Computer Simulation of Ion Beam Mixing

Seunghee Han

December 1988

UWFDM-789

Ph.D. thesis.

FUSION TECHNOLOGY INSTITUTE

UNIVERSITY OF WISCONSIN

MADISON WISCONSIN

Computer Simulation of Ion Beam Mixing

Seunghee Han

Fusion Technology Institute
University of Wisconsin
1500 Engineering Drive
Madison, WI 53706

http://fti.neep.wisc.edu

December 1988

UWFDM-789

Ph.D. thesis.

COMPUTER SIMULATION OF ION BEAM MIXING

by

Seunghee Han

A thesis submitted in partial fulfillment of the

requirements for the degree of

Doctor of Philosophy

(Nuclear Engineering and Engineering Physics)

at the

University of Wisconsin - Madison

1988

COMPUTER SIMULATION OF ION BEAM MIXING

Seunghee Han

Under the supervision of Professor Gerald L. Kulcinski

A highly optimized dynamic Monte Carlo program TAMIX has been developed on Cray to simulate the complicated nature of the ion beam mixing process. In addition to the collisional features, some of the diffusional processes (radiation-enhanced diffusion and radiation-induced segregation) are taken into account in TAMIX for high-temperature irradiation applications.

TAMIX can be run in three modes, i.e. static, collisional-dynamic, and collisional-diffusional-dynamic modes. One of the three run modes can be used to effectively simulate a specific situation. With static mode, where the target composition is assumed to remain unchanged, low-fluence ion and damage distributions can be calculated. Also, the static sputtering properties of the target can be studied with this mode. For a high ion fluence and low target temperature, the collisional-dynamic mode can be invoked to investigate the dynamic response of the target due to the collisional processes, suppressing the diffusional processes. The preferential sputtering along with the altered layer formation can be studied with this mode. If the target temperature is high, the diffusional processes are activated in addition to the collisional process, which can be simulated with the third mode, i.e. collisional-diffusional-dynamic mode. The combined effect of the collisional and diffusional processes can be investigated with this mode.

TAMIX has been applied extensively to a wide range of situations and

the calculated results were compared to available experimental data, which showed good agreement. Even the very complicated situation of co-deposition during ion implantation can be effectively simulated with TAMIX.

TAMIX is a highly optimized program in which a variance reduction scheme is adopted to reduce the computation time. Also, TAMIX is a vectorized Monte Carlo program, which uses a completely different algorithm from conventional 'history-based' Monte Carlo codes. For a sputtering calculation, a speed advantage of as much as a factor of 20 has been achieved with TAMIX compared to a similar Monte Carlo code for sputtering calculation TRIM.SP. In addition, various kinds of sophisticated models are used in TAMIX to obtain both speed and accuracy. Examples include tabulation of the scattering angles, energy-dependent mean free path for nuclear collisions, a 'random surface model' for sputtering, and concentration-dependent surface binding energies.

Approved:

12/23/88

Date

Professor Gerald L. Kulcinski

Department of Nuclear Engineering and Engineering Physics

Acknowledgement

It is absolutely impossible to express my full thanks to those who contributed to the completion of my thesis within these few words of acknowledgement. But, I wish to show my deep gratitude to them by naming some of the people who helped me complete this thesis.

The first and sincere thanks should be given to my thesis advisor Professor Gerald L. Kulcinski for his motivation, guidance, continual support and encouragement.

Also, I should say my special thanks to Professor John R. Conrad for his invitation to the PSII field and the permission to use some of his experimental data.

Sincere thanks should also be given to the other professors in my committee, Professor Dodd R. Arthur, Professor Gregory A. Moses, and Professor John H. Perepezko.

I am very much indebted to the members of Radiation Damage group for their academic stimulation, interest to my talk, and above all their indisputable help, R. D. Griffin, M. H. Hassan, D. J. Pertzborn, and D. H. Plantz. My special thanks go to J. Liang, L. Wang, and L. E. Seitzman for frequent helpful discussions in various fields.

I am also grateful to Dr. Y. Yamauchi from Tsukuba Laboratories in Japan for valuable discussions and Dr. N. Q. Lam in Argonne National Laboratory for advice on diffusion models.

Without the NMFECC supercomputing center, this thesis would not be

existing. I have to give my thanks to the consultants in the center as well as to John F. Santarius and Dennis C. Bruggink of the Fusion Technology Institute at the University of Wisconsin.

I can not repeat all of the names of my Korean friends, either here or in Korea, who helped make living in a foreign country much easier, but my sincerest thanks are given to all of them.

Finally, my greatest thanks should be given to my wife and daughter, who endured the past five years of loneliness and my negligence to them. Also, I dedicate this thesis to my parents in Korea who could not sleep even one good night with their son and daughter abroad.

This work was supported by the United States Department of Energy.

Contents

Abstract ii

Acknowledgement iv

1 Introduction 1

1.1 Definition 1

1.2 Mechanisms 3

1.3 Scope of this thesis 4

2 Stopping of ions in solid 9

2.1 Nuclear Stopping 10

2.1.1 Collision Kinematics 10

2.1.2 Interatomic potential 12

2.1.3 Nuclear stopping cross section 18

2.1.4 Validity of using the classical mechanics 24

2.1.5 Validity of binary collision model 28

2.2 Electronic stopping 28

2.2.1 Electronic stopping cross section 28

2.2.2 Bragg's rule 33

3 Range and Damage Distribution 39

3.1 Introduction 39

3.2 Range and damage distribution 41

3.3 Displacement production 51

4 Ion-Solid Interaction **58**

4.1 Sputtering 58

4.1.1 Sputtering of elemental target 61

4.1.2 Sputtering of multicomponent target 64

4.2 Collisional mixing 67

4.3 Diffusional processes 72

4.3.1 Radiation enhanced diffusion 72

4.3.2 Radiation induced segregation 74

4.3.3 Surface(Gibbisian) segregation 78

5 Computer simulation of ion beam mixing **85**

5.1 Computer simulation methods 85

5.1.1 Molecular dynamics simulation 85

5.1.2 Monte Carlo method 86

5.2 A dynamic Monte Carlo program TAMIX 92

5.2.1 Transport procedure 92

5.2.2 Displacement model 106

5.2.3 Sputtering process 108

5.2.4 Optimization 114

5.2.5 Dynamic simulation 117

5.2.6 Diffusion incorporation 120

5.2.7 Structure of TAMIX 124

6 Results and discussion **128**

6.1 Static mode 129

6.1.1 Range and damage distribution 129
6.1.2 Sputtering 135
6.2 Collisional dynamic mode 150
6.2.1 Preferential sputtering and altered layer formation . . . 150
6.2.2 Collisional mixing 156
6.2.3 High dose ion implantation 163
6.3 Collisional and diffusional dynamic mode 163

7 Summary and conclusion **181**

List of Figures

1.1 Schematic representation of ion beam mixing process 2

2.1 Nuclear and electronic stopping power of N in Ti 10

2.2 Elastic scattering between two particles 11

2.3 Regions of applicability of various interatomic potential 15

2.4 Various screening functions 18

2.5 Elastic scattering in the repulsive central force field 19

2.6 Differential scattering cross section 23

2.7 s_n and w_n for various potentials 25

2.8 Illustration of the validity of using classical mechanics in scattering problem 27

2.9 Electronic stopping cross section 34

3.1 Schematic picture of the ion trajectories and various ranges . . 40

3.2 Kinchin-Pease displacement model 53

4.1 Three regimes of knock-on sputtering 60

4.2 Experimental and theoretical values of the function $\alpha(M_2/M_1)$ 63

4.3 Calculated broadening and shift of a thin Pt marker in Si . . . 71

4.4 Temperature dependence of radiation enhanced diffusion . . . 74

5.1 Illustration of $P(x)$ and $C(x)$ 88

5.2 Equivalent target atomic cell 94

5.3 Various p_{max}'s for Be into Ni 95

5.4 Illustration of step length selection 99

5.5 Illustration of impact parameter selection 100
5.6 Scattering angle for the Universal potential 102
5.7 Directions before and after a collision 104
5.8 Displacement model used in TAMIX 106
5.9 Illustration of the random surface model 109
5.10 Refraction of the sputtered atom by a planar surface barrier . 111
5.11 Component surface binding energy for an ideal binary solution 114
5.12 CPU comparison with TRIM.SP and TAMIX for a sputtering calculation, D on Au 116
5.13 Grouping of recoils 118
5.14 Structure of TAMIX 125

6.1 Ion and damage distribution for 14 MeV Cu in Ni 130
6.2 Projected range and range straggling of Bi in Si 131
6.3 Projected range and range straggling of heavy ions in Si . . . 132
6.4 Projected range of N^{14} in Ni 133
6.5 PSII-N distribution in a bilayer target 134
6.6 Light ion back-scattering coefficients, D on Fe and He on Ag . 136
6.7 Sputtering yield of Kr and He on Be 138
6.8 Sputtering yield of Xe and He on Ni 140
6.9 Sputtering yield of Ar and D on Mo 141
6.10 Sputtering yield of Xe and H on Au 142
6.11 Sputtering yield of D on stainless steel 143

6.12 Incidence angle dependence of sputtering yield, Xe on Ni and He on Ni 144
6.13 Angular distribution of sputtered atoms for normal ion incidence, Xe on Ni and He on Ni 145
6.14 Angular distribution of sputtered atoms for glancing incidence, Xe on Ni 146
6.15 Energy distribution of sputtered atoms, Xe on Ni 147
6.16 Double differential distribution of sputtered atoms, Xe on Ni . 149
6.17 Group distribution of sputtered atoms, He on Ni and Xe on Ni 150
6.18 Origin depth distribution of sputtered atoms, Xe on Ni 151
6.19 Dynamic composition change and instantaneous partial sputtering yield of Lu-Fe by 1 keV Ar irradiation 153
6.20 Dynamic composition change and instantaneous partial sputtering yield of Lu-Fe by 5 keV Ar irradiation 154
6.21 Dynamic composition change and instantaneous partial sputtering yield of Lu-Fe by 10 keV Ar irradiation 155
6.22 Dynamic composition change and instantaneous partial sputtering yield of Pt-Au by 5 keV Ar irradiation 157
6.23 Broadening of Pt marker in Si by 300 keV Xe irradiation . . . 158
6.24 Collisional mixing of Cu + Ni by 50 keV Ar irradiation 159
6.25 TAMIX simulation of scanning AES 161
6.26 SIMS profile for PSII-CH_4 on Si 162
6.27 TAMIX simulation of PSII-CH_4 on Si 162
6.28 TAMIX simulation of PSII-CH_4 on Si 164

6.29 TAMIX simulation of PSII-CH_4 on Si 165

6.30 Areal density of retained N for PSII-N on Ti-6Al-4V 165

6.31 Profile evolution for a uniform irradiation on a foil, T= 200 °C 168

6.32 Profile evolution for a uniform irradiation on a foil, T= 500 °C 169

6.33 Profile evolution for a uniform irradiation on a foil, T= 800 °C 170

6.34 Temperature dependence of radiation induced segregation . . . 172

6.35 Profile evolution for a uniform irradiation with $\rho_d = 10^{10}$ /cm^2, at 200 °C 173

6.36 Profile evolution for a uniform irradiation with $E^m_{v,Cu} = 1.05$ eV, at 200 °C 174

6.37 Ion distribution for 14 MeV Cu in Ni with diffusion 175

6.38 Ion beam mixing of Cu + Ni by 50 keV Ar irradiation with diffusion 176

List of Tables

1.1 Summary of mechanisms for ion beam mixing 5

2.1 Analytical approximations for T-F equation 16

Chapter 1.

Introduction

1.1 Definition – What is ion beam mixing ?

In recent years, the use of ion beams for processing materials has received new emphasis. One aspect of this interest has been the application of energetic heavy ion bombardment to induce materials interactions in thin-film composite samples or previously ion-implanted solids. This processing technique which has come to be called **ion beam mixing**, has led to a variety of materials alterations that cannot be achieved with normal equilibrium processing techniques [1,2,3,4,5,6,7].

The ion beam mixing concept is illustrated in Fig. 1.1. If a thin film of element A is deposited on a solid B and bombarded with an energetic ion beam, a variety of complex interacting effects are initiated. Each ion slows down through a series of collisions with the target atoms along its path. Some of the ion energy is deposited in inelastic ionizing collisions and the rest in elastic displacement collisions. In most of ion beam mixing experiments, the ion beam parameters are chosen so that the energy deposited in displacement damage has its maximum at the interface as illustrated in the figure. The collision cascades initiated along the ion trajectory result in the displacement of many atoms of both A and B and the creation of many mobile defects. The various interactions mix the atoms and induce a materials interaction

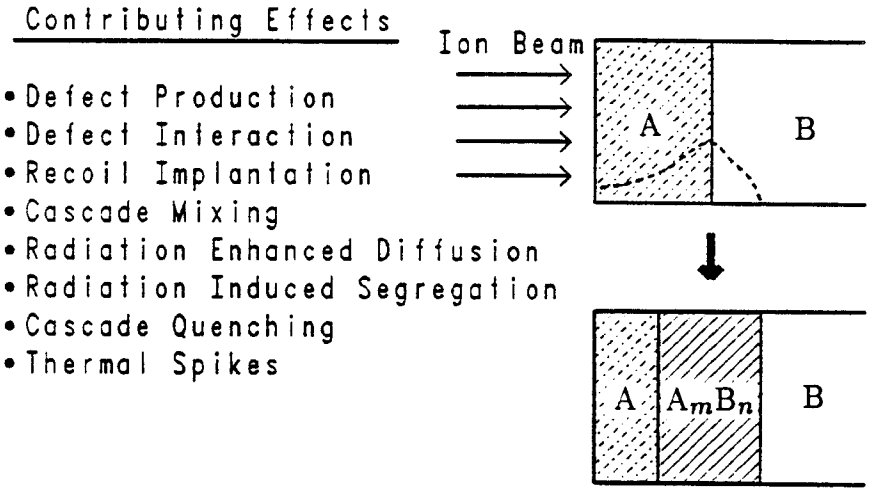

Figure 1.1: Schematic representation of ion beam mixing process

to result in a modified layer A_mB_n as denoted in Fig. 1.1. The degree of mixing, the final material formed, etc., depend on the relative importance of the contributing mechanisms.

The ion beam mixing is an alternative method to replace a high dose implantation for the modification of solids. For the case of metals, it is necessary to implant with a high dose (typically $> 10^{17}/\text{cm}^2$) in order to reach a concentration of foreign atoms sufficient to change the metallurgical properties of solids($\sim$ 10 atomic %). However, due to self-sputtering there is a limit of concentration achievable by ion implantation [13]. Ion beam mixing offers the possibility of overcoming this concentration limit and consequently it may have more potential for application to the modification of materials. Furthermore, it has been known that the atomic mixing accompanying sput-

tering events causes ultimate limits to the depth resolution attainable in sputter profiling of composite targets [8,14]. The perturbations due to ion beam mixing may also change the composition and distribution of species profiled. Hence, it is necessary to take the mixing effects into account when sputtering is used in profiling the multicomponent targets. Other applications of this technique have revealed greatly enhanced adhesion between coating and substrate materials even in non-reacting, immiscible system [15,16,17,18,19,20], and increased corrosion resistance by producing amorphous passive films on metal surface [21].

1.2 Mechanisms

Ion beam mixing is an all inclusive term which embraces some of the most complex phenomena in ion-solid interactions and, thus it can be anticipated that materials alterations induced by ions will be very difficult to attribute to a single mechanism. However, we can identify some of the fundamental mechanisms involved. First, collisional mixing (ballistic mixing) may be induced by recoil implantation and cascade mixing, as well as displacement spikes [8,9]. In the collisional mixing process, kinetic energy of the incident ions is transferred to target atoms via atomic collisions, which depends on the mass numbers of the systems involved. In principle, collisional mixing does not depend on the temperature of the substrate during ion irradiation. Second, diffusional mixing involves radiation-enhanced diffusion and radiation-induced segregation, which would be caused by mobile defects such as vacancies and interstitials generated by the irradiation [10,11]. The diffusional mixing is a

thermally activated process and depends on the temperature of the substrate. These mechanisms are summarized in Table 1.1.

Until now, most of the theoretical work has been concentrated on the collisional mixing mechanisms, which is in turn divided into two areas; one is an analytical approach using various kinds of approximations to solve the governing equations [22,9,23,24], and the other is a development of Monte Carlo computer code which adopts a binary collision approximation to simulate the collisional processes [25,26]. This thesis work basically belongs to the latter group, however in which the diffusional processes were also considered.

1.3 Scope of this thesis

The purpose of this thesis is to develop a comprehensive Monte Carlo computer program which can effectively simulate the ion beam mixing processes induced by energetic ion bombardment on the composite multicomponent target. The collisional mixing and some of the diffusional processes have been modeled into a large scale Monte Carlo code-TAMIX(Transport And MIXing from ion irradiation) through various kinds of sophistication. In the TAMIX code, phase transformations in the target have not been taken into account. This means that the complete solid solution between different elemental species was assumed, which is often observed because of the increased solid solubility under ion irradiation.

In chapter 2, the elemental stopping processes of energetic ions in solids will be reviewed, which includes the recent models of interatomic potential and electronic stopping formula. In chapter 3, the analytic treatment of the ion

Process	Features	Time scale
Collisional mixing (*ballistic mixing*)	prompt processes non thermally activated, high energies	
1. Primary recoil mixing (recoil implantation)	collision between moving and stationary particle low density, isolated displacements one of the first collisions in a sequence	10^{-13} sec
2. Cascade mixing	collision between moving and stationary particle isolated displacements later in the collision sequence linear phenomena deposited energy α number of displacement isotropic and anisotropic mixing	10^{-12} sec
3. Displacement spikes	collision between moving particles overlapping displacements non-linear phenomena all atoms in spike volume have energy heat of fusion	10^{-11} sec
Diffusional processes	delayed processes, low energies thermally activated, thermodynamic driving forces	
1. RED	transport by enhanced diffusion	1 hour
2. RIS	transport by defect fluxes	
Radiation-modified diffusion	persistent effects, thermally activated	> 1 hour

Table 1.1: Summary of mechanisms for ion beam mixing [12]

range and damage distribution will be summarized along with the displacement model. The various ion-solid interactions will be discussed in chapter 4, in which the sputtering, collisional mixing and rearrangement, and diffusional processes are summarized. After a brief introduction of the Monte Carlo method, the various kinds of models along with the calculation procedures adopted in TAMIX will be presented in chapter 5. In chapter 6, the simulation results will be shown and compared extensively with other available data and also, the practical applications of TAMIX in some complicated situations will be presented. Finally, in chapter 7 the summary and conclusion will be drawn with a brief mention to the future direction of research.

References

[1] J. W. Mayer et al., "Ion Implantation Metallurgy"(C. M. Preecy and J. K. Hirvonen, eds.), p. 37, The Metallurgical Society of AIME (1980).

[2] J. W. Mayer, B. Y. Tsaur, S. S. Lau, and L. S. Hung, Nucl. Instr. and Meth. **182/183**, 1 (1981).

[3] B. Y. Tsaur and J. W. Mayer, Appl. Phys. Lett. **37**, 389 (1980).

[4] B. Y. Tsaur, S. S. Lau, and J. W. Mayer, Appl. Phys. Lett. **36**, 823 (1980).

[5] B. Y. Tsaur, J. W. Mayer, J. F. Graczyk, and K. N. Tu, J. Appl. Phys. **51**, 5334 (1980).

[6] B. Y. Tsaur, J. W. Mayer, and K. N. Tu, J. Appl. Phys. **51**, 5326 (1980).

[7] B. Y. Tsaur, S. S. Lau, L. S. Hung, and J. W. Mayer, Nucl. Instr. and Meth. **182/183**, 67 (1981).

[8] U. Littmark and W. O. Hofer, Nucl. Instr. and Meth. **168**, 329 (1980).

[9] P. Sigmund and Gras-Marti, Nucl. Instr. and Meth. **168**, 389 (1980).

[10] G. J. Dienes and A. C. Damask, J. Appl. Phys. **29**, 1713 (1958).

[11] J. C. Bourgoin and J. W. Corbett, Rad. Effect **36**, 157 (1978).

[12] Z. L. Wang, Nucl. Instr. and Meth. **B2**, 784 (1984).

[13] Z. L. Liau and J. W. Mayer, J. Vac. Sci. Technol. **15**, 1629 (1978).

[14] H. H. Andersen, J. Appl. Phys. **18**, 131 (1979).

[15] J. E. Griffith, Y. Qiu, and T. A. Tombrello, Nucl. Instr. and Meth. **198**, 607 (1982).

[16] S. Jacobson, B. Jonsson, and B. Sundqvist, Thin Solid Films, **107**, 89 (1983).

[17] J. E. E. Baglin, G. J. Clark, and J. Bøttiger, in: Thin Films and Interfaces II, eds., J. E. E. Baglin, D. S. Campbell and W. K. Chu (Elsevier, New York, 1984), p. 179.

[18] T. A. Tombrello, ibid., p. 173.

[19] I. V. Mitchell et al., ibid., p. 189.

[20] J. E. E. Baglin, G. J. Clark, Nucl. Instr. and Meth. **B7/8**, 881 (1985).

[21] R. S. Bhattacharya, et al., Nucl. Instr. and Meth. **B7/8**, 694 (1985).

[22] P. K. Haff and Z. E. Switkowski, J. Appl. Phys. **48**, 3383 (1977).

[23] S. Matteson, B. M. Paine, and M. A. Nicolet, Nucl. Instr. and Meth. **182/183**, 53 (1981).

[24] P. Sigmund and A. Gras-Marti, Nucl. Instr. and Meth. **182/183**, 25 (1981).

[25] M. L. Roush et al. Nucl. Instr. and Meth. **194**, 611 (1982).

[26] W. Möller and W. Eckstein, Nucl. Instr. and Meth. **B7/8**, 645 (1985).

Chapter 2.

Stopping of ions in solid

The slowing down of ions in solid is a many-body problem, which involves nuclei and electrons of interacting ion and target atoms. Here we are concerned about the ion-solid interaction, where maximum incident ion energy can be a few tens of MeV. In this energy range, as Bohr [1,2] suggested, **nuclear stopping** and **electronic stopping** are the two major stopping processes. Furthermore, he concluded that these two stopping processes could be separated because of the large mass difference between nuclei and electrons.

Nuclear stopping is defined as the energy and momentum transfer of an ion to the target atom due to the elastic collision under the influence of a Coulomb field that is partially screened by consisting electrons. Therefore, nuclear stopping gives a discrete energy loss and an abrupt change of direction of the moving ion. On the other hand, electronic stopping is defined as the energy loss of the moving ion from its interaction with target electron clouds, i.e. excitation and ionization. The ion loses its energy continuously, but doesn't suffer any change of direction of motion by this process. Fig. 2.1 shows the typical dependence of each stopping process on the ion energy. As seen in the figure, nuclear stopping dominates in the low energy region and electronic stopping in the high energy region.

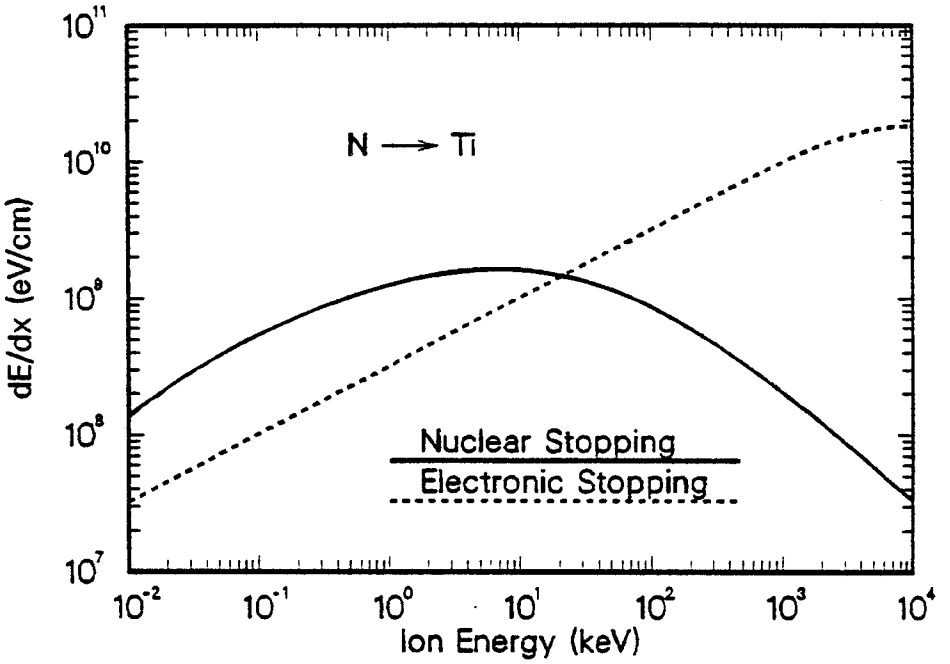

Figure 2.1: Nuclear and electronic stopping power of N in Ti

2.1 Nuclear Stopping

2.1.1 Collision Kinematics

Fig. 2.2(a) shows the schematic diagram of a nonrelativistic elastic collision between two particles in the laboratory frame. Suppose that particle 1 (the projectile) with mass M_1 and velocity v_{10} makes a collision with a stationary particle 2 (the target) with mass M_2. In the figure, v_{1f} and v_{2f} represent the velocities of the projectile and target atom after collision, respectively. Transforming the coordinate system to center of mass system, the analysis can be simplified. The velocity of center of mass is given by

$$v_{cm} = \left(\frac{M_1}{M_1 + M_2}\right) v_{10} \tag{2.1}$$

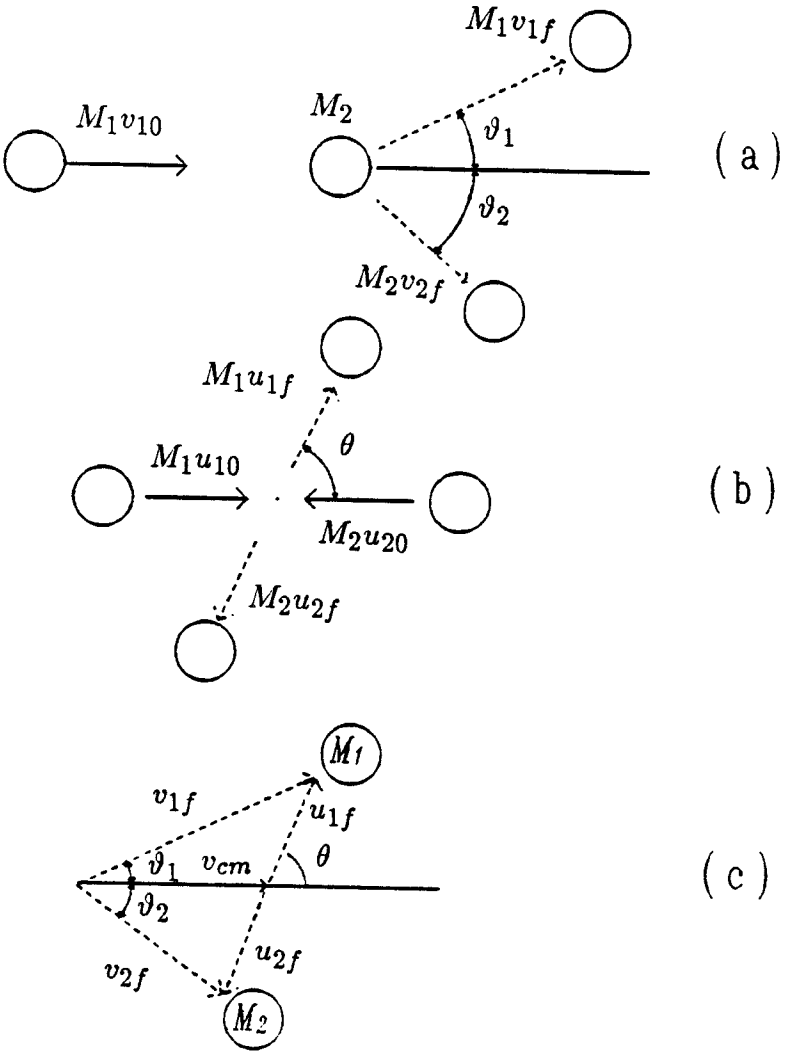

Figure 2.2: Elastic scattering between two particles; (a) viewed in laboratory frame (b) view in the center of mass frame (c) vector diagram relating the velocities in two reference frames

The collision viewed in center of mass system is shown in Fig. 2.2(b). In the figure, u's and θ are the velocities and scattering angle in the center of mass frame respectively. Applying the energy and momentum conservation law, one can easily get the energy transfer to the target atom, T as

$$T = \frac{\Lambda E}{2}(1 - \cos\theta) = \Lambda E \sin^2\frac{\theta}{2} \tag{2.2}$$

, where E is the initial energy of the projectile before collision and Λ is the energy transfer factor given by

$$\Lambda = \frac{4M_1M_2}{(M_1 + M_2)^2} \tag{2.3}$$

The maximum energy transfer from the projectile to the target atom occurs in a head-on collision, for which $\theta = \pi$ and

$$T_{max} = \Lambda E \tag{2.4}$$

Fig. 2.2(c) shows the vector diagram between the velocities in the laboratory frame and center of mass frame. Using this diagram, the relations between scattering angles are given by

$$\begin{aligned} \tan\vartheta_1 &= \frac{M_2 \sin\theta}{M_1 + M_2\cos\theta} \\ \vartheta_2 &= \frac{\pi - \theta}{2} \end{aligned} \tag{2.5}$$

, where ϑ_1 and ϑ_2 are the scattering angles of the projectile and target atom in the laboratory frame, respectively.

2.1.2 Interatomic potential

To accurately assess the atomic scattering process, we have to know the force between interacting particles, in other words, interatomic potential.

There are two major contributions to the repulsive potential between two atoms; (1) the electrostatic repulsion between positively charged nuclei and (2) the increase in energy required to maintain the electrons of nearby atoms in the same region of space without violating the Pauli exclusion principle.

For low energy collisions the interatomic distance of approach is of the order of equilibrium spacing of the atoms in the crystal lattice. In this case the nuclear repulsion is small because the positive nuclear charges are nearly completely shielded by the electrons. In this region the potential energy of interaction is adequately represented by the Born-Mayer [3] potential:

$$V(r) = A \exp\left(-\frac{r}{\rho}\right) \tag{2.6}$$

, where A and ρ are determined from experiments.

At the other extreme of a high energy collision, the repulsive force between the two bare nuclei dominates the effect of overlapping electrons and this force increases as distance between the particles decreases. In this limit, the interaction is satisfactorily described by the Coulomb potential:

$$V(r) = \frac{Z_1 Z_2 e^2}{r} \tag{2.7}$$

, where Z_1 and Z_2 are the atomic numbers of the two atoms or ions and e is the electronic charge.

The intermediate region where both Coulombic repulsion and closest shell repulsion are of comparable magnitudes is the most difficult to describe accurately. Unfortunately, this energy region is the region of most concern on ion implantation. Often, this region is represented by the screened Coulomb potential in the form of

$$V(r) = \frac{Z_1 Z_2 e^2}{r} \Phi\left(\frac{r}{a}\right) \tag{2.8}$$

, where a is the characteristic screening radius. These three cases are shown schematically in Fig. 2.3. In the figure, the solid region denotes the nuclear charge and the shaded region represents the electron clouds.

There have been a number of theoretical investigations to develop the expressions for the screening function Φ. Based on the statistical atomic model Thomas [4] and Fermi [5] derived an equation called Thomas-Fermi equation:

$$\Phi'' = \frac{\Phi^{\frac{3}{2}}}{x^{\frac{1}{2}}} \tag{2.9}$$

with the boundary conditions of

$$\Phi(x \longrightarrow 0) = 1 \qquad , \qquad \Phi(x \longrightarrow \infty) = 0 \tag{2.10}$$

This equation cannot be solved analytically and numerical solutions are required. For practical purposes, it is convenient to represent the result of numerical calculations of $\Phi(x)$ by analytic expressions. Thus, many approximations to the T-F function $\Phi(x)$ have been obtained. Some of these approximations are given in Table 2.1 [6].

Bohr [7] suggested a screening function:

$$\Phi(x) = \exp(-x) \tag{2.11}$$

The screening function for a Lenz-Jensen atom [8,9] is:

$$\Phi(x) = \exp(-t)(1 + t + 0.3344t^2 + 0.0485t^3 + 2.647 \times 10^{-3}t^4) \tag{2.12}$$

, where

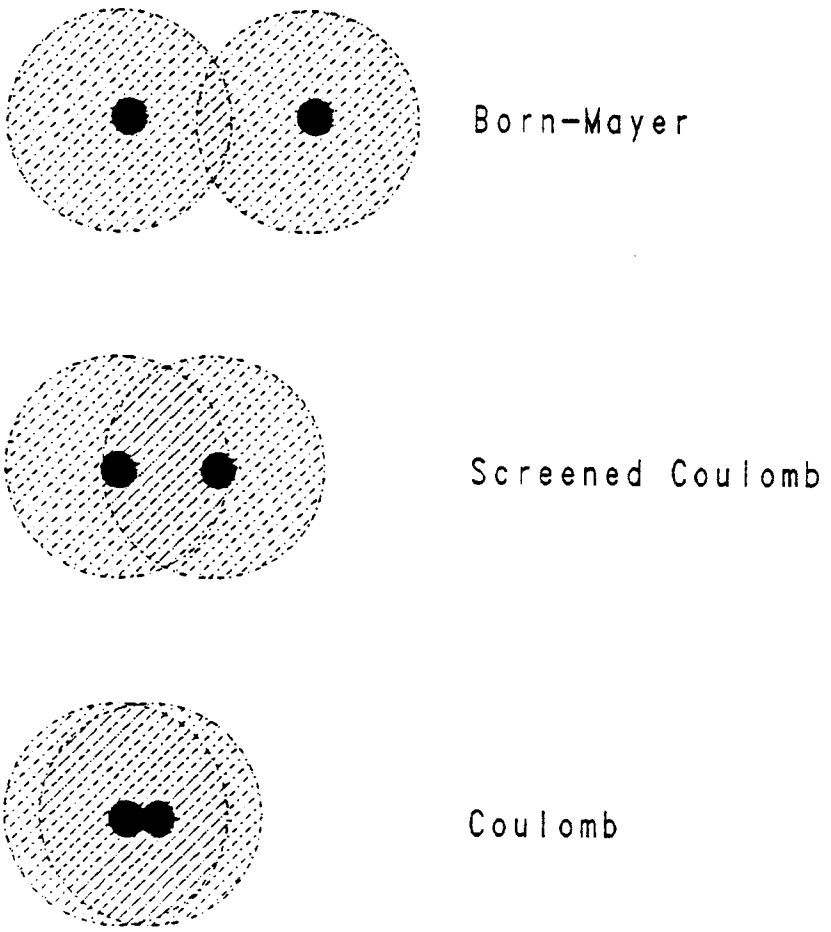

Figure 2.3: Regions of applicability of various interatomic potential

Author	Analytical expression for (x)
1. Sommerfeld [20]	$\left[1+\left(\frac{x}{12^{2/3}}\right)^{\lambda}\right]^{-3/\lambda}$ $\lambda = 0.772$ (Sommerfeld [20]) $\lambda = 0.8034$ (March [21]) $\lambda = 0.8371$ (Umeda [22])
2. Kerner [24]	$(1+Bx)^{-1}$ $B = 1.3501$ (Kerner [24]) $B = 1.3679$ (Umeda [22])
3. Brinkman [25]	$Cx^{1/2}K_1(2Ax^{1/2})$
4. Tietz [26]	$(1+(B/6^{1/2})\cdot x)^{-2}$
5. Rozental [28]	$0.7345e^{-0.562x}+0.2655e^{-3.392x}$
6. Rozental [28]	$0.255e^{-.0246x}+0.581e^{-0.947x}+0.164e^{-4.356x}$
7. Molière [29]	$0.35e^{-0.3x}+0.55e^{-1.2x}+0.10e^{-6.0x}$
8. Csavinsky [30]	$(0.7111e^{-0.175x}+0.2889e^{-1.6625x})^2$
9. Roberts [31, 32]	$(1+1.7822x^{1/2})\exp[-1.7822x^{1/2}]$
10. Wedepohl [33]	$317x\exp[-6.62x^{1/4}]$
11. Lindhard [23]	$1-x/(3+x^2)^{1/2}$
12. Lindhard [23]	$1-1/2x$

Table 2.1: Analytical approximations for T-F equation [6]

$$t = 3.11126x^{\frac{1}{2}} \tag{2.13}$$

Wilson et al. [10] suggested a more refined screening function from theoretical and experimental studies called Kr-C potential:

$$\Phi(x) = 0.1909e^{-0.2785x} + 0.4737e^{-0.6372x} + 0.3354e^{-1.9192x} \tag{2.14}$$

The solutions thus far considered are screening functions for a single atom. To create an interatomic screening function, previous workers used above single atom potentials and adjusted the screening length to account for the two-atom potential.

Bohr [11,12] suggested a form:

$$a = \frac{a_0}{\left(Z_1^{2/3}+Z_2^{2/3}\right)^{1/2}} \tag{2.15}$$

, where a_0 is the Bohr radius (0.529 Å).

Firsov [13,14,15,16] made computer calculations based upon merging two Thomas-Fermi atoms and suggested that interatomic potential would be best described by the neutral atomic T-F screening function, but with a reduced screening radius being defined as

$$a = \frac{0.8853 a_0}{\left(Z_1^{1/2} + Z_2^{1/2}\right)^{2/3}} \tag{2.16}$$

Lindhard [17] suggested also using the T-F screening function but with

$$a = \frac{0.8853 a_0}{\left(Z_1^{2/3} + Z_2^{2/3}\right)^{1/2}} \tag{2.17}$$

Recently, Biersack and Ziegler [18] made an extensive calculation for the interatomic potential, and developed a semi-empirical screening function called **universal potential:**

$$\begin{aligned} \Phi_u(x) = 0.1818 e^{-3.2x} &+ 0.5099 e^{-0.9423x} \\ &+ 0.2802 e^{-0.4028x} + 0.02817 e^{-0.2016x} \end{aligned} \tag{2.18}$$

with a **universal screening length** :

$$a_u = \frac{0.8854 a_0}{Z_1^{0.23} + Z_2^{0.23}} \tag{2.19}$$

Fig. 2.4 shows those frequently used screening functions, i.e.

- Sommerfeld approximation of T-F potential
- Moliere approximation of T-F potential
- Bohr potential

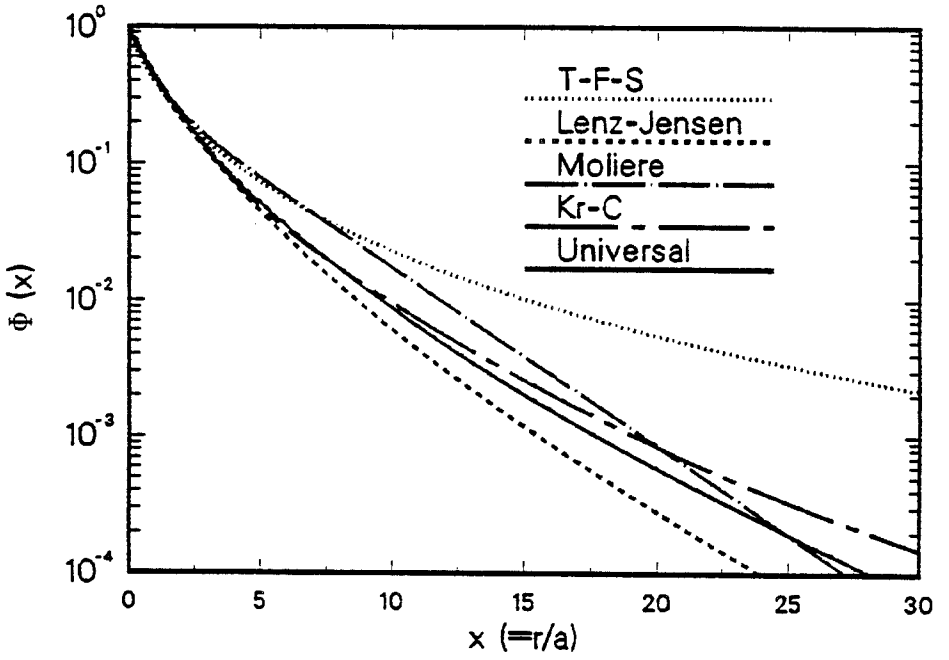

Figure 2.4: Various screening functions

- Lenz-Jensen potential
- Kr-C potential
- Universal potential

2.1.3 Nuclear stopping cross section

To calculate the cross section for the energy transfer we have to know the probability for each final scattering angle, and this is obtained only after evaluating the details of the scattering trajectory and hence the probability of scattering into each angle.

Fig. 2.5 shows the schematic picture of an elastic binary collision in the center of mass frame under the influence of the interatomic potential which is a function of their separation distance only. Using this coordinate system, we

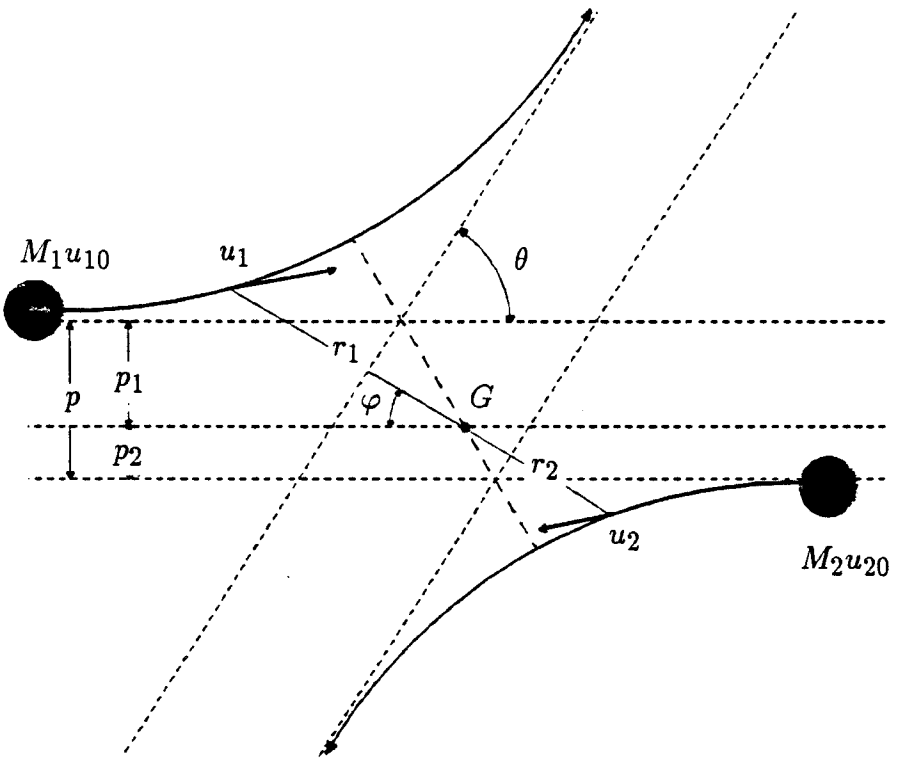

Figure 2.5: Elastic scattering in the repulsive central force field as viewed in the center of mass frame

can reduce the two-body problem to a one-body problem.

The energy conservation of the system requires that

$$E_{c0} = \frac{1}{2}M_1 u_1^2 + \frac{1}{2}M_2 u_2^2 + V(r) \tag{2.20}$$

, where E_{c0} is the initial kinetic energy of the system in the center of mass frame, i.e.

$$\begin{aligned} E_{c0} &= \frac{1}{2}M_1 u_{10}^2 + \frac{1}{2}M_2 u_{20}^2 \\ &= \frac{1}{2}\frac{M_1 M_2}{M_1 + M_2} v_{10}^2 \\ &= \frac{M_2}{M_1 + M_2} E_{10} \end{aligned} \tag{2.21}$$

The RHS of eq.(2.20) can be changed into polar coordinates noting that

$$\begin{aligned} u_1^2 &= u_{1r}^2 + u_{1\varphi}^2 = \dot{r}_1^2 + r_1^2\dot{\varphi}^2 \\ u_2^2 &= u_{2r}^2 + u_{2\varphi}^2 = \dot{r}_2^2 + r_2^2\dot{\varphi}^2 \end{aligned} \tag{2.22}$$

and

$$\begin{aligned} r_1 &= \frac{M_2}{M_1 + M_2} r \\ r_2 &= \frac{M_1}{M_1 + M_2} r \end{aligned} \tag{2.23}$$

The resulting equation will be

$$E_{c0} = \frac{M_1 M_2}{2(M_1 + M_2)}(\dot{r}^2 + r^2\dot{\varphi}^2) + V(r) \tag{2.24}$$

Because the system is in the central force field, the angular momentum should be also conserved, which gives

$$M_1 u_{10} p_1 + M_2 u_{20} p_2 = M_1 u_{1\varphi} r_1 + M_2 u_{2\varphi} r_2 \tag{2.25}$$

Using eq.(2.21), eq.(2.22), and eq.(2.23) along with eq.(2.1) and noting that

$$\begin{aligned} p_1 &= \frac{M_2}{M_1+M_2}p \\ p_2 &= \frac{M_1}{M_1+M_2}p \end{aligned} \tag{2.26}$$

, we get

$$\dot{\varphi} = \frac{p}{r^2}\sqrt{\frac{M_1+M_2}{M_1M_2}}\sqrt{2E_{c0}} \tag{2.27}$$

Substituting this expression for $\dot{\varphi}$ in eq.(2.24) results in

$$\dot{r} = -\sqrt{\frac{2(M_1+M_2)}{M_1M_2}}\sqrt{\left(1-\frac{p^2}{r^2}\right)E_{c0} - V(r)} \tag{2.28}$$

For a closest approach distance of r_0, $\dot{r} = 0$. Hence, r_0 is obtained from the equation:

$$\left(1-\frac{p^2}{r_0^2}\right)E_{c0} - V(r_0) = 0 \tag{2.29}$$

If we note that

$$d\varphi = \frac{d\varphi}{dr}dr = \frac{\dot{\varphi}}{\dot{r}}dr \tag{2.30}$$

, we can get the expression for $d\varphi$ using eq.(2.27), and eq.(2.28)

$$d\varphi = -\frac{pdr}{r^2\sqrt{1-\frac{V(r)}{E_{c0}}-\frac{p^2}{r^2}}} \tag{2.31}$$

The final expression for the scattering angle θ in the center of mass system is given as

$$\begin{aligned} \theta &= \pi - 2\int_0^{\frac{\varphi max}{2}} d\varphi \\ &= \pi - 2p\int_\infty^{r_0} \frac{-dr}{r^2\sqrt{1-\frac{V(r)}{E_{c0}}-\frac{p^2}{r^2}}} \end{aligned} \tag{2.32}$$

For a screened Coulomb potential (that will be used in this study), $V(r)$ is expressed with a screening function $\Phi(\frac{r}{a})$ as

$$V(r) = \frac{Z_1 Z_2 e^2}{r} \Phi\left(\frac{r}{a}\right) \tag{2.33}$$

New units for energy and impact parameter can be defined, that is reduced energy ε, as

$$\varepsilon = \frac{a E_{c0}}{Z_1 Z_2 e^2} = \frac{a}{Z_1 Z_2 e^2} \frac{M_2}{M_1 + M_2} E_{10} \tag{2.34}$$

and reduced impact parameter b, as

$$b = \frac{p}{a} \tag{2.35}$$

, where both ε and b are dimensionless. With these and replacing $\frac{a}{r}$ with z, one obtains

$$\theta = \pi - 2b \int_0^{z_0} \frac{dz}{\sqrt{1 - \frac{z}{\varepsilon}\Phi\left(\frac{1}{z}\right) - b^2 z^2}} \tag{2.36}$$

, where z_0 is the root of the equation

$$1 - \frac{z_0}{\varepsilon}\Phi\left(\frac{1}{z_0}\right) - b^2 z_0^2 = 0 \tag{2.37}$$

Eq.(2.36) and eq.(2.37) allow the calculation of the final scattering angle with the new parameters ε and b, and the individual atomic variables Z_1, Z_2, M_1, and M_2 have been eliminated.

The differential scattering cross section is defined with

$$d\sigma = 2\pi p dp = \sigma(\theta) 2\pi \sin\theta d\theta \tag{2.38}$$

Fig. 2.6 shows the calculated differential scattering cross section for Moliere potential and Universal potential.

The nuclear stopping cross section, $S_n(E)$ is the average energy transferred

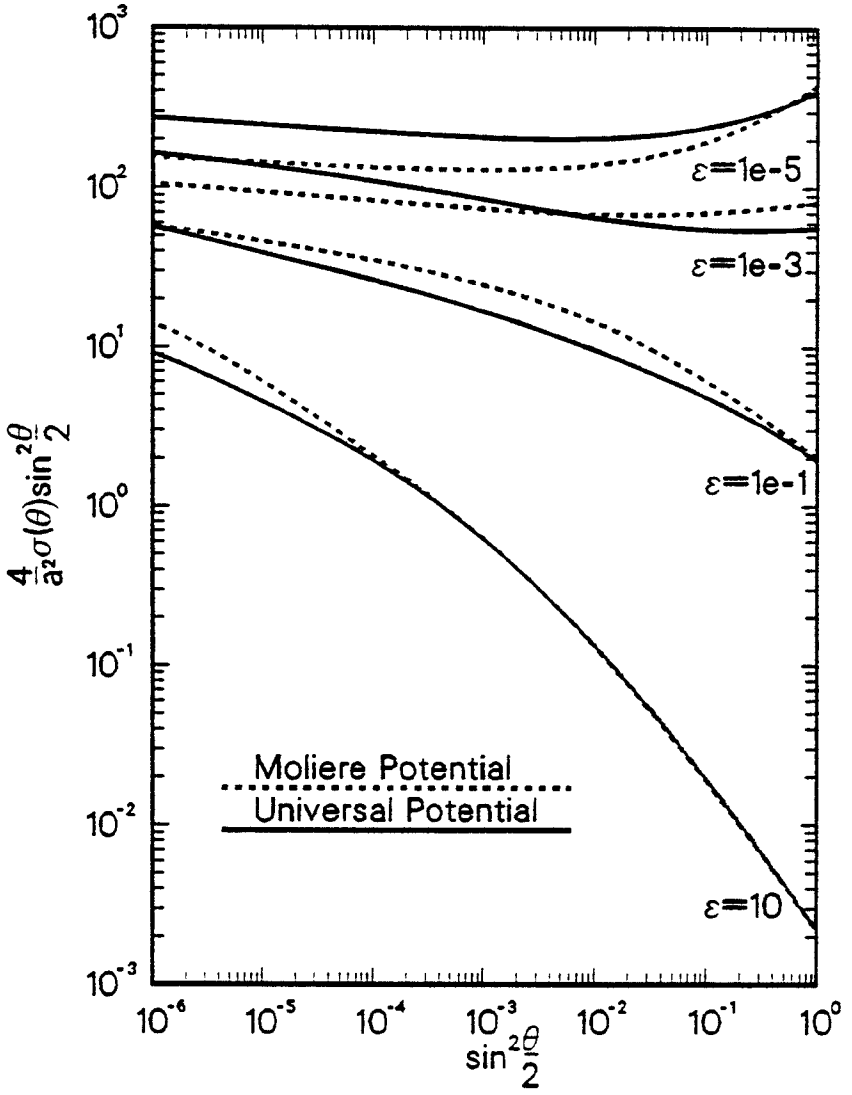

Figure 2.6: Differential scattering cross section for Moliere and Universal potential

in a collision, so from eq.(2.2), eq.(2.3), and eq.(2.38) we have

$$\begin{aligned} S_n(E) &= \int T d\sigma = \int_0^{pmax} T 2\pi p dp \\ &= \pi a^2 \Lambda E \int_0^{b^2_{max}} \sin^2 \frac{\theta}{2} d(b^2) \end{aligned} \tag{2.39}$$

If one defines reduced nuclear stopping cross section $s_n(\varepsilon)$ as

$$s_n(\varepsilon) = \frac{\varepsilon}{\pi a^2 \Lambda E} S_n(E) \tag{2.40}$$

, then

$$s_n(\varepsilon) = \varepsilon \int_0^{b^2_{max}} \sin^2 \frac{\theta}{2} d(b^2) \tag{2.41}$$

The straggling of nuclear energy loss, $\Omega_n(E)$ can be calculated similarly as

$$\Omega_n^2(E) = \int T^2 d\sigma = \pi a^2 \Lambda^2 E^2 \int_0^{b^2_{max}} \sin^4 \frac{\theta}{2} d(b^2) \tag{2.42}$$

Again, reduced nuclear straggling will be

$$w_n(\varepsilon) = \frac{\varepsilon^2}{\pi a^2 \Lambda^2 E^2} \Omega_n^2(E) = \varepsilon^2 \int_0^{b^2_{max}} \sin^4 \frac{\theta}{2} d(b^2) \tag{2.43}$$

Fig. 2.7 shows $s_n(\varepsilon)$ and $w_n(\varepsilon)$ for various potentials.

2.1.4 Validity of using the classical mechanics

The collision between atoms can also be properly expressed in terms of the superposition of the wave functions of moving ion and target atom and the scattering law can be determined by solutions of the wave equations. However, in some conditions classical mechanics can give satisfactory results with much simpler calculations. Bohr [7] discussed this validity criteria extensively.

If we want to apply the classical mechanics to the scattering problem, two conditions must be satisfied:

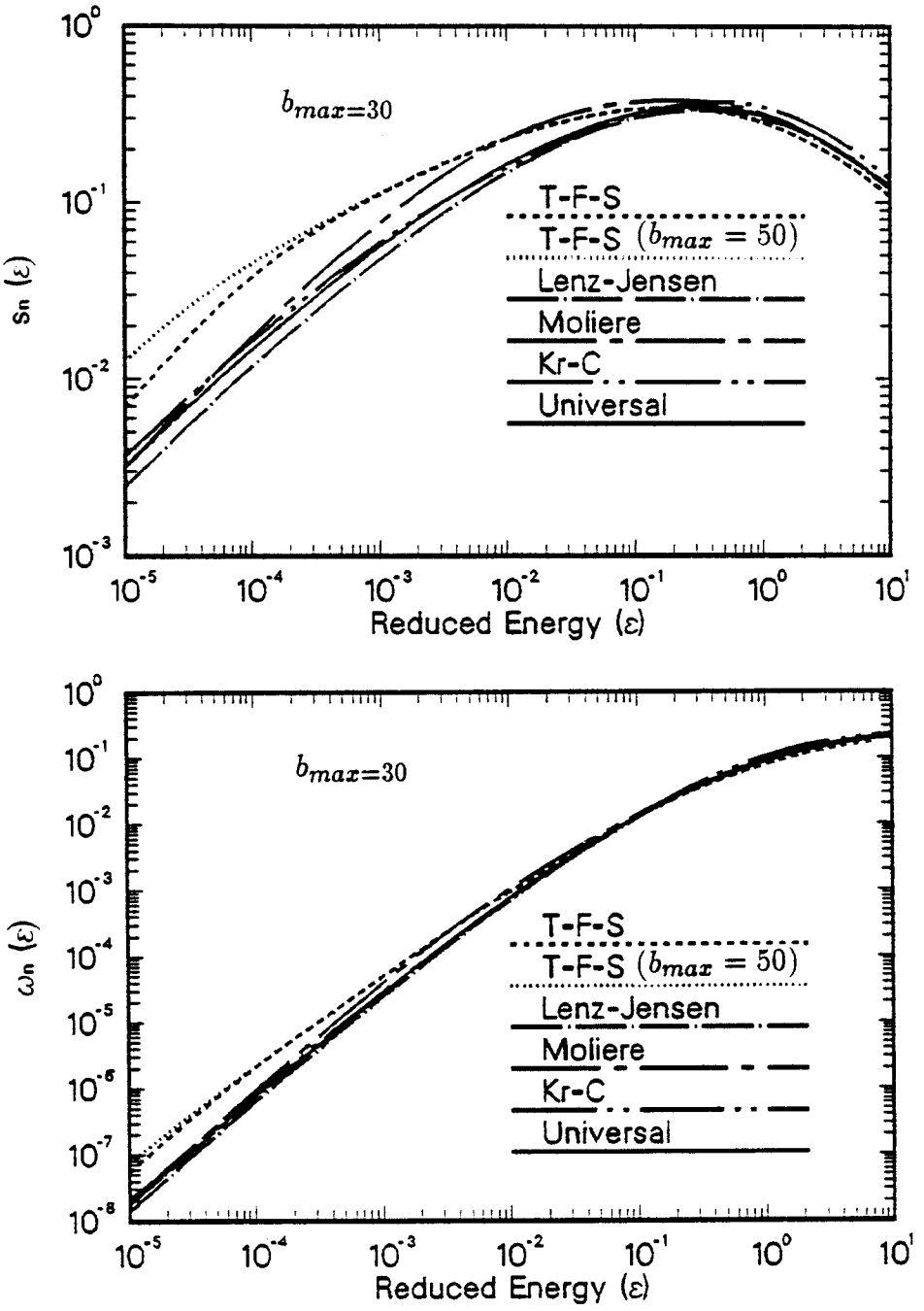

Figure 2.7: Reduced nuclear stopping cross section s_n and straggling w_n for various potentials

1. The particle trajectories must be well defined with respect to the smallest dimension of the system.

2. The deflection angle of the incident particle must be well defined.

Before discussing these criteria quantitatively, some variables need to be defined, i.e. a is the usual screening length and collision diameter b_c is defined as the closest approach distance in a head-on collision in Coulomb field:

$$b_c = \frac{Z_1 Z_2 e^2}{E_{c0}} \tag{2.44}$$

, where E_{c0} is the kinetic energy in the center of mass system. If we denote λ as the wave length associated with the incident particle, λ will be

$$\lambda = \frac{\hbar}{P} = \frac{\hbar}{M_1 v_{10}} \tag{2.45}$$

Furthermore, we define

$$\begin{aligned} \chi &= \frac{b_c}{\lambda} \\ \xi &= \frac{1}{\varepsilon} = \frac{b_c}{a} \end{aligned} \tag{2.46}$$

, where ε is the reduced energy.

To satisfy the condition 1, the minimum dimension of the system should be larger than the wave length λ. Hence,

$$\begin{aligned} b_c &> \lambda \quad \text{if} \quad a > b_c \\ a &> \lambda \quad \text{if} \quad a < b_c \end{aligned} \tag{2.47}$$

or

$$\begin{aligned} \chi &> 1 \quad \text{if} \quad \xi < 1 \\ \chi &> \xi \quad \text{if} \quad \xi > 1 \end{aligned} \tag{2.48}$$

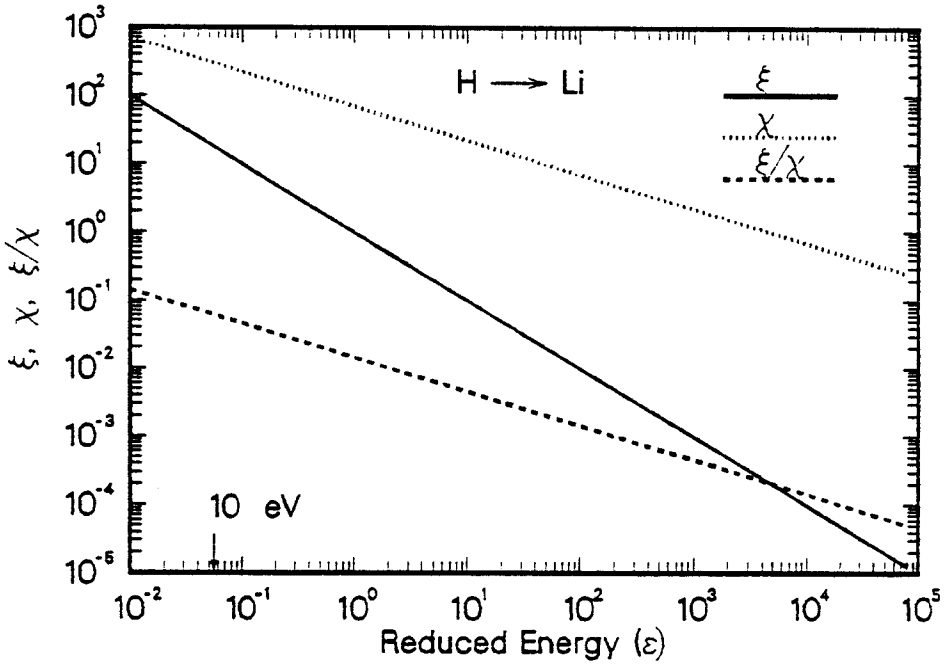

Figure 2.8: Illustration of the validity of using classical mechanics in scattering problem

The condition 2 can be understood with the help of uncertainty principle $\Delta P\ \Delta X \geq \hbar$, where ΔX is of the order of a(screening length). If one uses the impulse approximation for the evaluation of θ_{min}, it will be given by

$$\theta_{min} = \frac{\Delta P}{P} \sim \frac{\hbar}{aP} = \frac{\xi}{\chi} \tag{2.49}$$

Therefore, the second condition will be satisfied if the scattering angle is greater than θ_{min}. Fig. 2.8 shows the conservative case of proton on Li. One can see that both conditions are satisfied except at very high reduced energy(ε). However, in this region the electronic stopping dominates the stopping of the ion. Thus, it is concluded that for charged particles which have masses at least as great as that of proton, the classical collision approximation is valid in the energy range of interest for the present work.

2.1.5 Validity of binary collision model

The collision of the ion with target atoms is a many body interaction in nature. However, due to the fact that the interaction force decreases rapidly when the distance of approach is larger than the order of an atomic diameter, the binary collision approximation is probably reasonable. For very low energy interaction, the moving atom interacts with more than one target atom simultaneously. The energy limit below which the multiple scattering effects become important can be estimated by equating the velocity of the longitudinal sound wave in the solid to the ion velocity [19]. This energy limit is of the order of 10 eV, which is usually below the energy range of interest.

2.2 Electronic stopping

2.2.1 Electronic stopping cross section

The electronic stopping is defined as the energy loss of ions by the excitation and ionization of the electrons of the target medium. Bohr [11,12] suggested that the ion will be stripped of all its electrons if the ion velocity is greater than the electron velocity of the ion's K-shell ($v > Z_1 v_0$). In this high energy region, he derived the electronic energy loss considering the electrons in a target atom as harmonic oscillators, i.e.:

$$S_e = \frac{4\pi Z_1^2 Z_2 e^4}{mv^2} \ln L \tag{2.50}$$

, where

$$L = \frac{1.123 mv^3}{Z_1 e^2 \bar{w}} \tag{2.51}$$

, where $\bar{w}$ is the geometric mean frequency of the harmonic oscillators. Bethe [20] and Bloch [21] obtained similar expressions from a quantum mechanical approach but expressed L in terms of the average ionization energy I as

$$L = \frac{2mv^2}{I} \tag{2.52}$$

There have been many attempts [22,23,24,25,26,27] to make S_e more sophisticated. Different theories yield similar expressions excluding the logarithmic term, which varies slowly with the ion energy. Generally speaking, the theories for electronic stopping at high energies are well developed.

As the ion slows down, it begins to capture electrons and these bound electrons screen the nuclear charge of the ion. In this intermediate energy region, it is very difficult to describe the highly distorted electron configuration of the partially stripped ion, so no precise theoretical treatment exists. Bohr [11,12] mentioned that if the effective charge of the ion could be estimated, then the traditional stopping theory could be used. Later this effective charge concept became widely used for scaling of the proton stopping power to those of heavy ions, which has the form:

$$S_{HI}(v_1, Z_2) = S_p(v_1, Z_2) Z^{*2}_{HI}(v_1) \tag{2.53}$$

, where $S_{HI}(v_1, Z_2)$ is the electronic stopping cross section of a heavy ion with velocity v_1 at the target material Z_2, and $S_p(v_1, Z_2)$ is the proton stopping cross section at the same velocity in the same material, and $Z^*_{HI}(v_1)$ is the effective charge of the ion at this velocity. Northcliff [28] gave an empirical formula for the effective charge as

$$Z_1^* = Z_1[1 - \exp\left(-\frac{v}{v_0 Z_1^{2/3}}\right)] \tag{2.54}$$

Betz [30], Robinson [31], and Ziegler [29] gave similar empirical expressions.

As the ion velocity is further reduced, so that $v << v_0$, the ion's electron cloud is completely recovered and dynamically polarizes the medium as it goes through the target. In this low energy region the ion is basically considered as a neutral atom. Based on the dieletric theory, Lindhard [23,32] derived a low energy electronic stopping formula proportional to the ion velocity as

$$S_e = \xi_e \frac{8\pi e^2 a_0 Z_1 Z_2}{\left(Z_1^{2/3} + Z_2^{2/3}\right)^{3/2}} \frac{v}{v_0} \tag{2.55}$$

, where $\xi_e \sim Z_1^{1/6}$.

Firsov [33,34,35] also derived the same dependence of S_e on the ion velocity but with a different proportional constant.

Because of the uncertainty of the electronic stopping power, especially in the intermediate energy region, many (semi)empirical formula have been developed. Using a quantum theory, Brice [36] suggested a formula with three fitting coefficients compared with experimental data. Biersack and Haggmark [37] suggested a formula which combines the Bethe-Bloch and LSS formula in the following manner:

$$S_e = \frac{S_{e,LSS} S_{e,BB}}{S_{e,LSS} + S_{e,BB}} \tag{2.56}$$

, where $S_{e,LSS}$ is the Lindhard's stopping formula and $S_{e,BB}$ is the Bethe-Bloch formula modified to include the effective charge effect.

Recently, Ziegler et al. [38] suggested a semiempirical electronic stopping formula based on the new concept of the effective charge proposed by Brandt

and Kitagawa [39] and the local density approximation. This formula is summarized below.

- For protons

  1. if $E \geq 25$ keV/amu

$$S_p(E) = \frac{S_L S_H}{S_L + S_H} \tag{2.57}$$

, where

$$\begin{aligned} S_L &= aE^b + cE^d \\ S_H &= \frac{e}{Ef} \ln\left(\frac{g}{E} + hE\right) \end{aligned} \tag{2.58}$$

, where a, b, c, d, e, f, g, h are the fitting coefficients for each target.

  2. if $E < 25$ keV/amu

$$S_p(E) = \begin{cases} S_p(25\text{keV/amu})\left(\frac{E}{25}\right)^{0.45} & \text{if} \quad Z_2 > 6 \\ S_p(25\text{keV/amu})\left(\frac{E}{25}\right)^{0.25} & \text{if} \quad Z_2 \leq 6 \end{cases} \tag{2.59}$$

- For He ions

  1. if $E \geq 1$ keV/amu

$$S_{He}(E, Z_2) = S_p(E, Z_2) Z_{He}^2 \gamma_{He}^2 \tag{2.60}$$

, where the fractional effective charge, γ_{He} is given by

$$\gamma_{He}^2 = 1 - \exp\left[-\sum_{i=0}^{5} a_i (\ln E)^i\right] \tag{2.61}$$

, where

$$\begin{aligned} &a_0 = 0.2865, \quad a_1 = 0.1266, \quad a_2 = -0.001429 \\ &a_3 = 0.02402, \quad a_4 = -0.01135, \quad a_5 = 0.001475 \end{aligned} \tag{2.62}$$

2. if $E < 1$ keV/amu

$$S_{He}(E) = S_{He}(1\text{keV/amu})E^{0.5} \tag{2.63}$$

- For heavy ions ($Z_1 \geq 3$)

The effective ion velocity, y_r is given by

$$y_r = \frac{v_r}{v_0 Z_1^{2/3}} \tag{2.64}$$

, where v_r is ion's relative velocity with respect to the Fermi velocity of the target atom v_F and is given by

$$v_r = \begin{cases} v_1\left(1 + \frac{v_F^2}{5v_1^2}\right) & \text{if} \quad v_1 \geq v_F \\ \frac{3}{4}v_F\left(1 + \frac{2}{3}\frac{v_1^2}{v_F^2} - \frac{1}{15}\frac{v_1^4}{v_F^4}\right) & \text{if} \quad v_1 < v_F \end{cases} \tag{2.65}$$

1. if $y_r \geq \max(0.13,\ Z_1^{-2/3})$

$$S_{HI}(E, Z_2) = S_p(E, Z_2)Z_{HI}^2\gamma^2 \tag{2.66}$$

, where the fractional effective charge γ is given by

$$\gamma = q + (1-q)\frac{(v_0/v_F)^2}{2}\ln\left(1 + \left(\frac{2\Lambda v_F}{a_0 v_0}\right)^2\right) \tag{2.67}$$

, where Λ is the ion screening length, q is the ionization fraction, a_0 is the Bohr radius, and v_0 is the Bohr velocity($\frac{e^2}{\hbar}$). Λ is given by

$$\Lambda = \frac{0.67492a_0(1-q)^{2/3}}{Z_1^{1/3}(1 - \frac{1-q}{7})} \times \Lambda_{corr} \tag{2.68}$$

, where Λ_{corr} is the correction term for Λ and q is given by

$$\begin{aligned} q = 1 - \exp(0.803y_r^{0.3} &- 1.3167y_r^{0.6} \\ &- 0.38157y_r - 0.008983y_r^2) \end{aligned} \tag{2.69}$$

2. if $y_r < \max(0.13,\ Z_1^{-2/3})$

$$S_{HI} \propto E^{0.375} \quad \text{if} \quad Z_1 \leq 19, \text{and } Z_2 = 6, 14, 32 \qquad (2.70)$$
$$S_{HI} \propto E^{0.5} \quad \text{otherwise}$$

Ziegler et al. [38] estimated the average error of evaluating the electronic stopping cross section as 7.4 %. Fig. 2.9 shows the electronic stopping cross sections of various models for two different ion-target combinations.

2.2.2 Bragg's rule

Bragg [40] formulated a rule to determine the electronic stopping cross section of non-monatomic substances. Suppose that the target is composed of molecules A_mB_n, then the electronic stopping cross section of this target can be calculated from

$$S_e(A_mB_n) = mS_e(A) + nS_e(B) \qquad (2.71)$$

, where $S_e(A)$ and $S_e(B)$ are the electronic stopping cross section of the target A and B respectively. Bragg's rule says that if we try to know the energy loss in a compound, it is sufficient to know the energy losses in the elements making it up. It does not take into account of the presence of the chemical bond in molecules and solids. Nonetheless, at high ion energy($E > 1$ MeV/amu) it gives satisfactory results. An explanation of the Bragg rule's breakdown at low energy has been given in terms of the modified Firsov theory [41,42]. At ion velocities less than or on the order of the outer shell electron velocities, electrons of the outer shells of the target atoms make a significant contribution

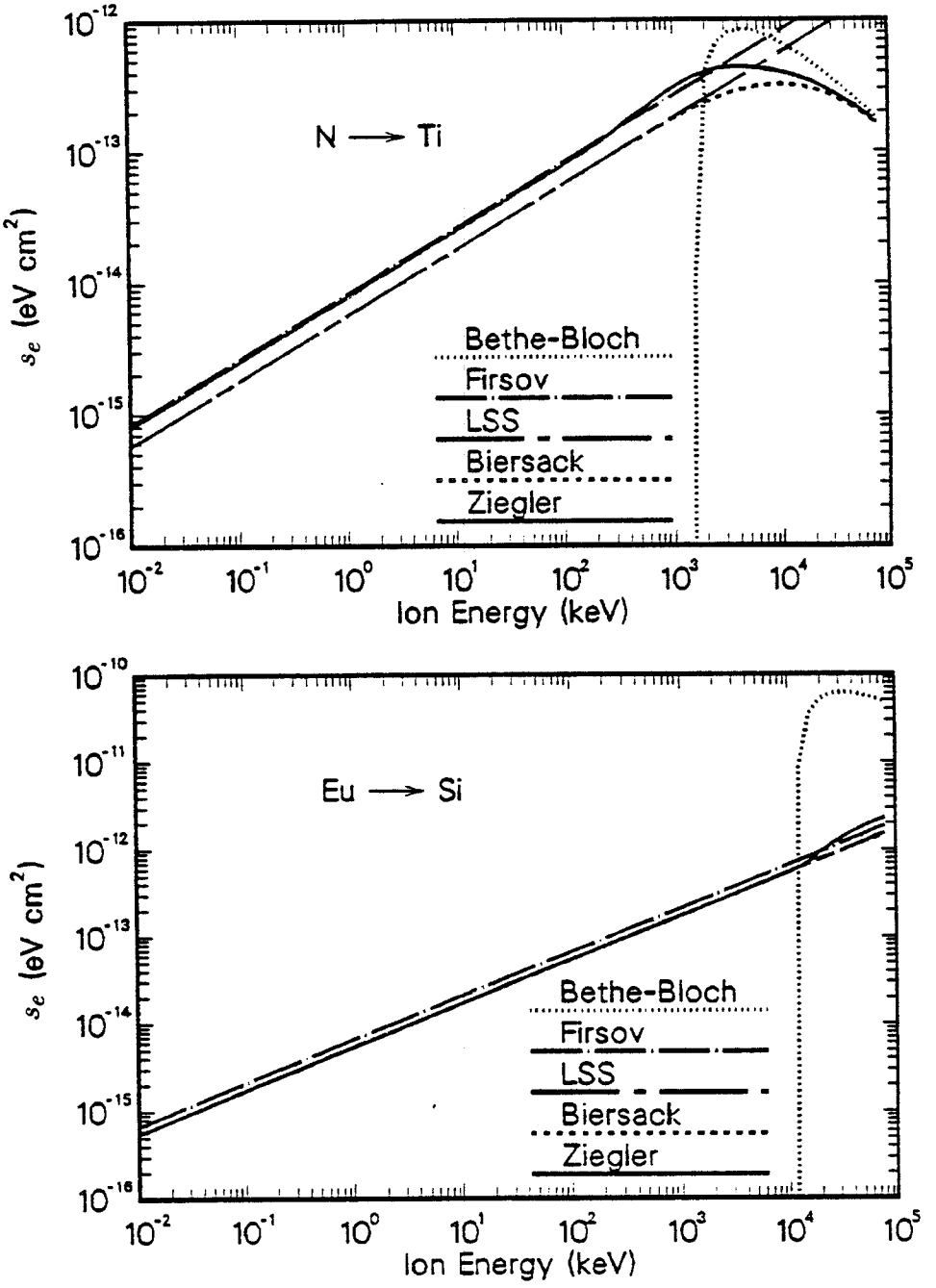

Figure 2.9: Electronic stopping cross section

to the electronic energy loss process. In compounds, the distribution of outer-shell electrons depends strongly on the type of bond between atoms of the constituent elements, by which the measured S_e for compounds is up to 20 % lower than the Bragg rule.

References

[1] N. Bohr, Phil. Mag. **25**, 10 (1913).

[2] N. Bohr, Phil. Mag. **30**, 581 (1915).

[3] M. Born and J. E. Mayer, Z. Phys. **75**, 1 (1932).

[4] L. H. Thomas, Proc. Cambridge Philos. Soc. **23** (1927).

[5] E. Fermi, Z. Phys. **48**, 73 (1929).

[6] I. M. Torrens, "Interatomic Potentials", Academic Press, New York, p. 32 (1972).

[7] N. Bohr, K. Dan. Vidensk. Selsk., Mat. Fys. Medd. **18**, No. 8 (1948).

[8] W. Lenz, Z. f. Physik **77**, 713 (1932).

[9] H. Jensen, Z. f. Physik **77**, 722 (1932).

[10] W. D. Wilson, L. G. Haggmark, J. P. Biersack, Phys. Rev. **15B**, 2458 (1977).

[11] N. Bohr, Phys. Rev. **58**, 654 (1940).

[12] N. Bohr, Phys. Rev. **59**, 270 (1941).

[13] O. B. Firsov, Zh. Eksp. Teor. Fiz. **32**, 1464 (1957).

[14] O. B. Firsov, Zh. Eksp. Teor. Fiz. **33**, 696 (1957).

[15] O. B. Firsov, Zh. Eksp. Teor. Fiz. **34**, 447 (1958).

[16] O. B. Firsov, JETP, Vol. **7**, 308 (1958).

[17] J. Lindhard, V. Nielsen, M. Scharff, K. Dan. Vidensk. Selsk., Mat. Fys. Medd. **36**, No. 10 (1948).

[18] J. P. Biersack, J. F. Ziegler, Springer Series in Electrophysics, Vol. **10** (Springer, Berlin, 1982), p. 122-156.

[19] M. T. Robinson, I. M. Torrens, Phys. Rev. **9B, 12**, 5008 (1974).

[20] H. A. Bethe, Ann. Phys. **5**, 325 (1930).

[21] F. Bloch, Ann. Phys. **16**, 287 (1933).

[22] L. D. Landau and E. M. Lifshitz, "Electrodynamics of Continuous Media"(Addison-Wesley, Reading, MA), p. 344-359.

[23] J. Lindhard, V. Nielsen, and M. Scharff, K. Dan. Vidensk. Selsk., Mat. Fys. Medd. **28**, No. 9 (1954).

[24] J. D. Jackson, "Classical Electrodynamics"(John-Wiley, New York, 1962), p. 636.

[25] H. A. Bethe, Ann. Phys. **89**, 1256 (1953).

[26] C. Moellor, Ann. Phys. **14**, 531 (1932).

[27] U. Fano, Ann. Rev. Nucl. Sci. **13**, 1 (1963).

[28] L. C. Northcliffe, Phys. Rev. **120**, 1744 (1960).

[29] Z. F. Ziegler, "Handbook of Stopping Cross Sections for Energetic Ions in All Elements" (Pergamon Press, New York), (1980).

[30] H. D. Betz, Rev. Mod. Phys. **44**, 465 (1972).

[31] M. T. Robinson, in "Proc. Symp. on the Physics of Irradiation Produced Voids", R. S. Nelson, ed., AERE Harwell Report AERE-R7934 (Jan. 1975).

[32] J. Lindhard, K. Dan. Vidensk. Selsk., Mat. Fys. Medd. **34**, No. 14 (1965).

[33] O. B. Firsov, JETP, Vol **5**, 1192 (1957).

[34] O. B. Firsov, JETP, Vol **6**, 534 (1958).

[35] O. B. Firsov, JETP, Vol **9**, 1076 (1959).

[36] D. K. Brice, Phys. Rev. **6**, 1971 (1972).

[37] J. P. Biersack and L. Haggmark, Nucl. Instr. and Meth. **174**, 257 (1980).

[38] Z. F. Ziegler, J. P. Biersack, U. Littmark, "Stopping and Range of Ions in Solids"(Pergamon Press, New York, 1985) Vol. **1**.

[39] W. Brandt and M. Kitagawa, Phys. Rev. **25B**, 5631 (1982).

[40] W. H. Bragg and R. Kleeman, Philos. Mag. **10**, 318 (1905).

[41] A. F. Burenkov and F. F. Komarov, Phys. Status Solidi **B79**, K161 (1977).

[42] A. F. Burenkov et al., Proc. Int. Conf. Atomic Collisions in Solids, 7th, Moskow, 1977. p. 193.

Chapter 3.

Range and Damage Distribution

3.1 Introduction

The stopping of ion in solids is basically a statistical process. In other words, each ion having exactly the same initial incidence parameters does not end with the same path, and this can result in a spatial distribution of ions in solid. This distribution function depends on the ion and target species, incident ion energy and the angle of incidence. Furthermore, the final distribution of damage produced by ion bombardment will be the average of the results of many incident ions.

The equation that describes the ion slowing down problem is the generalized transport equation [1,2,3,4,5,6] of the form:

$$\begin{aligned} & \frac{1}{v}\frac{\partial}{\partial t}\Phi(\vec{r},E,\vec{\Omega},t)+\vec{\Omega}\cdot\nabla\Phi(\vec{r},E,\vec{\Omega},t)+\Sigma_t(\vec{r},E,t)\Phi(\vec{r},T,\vec{\Omega},t) \quad (3.1) \\ = \; & Q(\vec{r},E,\vec{\Omega},t)+\frac{\partial}{\partial E}\left(S_e(\vec{r},E,t)\Phi(\vec{r},E,\vec{\Omega},t)\right) \\ + \; & \int_0^\infty dE'\int_{-1}^{1} d\vec{\Omega}'\Sigma_s(E'\rightarrow E,\vec{\Omega}'\rightarrow\vec{\Omega})\Phi(\vec{r},E',\vec{\Omega}',t) \end{aligned}$$

, where Φ is the particle flux, which is a function of position vector $\vec{r}$, energy E, direction vector $\vec{\Omega}$, and time t and Σ_t is the total cross section, Σ_s is the differential scattering cross section, Q is the particle source rate, and S_e is the electronic stopping cross section. This equation is derived from the particle conservation in phase space. It is a formidable problem to solve this equation

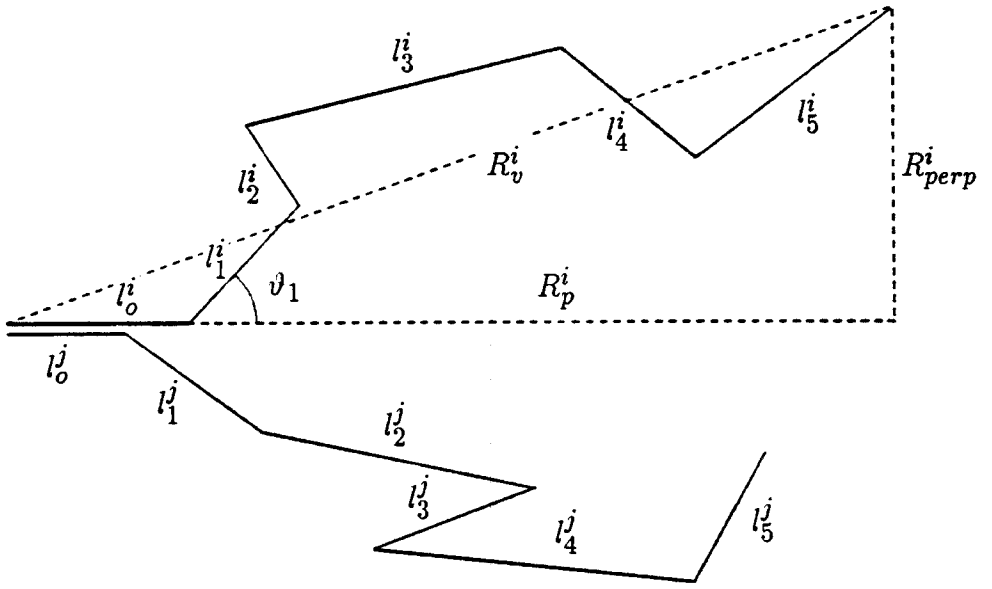

Figure 3.1: Schematic picture of the ion trajectories and various ranges

as it is formulated, so many authors have attacked the problem with a variety of approximations.

Before proceeding further, the various range concepts need to be defined. In Fig. 3.1 the paths of two typical ions are shown to illustrate the diversity of the individual trajectory. If we consider the path of the ith ion made up of a number of approximately linear segments between collisions with target atoms, then the total path length is given by

$$R^i = \sum_{j=0}^{m} l_j^i \tag{3.2}$$

, where the sum is terminated in the mth flight path at which the ion becomes trapped in the lattice. The average total path length is defined as

$$\overline{R} = \frac{1}{n} \sum_{i=1}^{n} R^i \tag{3.3}$$

for a number of n incident ions. The vector range R_v^i is the distance from the initial point of entry of the ion to its final resting point, whose average will be

$$\overline{R_v} = \frac{1}{n}\sum_{i=1}^{n} R_v^i \tag{3.4}$$

The penetration or the projected range R_p^i is the projection of the vector range onto the incident direction of the ion, which gives the average as

$$\overline{R_p} = \frac{1}{n}\sum_{i=1}^{n} R_p^i \tag{3.5}$$

Finally, the spread in stopping points perpendicular to the initial direction, R_{perp}^i is obtained through resolution of the vector range in perpendicular direction.

3.2 Range and damage distribution

The average total path length $\overline{R}$ can be calculated using a rather simple argument. The average energy loss of ion with energy E, when it moves a small path segment dR is given by

$$< dE >= N \int_{T_{min}}^{T_{max}} T d\sigma(E,T) dR \tag{3.6}$$

, which gives (the average sign is omitted from hereon.)

$$\frac{dE}{dR} = N \int_{T_{min}}^{T_{max}} T d\sigma(E,T) \tag{3.7}$$

, where N is the atomic density of the medium. The range is given by

$$\begin{aligned} R(E) &= \int_0^R dR = \int_0^E \frac{1}{(dE'/dR)} dE' \\ &= \frac{1}{N}\int_0^E \frac{dE'}{S(E')} \end{aligned} \tag{3.8}$$

In an analogous way, we can calculate the range straggling ΔR, using the energy straggling defined as

$$\overline{(\Delta E)^2} = N \int_{T_{min}}^{T_{max}} T^2 d\sigma(E,T) dR = N\Omega^2 dR \tag{3.9}$$

, which gives the average square fluctuation in the range, $(\Delta R)^2$ as

$$(\Delta R)^2 = \frac{1}{N^2} \int_0^E \frac{\Omega^2(E')}{S^3(E')} dE' \tag{3.10}$$

Lindhard, Scharff, and Schiott [7] treated the above method more rigorously to derive equations describing the relation between energy and range of ions in amorphous target, which has been called the specific energy loss method or LSS method. A number of assumptions, which corresponds to reality in many cases, underlie the LSS model:

- The target is amorphous, i.e. the crystalline effects are neglected.
- The energy transfer T can be divided into two parts; the energy transferred to the electrons of the medium T_e, and the energy transferred to the screened target nuclei through the repulsive interaction T_n. The two contributions to the total energy transfer are assumed independent in stopping process.
- Energy fluctuation in the stopping process is only due to the interaction with nuclei.
- The binary collision approximation is used, i.e. the scattering angle is related to T_n in a single-valued way.

- The energy T transferred to the target atom in a collision is much less than the ion's kinetic energy before collision, i.e. $T << E$.

Let's define $F(R,E)dR$ as the probability that the total path length traversed by an ion with energy E lies in the interval from R to $R+dR$. Obviously,

$$\int_0^\infty F(R,E)dR = 1 \tag{3.11}$$

and the average of the mth moment with respect to R is defined as

$$\overline{R^m} = \int_0^\infty F(R,E)R^m dR \tag{3.12}$$

The probability that the ion, after traversing a path δR, will transfer energy $\sum_i T_{ei}$ to the electrons and energy T_n to the target atom(recoil) is determined as $N\delta R d\sigma_{n,e}$, , where N is the target atomic density and $d\sigma_{n,e}$ is the differential cross section for the electronic and nuclear energy loss. If a collision takes place, then the probability that the ion has the total path R will be $F(R-\delta R, E-T_n-\sum_i T_{ei})$. If we multiply this by the collision probability $N\delta R d\sigma_{n,e}$, we get the contribution from each collision to the total probability for the range R. Then, the contributions from all collisions should be summed.

The probability that no collision takes place is $1-N\delta R\int d\sigma_{n,e}$. Then, the contribution of each case to the total probability for the range is expressed as $(1-N\delta R\int d\sigma_{n,e})F(R-\delta R,E)$. By summing the two contributions, we find an expression for $F(R,E)$ as

$$\begin{aligned} F(R,E) &= N\delta R\int d\sigma_{n,e}F(R-\delta R, E-T_n-\sum_i T_{ei}) \\ &+ (1-N\delta R\int d\sigma_{n,e})F(R-\delta R,E) \end{aligned} \tag{3.13}$$

As $\delta R \rightarrow 0$, above expression becomes

$$\frac{\partial F(R,E)}{\partial R} = N \int d\sigma_{n,e}\{F(R, E - T_n - \sum_i T_{ei}) - F(R,E)\} \tag{3.14}$$

Eq.(3.14) derived by LSS, determines the fundamental integral equation for the range probability distribution. Multiplying this equation by R^m and integrating by parts, one obtains

$$m\overline{R^{m-1}}(E) = N \int d\sigma_{n,e}\{\overline{R^m}(E) - \overline{R^m}(E - T_n - \sum_i T_{ei})\} \tag{3.15}$$

Eq.(3.15) can be used to calculate various moments of the range. The mean ion range is found from the above relation as

$$1 = N \int d\sigma_{n,e}\{\overline{R}(E) - \overline{R}(E - T_n - \sum_i T_{ei})\} \tag{3.16}$$

To obtain an approximate solution for the expression of $\overline{R}$, we can expand eq.(3.16) as a Taylor series in $T = T_n + \sum_i T_{ei}$. By taking only the first term in this expansion, one gets

$$\frac{d\overline{R_1}(E)}{dE} = \frac{1}{NS(E)} \tag{3.17}$$

or

$$\overline{R_1}(E) = \int_0^E \frac{dE'}{NS(E')} \tag{3.18}$$

, where $S(E) = S_n(E) + S_e(E)$ is the total stopping cross section. Note that this is the same as eq.(3.8) obtained from a rough calculation for the average total path length. If the second term of the expansion is included, one arrives at a second order differential equation,

$$1 = NS(E)\frac{d\overline{R_2}(E)}{dE} - \frac{1}{2}N\Omega^2(E)\frac{d^2\overline{R_2}(E)}{dE^2} \tag{3.19}$$

, where $\Omega^2(E) = \int d\sigma_{n,e} T^2$ is the energy transfer straggling. This equation can be solved for $\overline{R_2}$ as

$$\overline{R_2}(E) = \int_0^E \frac{dE'}{NS(E')} \left\{ 1 + \frac{\Omega^2(E')}{2} \frac{d}{dE'} \left(\frac{1}{S(E')} \right) \right\} \tag{3.20}$$

To obtain the mean square fluctuation of the total path length, $\overline{\Delta R^2}(E) = \overline{R^2}(E) - \overline{R}^2(E)$, one can multiply eq.(3.16) by $2\overline{R}(E)$ and subtract this from the second moment with respect to R, given in eq.(3.15) to get

$$\begin{aligned} & \int d\sigma_{n,e} \{ \overline{\Delta R^2}(E) - \overline{\Delta R^2}(E - T_n - \sum_i T_{ei}) \} \\ = & \int d\sigma_{n,e} \{ \overline{R}(E) - \overline{R}(E - T_n - \sum_i T_{ei}) \}^2 \end{aligned} \tag{3.21}$$

If the above expression is expanded in T and only the first term is used, one gets

$$S(E) \frac{d(\overline{\Delta R^2})_1}{dE} = \Omega^2(E) \left(\frac{d\overline{R_1}(E)}{dE} \right)^2 \tag{3.22}$$

or

$$\left(\overline{\Delta R^2} \right)_1 = \frac{1}{N^2} \int_0^E \frac{\Omega^2(E')}{S^3(E')} dE' \tag{3.23}$$

Again the same expression was obtained from the simple calculation, eq.(3.10). If the second term of the expansion is included, one obtains an expression for the second approximation of the mean square fluctuation of the total path length $\left(\overline{\Delta R^2} \right)_2$, and so forth.

Lindhard et al. also derived the expressions for the projected range R_p and the projected range straggling $\overline{\Delta R_p^2}$. By analogy with eq.(3.16), one can get the integral equation for the projected range as

$$1 = N \int d\sigma_{n,e} \{ \overline{R_p}(E) - \overline{R_p}(E - T) \cos \vartheta \} \tag{3.24}$$

, where ϑ is the scattering angle of the ion with energy E in the laboratory system. Using only the first term in the expansion with respect to T, one obtains the first approximation for R_p, i.e. $\overline{R_{p1}}$

$$1 = \overline{R_{p1}}(E)N\int d\sigma_{n,e}(1-\cos\vartheta) + \frac{d\overline{R_{p1}}(E)}{dE}N\int d\sigma_{n,e}T\cos\vartheta \qquad (3.25)$$

If the new variables λ_{tr} and S_{tr} are introduced as

$$\begin{aligned} \frac{1}{\lambda_{tr}} &= N\int d\sigma_{n,e}(1-\cos\vartheta) \\ S_{tr} &= \int d\sigma_{n,e}T\cos\vartheta \end{aligned} \qquad (3.26)$$

, then eq.(3.25) becomes

$$1 = \frac{\overline{R_{p1}}(E)}{\lambda_{tr}(E)} + \frac{d\overline{R_{p1}}(E)}{dE}NS_{tr}(E) \qquad (3.27)$$

This equation has the solution of

$$\overline{R_{P1}}(E) = \int_0^E \frac{dE'}{NS_{tr}(E')}\exp\left(\int_E^{E'}\frac{dE''}{\lambda_{tr}(E'')NS_{tr}(E'')}\right) \qquad (3.28)$$

Lindhard et al. calculated the total path length and the projected range along with stragglings up to the second order approximation using the Thomas-Fermi potential and with the electronic energy loss. In the calculations, reduced energy ε and reduced range ρ were used, which are defined as

$$\begin{aligned} \varepsilon &= \frac{aM_2}{Z_1Z_2e^2(M_1+M_2)}E \\ \rho &= N\pi a^2\Lambda R \end{aligned} \qquad (3.29)$$

, where E is the energy of the ion and R is the corresponding range.

Lindhard et al. [8] also derived an integral equation , which describes the damage in the forms of the deposited energy, the displacement and other relevant quantities induced by ion bombardment. If one denotes such a quantity

by Φ, the equation which governs the final average value of Φ due to the ions with energy E can be obtained with a similar argument as the range, i.e. for the like atoms

$$\int d\sigma_{n,e}\{\overline{\Phi}(E-T)-\overline{\Phi}(E)+\overline{\Phi}(T_n-U)+\sum_i \overline{\Phi}_e(T_{ei}-U_i)\}=0 \quad (3.30)$$

, where U is the binding energy of the atom in the lattice and U_i equals the ionization energy of the ith ionized electron in the collision. Usually, the damage produced by the ionized electrons is small and can be neglected. If the ion is different from the target atom, one can get the expression

$$\int d\sigma_{n,e}\{\overline{\Phi}_1(E-T)-\overline{\Phi}_1(E)+\overline{\Phi}_1(T_n-U)+\sum_i \overline{\Phi}_e(T_{ei}-U_i)\}=0 (3.31)$$

With similar approximations used in the range calculations Lindhard et al. solved the above equations for the Thomas-Fermi potential and found that if $\overline{\Phi}(E)$ equals the total deposited energy and denoting $\overline{\nu}(E)$ the deposited energy in nuclear collisions and $\overline{\eta}(E)$ the deposited energy in the electronic ionization and excitation, then $\overline{\Phi}(E)=\overline{\nu}(E)+\overline{\eta}(E)$, and a simple formula can be used to fit the obtained solution. Lindhard et al. suggested the expression in the reduced unit as

$$\overline{\nu}(E)=\varepsilon(1+kg(\varepsilon))^{-1} \quad (3.32)$$

, where k is the proportional constant in LSS electronic stopping formula in reduced units.

The LSS method is rather limited for obtaining the higher order moments, , which are necessary to construct the actual distribution functions. Winterbon, Sigmund, and Sanders [9,10,11] generalized the LSS methods, and they

introduced the vector range probability distribution instead of the total path length, which had been used in LSS method. First, consider the case when the incident ion is the same type as the target atom. If a function $F(E,\vec{\Omega},\vec{r})$ is defined as the probability that an ion with initial energy E and the incident direction $\vec{\Omega}$ comes to rest at a position denoted by a vector $\vec{r}$ from its starting point and generalizing the argument in LSS method, one gets the expression as

$$\begin{aligned} -\vec{\Omega}\cdot\nabla F(E,\vec{\Omega},\vec{r}) &= N\int d\sigma\{F(E,\vec{\Omega},\vec{r})-F(E-T,\vec{\Omega}',\vec{r})\} \\ &+ NS_e(E)\frac{\partial F(E,\vec{\Omega},\vec{r})}{\partial E} \end{aligned} \tag{3.33}$$

with

$$\int d^3\vec{r}F(E,\vec{\Omega},\vec{r})=1 \tag{3.34}$$

, where $\vec{\Omega}'$ is the direction vector of the scattered ion in laboratory system. If one integrates the above equation over the y and z, one gets

$$\begin{aligned} -\mu\frac{\partial F(E,\mu,x)}{\partial x} &= N\int d\sigma\{F(E,\mu,x)-F(E-T,\mu',x)\} \\ &+ NS_e(E)\frac{\partial F(E,\mu,x)}{\partial E} \end{aligned} \tag{3.35}$$

, where μ is the cosine of the incident angle with respect to the x axis. $F(E,\mu,x)$ is then expanded in Legendre polynomials as

$$F(E,\mu,x)=\sum_k(2k+1)P_k(\mu)F_k(E,x) \tag{3.36}$$

, which gives the expression along with eq.(3.35)

$$\begin{aligned} &-k\frac{\partial F_{k-1}(E,x)}{\partial x}-(k+1)\frac{\partial F_{k+1}(E,x)}{\partial x} \\ &= (2k+1)\left(S_e\frac{\partial F_k(E,x)}{\partial E}+N\int d\sigma\{F_k(E,x)-P_k(\mu)F_k(E-T,x)\}\right) \end{aligned} \tag{3.37}$$

If the nth moment of $F_k(E,x)$ over x is defined as

$$F_k^n(E) = \int dx\ x^n F_k(E,x) \tag{3.38}$$

and taking the nth moment of the eq.(3.37), one obtains

$$\begin{aligned} & \frac{n}{2k+1}\{kF_{k-1}^{n-1}(E) + (k+1)F_{k+1}^{n-1}(E)\} \\ = \ & S_e\frac{\partial F_k^n(E)}{\partial E} + N\int d\sigma\{F_k^n(E) - P_k(\mu)F_k^n(E-T)\} \end{aligned} \tag{3.39}$$

Sigmund et al. [10] solved the above equation for the first and second moment in the case of equal ion-target species. Gibbons et al. [12] solved this equation for the general ion-target combinations up to the third moment with a different numerical technique. Winterbon [9,13] reduced the above equation to a set of algebraic equations and thus attained more accuracy in the solution up to the fifth order.

The equation which governs the deposited energy can be obtained with a similar method with LSS. Consider the function $F(\vec{r},\vec{v})$, which is defined as the average energy deposited at $\vec{r}$ due to an ion with an initial position of $\vec{r} = \vec{0}$ and energy $E = \frac{1}{2}M_1v^2$. Clearly this function should satisfy

$$\int d^3\vec{r}F(\vec{r},\vec{v}) = E \tag{3.40}$$

The integral equation for the energy deposition $F(\vec{r},\vec{v})$ has the form

$$-\frac{\vec{v}}{v}\frac{\partial F(\vec{r},\vec{v})}{\partial \vec{r}} = N\int d\sigma\{F(\vec{r},\vec{v}) - F(\vec{r},\vec{v}') - F_r(\vec{r},\vec{v}'')\} + \frac{S_e}{v}\frac{\partial F(\vec{r},\vec{v})}{\partial \vec{v}} \tag{3.41}$$

, where $F_r(\vec{r},\vec{v}'')$ is for matrix recoils, which subsequently follows the relation

$$\begin{aligned} -\frac{\vec{v}}{v}\frac{\partial F_r(\vec{r},\vec{v})}{\partial \vec{r}} \ &= \ N\int d\sigma\{F_r(\vec{r},\vec{v}) - F_r(\vec{r},\vec{v}') - F_r(\vec{r},\vec{v}'')\} \\ &+ \ \frac{S_e}{v}\frac{\partial F_r(\vec{r},\vec{v})}{\partial \vec{v}} \end{aligned} \tag{3.42}$$

If the same moment method is used in deriving the range equations, one gets

$$\frac{n}{2k+1}\{kF_{k-1}^{n-1}(E)+(k+1)F_{k+1}^{n-1}(E)\}=S_e\frac{\partial F_k^n(E)}{\partial E} \qquad (3.43)$$
$$+N\int d\sigma\{F_k^n(E)-F_k^n(E')P_k(\mu')-F_{r,k}^n(E'')P_k(\mu'')\}$$

and

$$\frac{n}{2k+1}\{kF_{r,k-1}^{n-1}(E)+(k+1)F_{r,k+1}^{n-1}(E)\}=S_e\frac{\partial F_{r,k}^n(E)}{\partial E} \qquad (3.44)$$
$$+N\int d\sigma\{F_{r,k}^n(E)-F_{r,k}^n(E')P_k(\mu')-F_{r,k}^n(E'')P_k(\mu'')\}$$

, where μ' and μ'' are the cosines of the scattering angles in the laboratory system for the incident ion and recoil atom, respectively. The fact that the deposited energy distributions are much less symmetric than the range distributions, and consequently require the moments much higher than those of the range, indicates the importance of the numerical accuracy in solving the above equations.

Brice [14,15,16,17,18,19] first formulated the transport equations governing the ion distribution during slowing down process and solved them for the first and second moment to obtain the spatial distribution of the ions as a function of their instantaneous energy. These distributions, which are all assumed to be Gaussian, have been used to calculate the depth distribution of the energy deposited into atomic displacements or electronic process.

Williams [2,3,4] derived a set of linear, coupled Boltzmann transport equations which describe the distributions of the projectile and recoil atoms in space, time, and energy. He showed that LSS equation is just a partially adjointed equation in energy and direction to the usual, or the forward form of the Boltzmann equation. He also showed the merits of using the forward form,

which is familiar and well understood in the neutron transport field. One of the advantages of using the forward form is the applicability of the method to multi-layer problem.

3.3 Displacement production

When the ion makes a collision with a target atom, it transfers an energy T to the struck atom. If this transferred energy is greater than some threshold energy(E_d), this recoil atom will escape from its equilibrium lattice site leaving a vacancy behind to make further displacements. The concentration of the displaced atoms by the ion bombardment with energy E and fluence Φ is given as

$$C_d = \Phi \int_{E_d}^{T_{max}} \nu(T) \frac{d\sigma}{dT} dT \tag{3.45}$$

, where $\nu(T)$ is the average number of displaced atoms by a recoil with energy T and T_{max} is the maximum energy transferred.

Kinchin and Pease [20] developed a model to calculate $\nu(E)$ with following assumptions.

- Atomic collisions are elastic and hard sphere-like.
- The cascade proceeds as a series of binary collisions.
- These collisions are independent of each other and the periodicity of crystal structure is neglected.
- No energy is passed to the lattice such that

$$E_1 = E_1' + E_2' \tag{3.46}$$

, where E_1 and E_1' are the energies of incident atom before and after collision respectively, and E_2' is the energy of recoil atom after collision.

- A stationary atom which receives less than a threshold energy E_d is not displaced. Similarly, if an incident atom emerges from collision with $E_1' < E_d$, it does not contribute further to the cascade.

Fig. 3.2 shows the diagrammatic representation of Kinchin-Pease model, and the expression for $\nu(E)$ is

$$\nu(E) = \begin{cases} \frac{E}{2E_d} & \text{if} \quad 2E_d \leq E \\ 1 & \text{if} \quad E_d \leq E < 2E_d \\ 0 & \text{if} \quad E < E_d \end{cases} \tag{3.47}$$

With the assumptions that E_d is lost at every collision such that

$$E_1 = E_1' + E_2' + E_d \tag{3.48}$$

and that both atoms move further after collision regardless of their energies, Snyder and Neufeld [21,22] estimated $\nu(E)$ as

$$\nu(E) = \begin{cases} 0.561\frac{E}{E_d} & \text{if} \quad 2E_d \leq E \\ ln(\frac{E}{E_d}) & \text{if} \quad E_d \leq E < 2E_d \\ 1 & \text{if} \quad E < E_d \end{cases} \tag{3.49}$$

Lindhard et al. [8] used the more realistic Thomas-Fermi potential to estimate the differential scattering cross section instead of the hard sphere collision and included the electronic energy loss to get

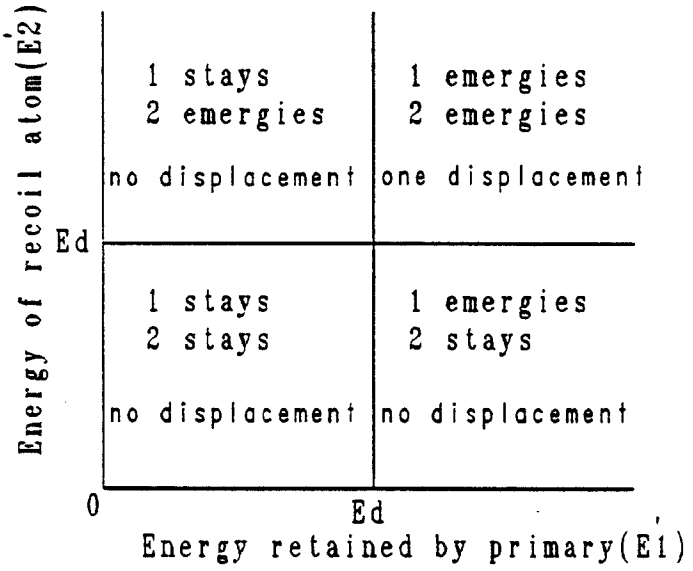

Figure 3.2: Diagrammatic representation of the Kinchin-Pease model for displacement production

$$\nu(E) = \xi(E)\frac{E}{2E_d} \tag{3.50}$$

, where

$$\xi(E) = \frac{1}{1 + 0.13(3.4\varepsilon^{1/6} + 0.4\varepsilon^{3/4} + \varepsilon)} \tag{3.51}$$

, where ε is the reduced energy of the recoil atom.

Robinson [23] suggested a similar expression as

$$\nu(E) = \begin{cases} 0.8\frac{E_\nu}{2E_d} & \text{if} \quad 2E_d \leq E_\nu \\ 1 & \text{if} \quad E_d \leq E_\nu < 2E_d \\ 0 & \text{if} \quad E_\nu < E_d \end{cases} \tag{3.52}$$

, where

$$E_\nu = \frac{E}{1 + k_d g(\varepsilon_d)} \tag{3.53}$$

, where

$$k_d = 0.1334 Z_2^{2/3} M_2^{-1/2} \tag{3.54}$$

$$g(\varepsilon_d) = \varepsilon_d + 0.40244 \varepsilon_d^{3/4} + 3.4008 \varepsilon_d^{1/6}$$

, where $\varepsilon_d = 0.01014 Z_2^{-7/3} E$.

The simple cascade analysis, even modified to account for a realistic energy transfer cross section or for the electronic energy loss during slowing down, implicitly assumes that the solid consists of a random arrays of atoms (amorphous). However, when the cascade is considered to occur in the real crystalline solid, two important phenomena appear , i.e. focusing and channeling. Focusing refers to the transfer of energy to a row of atoms by nearly head-on collisions. Channeling is the complementary process whereby atoms move long distances in the solid along open directions in the crystalline structure. In this case the moving atom is kept in its channel by glancing collisions with the atomic rows that serve as walls. Focusing and channeling affect both the number and configuration of displaced atoms in a solid. First, atoms moving along the crystallographic direction favorable to the focusing or channeling lose energy only by glancing collisions with the atoms consisting the axis of motion. The energy transfer in these collisions is well below E_d, resulting in that more energy is dissipated in subthreshold collisions. Consequently, $\nu(E)$ is smaller when the crystal effects are considered than when the atom moves in a random array of atoms. Second, the focused or channeled atoms are able to move much larger distances before coming to rest than in a random lattice, resulting in the spread of the damaged region. Because the maximum energy

at which focusing can occur is relatively low, focusing is important only in low energy cascades or at the very end of a high energy cascade. On the contrary, channeling is favorable at high energy.

Oen and Robinson [24] derived a formula for $\nu(E)$ as

$$\nu(E) = \frac{1-P}{1-2P}\left(\frac{E}{2E_d}\right)^{1-2P} - \frac{P}{1-2P} \tag{3.55}$$

, where $P(E)$ is the probability of the occurrence of focusing and channeling. A value of 0.07 was used in order to obtain a quantitative agreement with the experimental measurements.

References

[1] D. E. Bartine, R. G. Alsmiller, Jr., F. R. Mynatt, W. W. Engle Jr., and J. Barish, Nucl. Sci. Eng. **48**, 159 (1972).

[2] M. M. R. Williams, J. Phys. A, **9**, 771 (1976).

[3] M. M. R. Williams, Rad. Effect **37**, 131 (1978)

[4] M. M. R. Williams, Progress Nucl. Energy **3**, 1 (1978).

[5] J. J. Hoffman, H. L. Dodds, and D. K. Holmes, Nucl. Sci. Eng. **68**, 55 (1978).

[6] P. S. Chou and N. M. Goniem, Nucl. Instr. and Meth. **B9**, 209 (1985).

[7] J. Lindhard, M. Scharff, H. E. Schiøt, K. Dan. Vidensk. Selsk., Mat. Fys. Medd. **33**, No. 14 (1963).

[8] J. Lindhard, V. Nielsen, M. Scharff, and P. V. Thomsen, K. Dan. Vidensk. Selsk., Mat. Fys. Medd. **33**, No. 10 (1963).

[9] K. B. Winterbon, "Ion Implantation Range and Energy Deposition Distribution", Vol. **2**, IFI/Plenum, New York (1975).

[10] P. Sigmund, M. T. Mathies, and D. L. Philips, Rad. Effect **11**, 39 (1979).

[11] J. B. Sanders, Can. J. Phys. **46**, 455 (1968).

[12] J. F. Gibbons, W. S. Johnson, and S. W. Mylrorie, "Projected Range Statistics", Powden, Hutc. and Ross, Inc. (1975).

[13] K. B. Winterbon, Rad. Effect **13**, 215 (1972).

[14] D. K. Brice, Appl. Phys. Lett. **16**, 1034 (1970).

[15] D. K. Brice, Rad. Effect **6**, 77 (1970).

[16] D. K. Brice, Rad. Effect **11**, 227 (1971).

[17] D. K. Brice, J. Appl. Phys. **46**, 3385 (1975).

[18] D. K. Brice, SAND75-0622; Sandia Lab. Albuquerque, New Mexico (1977).

[19] D. K. Brice, "Ion Implantation Range and Energy Deposition Distributions", Vol. **1**, IFI/Plenum, New York (1975).

[20] G. H. Kinchin and R. S. Pease, Rep. Progr. Phys. **18**, 1 (1955).

[21] W. S. Snyder and J. S. Neufeld, Phys. Rev. **97**, 1636 (1955).

[22] W. S. Snyder and J. S. Neufeld, Phys. Rev. **99**, 1326 (1955).

[23] M. T. Robinson, "Nuclear Fission Reactors", British Nuclear Energy Society, London, p. 364 (1970).

[24] O. S. Oen and M. T. Robinson, Appl. Phys. Lett. **2**, 83 (1963).

Chapter 4.

Ion-Solid Interaction

4.1 Sputtering

Sputtering is defined as the removal of target atoms due to energetic particle bombardment on the solid surface. The incident particles may be ions, neutral atoms, neutrons, electrons, or energetic photons. However, this work is confined to the sputtering by energetic ion bombardment. Furthermore, we are only concerned with the physical sputtering (or knock-on sputtering), in which a transfer of kinetic energy from the incident particle to target atoms causes the sputtering in contrary to the chemical sputtering, where the atoms are removed from the target surface via electronic processes.

In sputtering of elemental target, the sputtering yield Y is defined as the average number of target atoms removed from solid surface per incident particle. For multicomponent target, besides the total sputtering yield Y the partial sputtering yield Y_i is defined as the average number of ith element removed per incident particle such that

$$Y = \sum_i Y_i \tag{4.1}$$

For comparison with sputtering yields of the corresponding elemental target, component sputtering yield Y_i^c is defined as

$$Y_i^c = \frac{Y_i}{C_i^s} \tag{4.2}$$

, where C_i^s is the atomic fraction of element i on the surface.
Furthermore, the particles removed from a solid surface by sputtering are emitted with a distribution in energy E and emission angle Ω, which is described by the differential sputtering yield $\frac{\partial Y_i}{\partial E}$ and $\frac{\partial^2 Y_i}{\partial \Omega^2}$ for ith component.

The knock-on sputtering can be described by elastic collision in the surface layers of a solid. The processes are the same as those leading to radiation damage in the bulk of the target. If an incident ion with sufficient energy makes a collision with a target atom, it can create a primary knock-on atom, which initiates a collision cascade. It is convenient to distinguish between three qualitatively different regimes, i.e. the few collision regime, the linear cascade regime, and the spike regime. In the few collision regime, the bombarding ion transfers energy to target atoms which, possibly after having undergone a (small) number of further collisions, are ejected through the surface if energetic enough to overcome the surface binding energy. This is particularly important close to the sputtering threshold and for light ions, where sufficient energy for the creation of a regular collision cascade is not available. In the linear cascade regime, the incident ion makes a number of collisions with target atoms, and transfer sufficient energy to several recoils to allow them to remove further target atoms from their lattice sites. As a result, large collision cascades can be developed, however, moving target atoms collide only with target atoms at rest. In spike regime, the cascades leading to the sputtering are very dense and begin to overlap resulting that a major part of the atoms within the cascade volume are released from their lattice sites and set in motion. These three regimes are shown in Fig. 4.1 [1].

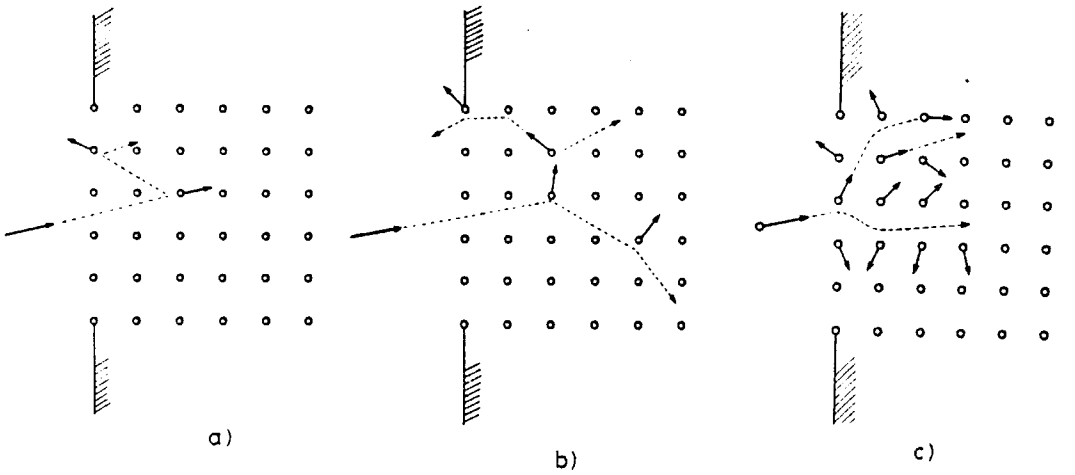

Figure 4.1: Three regimes of knock-on sputtering: (a) Few collision regime (b) Linear cascade regime (c) Spike regime [1]

It has often been claimed that energy transfer factor Λ given by

$$\Lambda = \frac{4M_1M_2}{(M_1+M_2)^2} \tag{4.3}$$

should be an important factor in the few collision regime. In fact, Bohdansky et al. [2] showed that yields of a number of target materials for incident H, D, He^3, and He^4 in the range of $0.1 - 10$ keV could be scaled together if the energy axis is chosen as E/U, where U is the surface binding energy. Especially, sputtering by light ions has recently been reviewed by Roth [3] and Littmark and Fedder [4]. The linear cascade regime is the one treated in most detail theoretically [5]. This regime is characterized by the energy deposition per unit depth, which can be typically applied to the ion energy for keV and low MeV region except for heaviest ions. In the spike regime,

sputtering yield is associated with a temperature deduced from the energy deposited per unit volume. This regime is often called the non-linear cascade regime because the sputtering yield of molecular ion bombardment is not just a linear superposition of atomic sputtering yield [6,7]. The spike effect has been reviewed in great detail by Thompson [8,9].

In the following section, the sputtering theory for the elemental target in the linear cascade regime will be reviewed and subsequently the sputtering for the multicomponent target will be briefly discussed.

4.1.1 Sputtering of elemental target

The collision cascade initiated by incident particles can be best described by transport equation, from which a number of averages over many cascades with identical macroscopic parameters may be calculated. The first order asymptotic solutions have been obtained by Sigmund [5] for the linear cascade regime in an amorphous (or polycrystalline) solids. Sigmund derived an expression for the sputtering yield Y for the ion bombardment with energy E and incidence angle θ as

$$Y = \Lambda_s F_D(E, \theta, 0) \tag{4.4}$$

, where $F_D(E, \theta, 0)$ is the energy deposition density at the surface in the form of nuclear collision and the material parameter Λ_s is expressed as

$$\Lambda_s = \frac{\Gamma_m}{2} \int \frac{dE'}{E'|dE'/dx|} \int d(\cos\theta')|\cos\theta'|P(E', \theta') \tag{4.5}$$

, where Γ_m is a constant which depends only weakly on the exponent m of the power law potential and $P(E', \theta')$ is the probability for an atom with energy

E' and angle θ' with surface normal to escape from the surface. With the nuclear stopping cross section $S_n(E')$ for the same kind of atoms as

$$S_n(E') = \frac{1}{1-m} C_m E'^{1-2m} \tag{4.6}$$

and planar surface barrier such as

$$P(E', \theta') = \begin{cases} 1 & \text{if} \quad E' \cos^2 \theta' > U \\ 0 & \text{if} \quad E' \cos^2 \theta' < U \end{cases} \tag{4.7}$$

, then Λ_s can be expressed as

$$\Lambda_s = \frac{\Gamma_m}{8(1-2m)} \frac{1}{N C_m U^{1-2m}} \tag{4.8}$$

, where N is the target atomic density and C_m is a function of exponent m, Z_1, Z_2, M_1, and M_2. Sigmund [10] suggested to use $m = 0$ because most of the atoms involved in the sputtering phenomena are in the low energy region. Furthermore, if the energy deposition density F_D is expressed as

$$F_D(E, \theta, 0) = \alpha N S_n(E) \tag{4.9}$$

, then one finally gets

$$Y = \frac{0.42}{U} \alpha S_n(E) \tag{4.10}$$

, where α is a dimensionless function of incidence angle θ and mass ratio M_2/M_1, and $S_n(E)$ is the nuclear stopping cross section of incident ion with energy E in the unit of eVÅ^2. Fig. 4.2 shows the α function deduced from measurements for Si, Cu, Ag, and Au with normal incidence [11].

Sigmund also got the expression for the differential yield as

$$\frac{d^3 Y}{dE_s d^2\Omega_s} = F_D(E, \theta, 0) \frac{\Gamma_m}{4\pi} \frac{1-m}{N C_m} \frac{E_s}{(E_s + U)^{3-2m}} \cos \theta_s \tag{4.11}$$

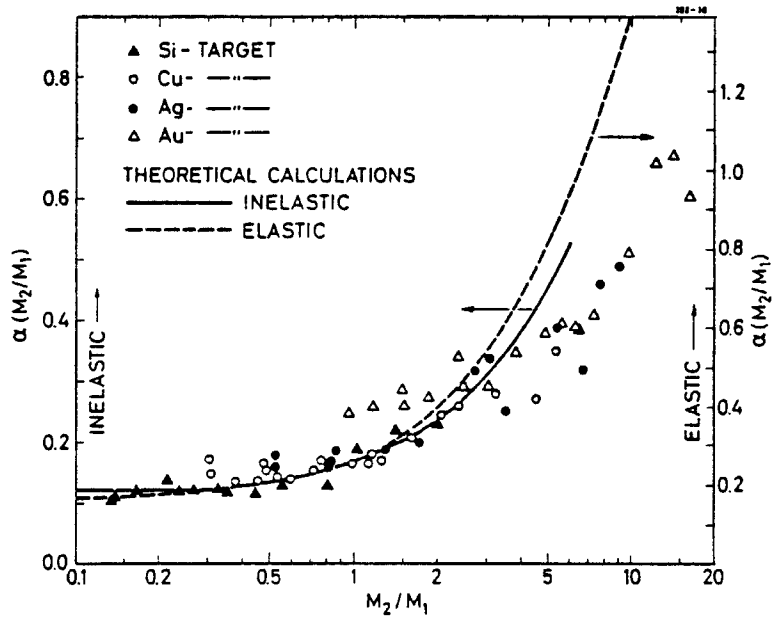

Figure 4.2: Experimental and theoretical values of the function $\alpha(M_2/M_1)$ [11]

, where E_s and θ_s are the energy and emission angle of a sputtered particle. With $m = 0$ again, he got

$$\frac{d^3Y}{dE_s d^2\Omega_s} \propto \frac{E_s}{(E_s + U)^3} \cos\theta_s \tag{4.12}$$

, which shows that the energy distribution of sputtered particles exhibits a maximum at $E_s = \frac{U}{2}$ and E_s^{-2} behavior for higher energy tail. Furthermore, the angular distribution shows the cosine distribution, which is a result of the isotropically distributed recoil atom flux in the derivation. Hence, deviation from such a distribution will signal deviations from isotropy of collision cascade. Such deviations are clearly seen at low energy, where angular distributions are under-cosine or even heart-shaped [12,13]. At somewhat higher energy the distribution becomes cosine-like, but at still higher energies. they become over-cosine [14].

After Sigmund's simple cascade theory, there have been many attempts to correct the assumptions and simplifications. For example, the electronic stopping correction [15], the effect of bulk binding forces [16,17], the effect of target surface [18], and the anisotropy of recoil flux [19] have been examined. Furthermore, with the help of extensive sputtering data, there have appeared several (semi)empirical formula especially in conjunction with the plasma interaction with the fusion first wall materials [2,20,21,22].

4.1.2 Sputtering of multicomponent target

Sputtering of multicomponent target is distinguished by the behavior **preferential sputtering** from the sputtering of elemental target. Preferential sputtering is said to occur when the composition of the sputtered particles differs from that of the outermost layers of the target, i.e.

$$\frac{Y_j}{Y_i} \neq \frac{C_j^s}{C_i^s} \qquad \text{or} \qquad Y_i^c \neq Y_j^c \tag{4.13}$$

, where $C_{i,j}^s$ is the surface composition of i,jth element in the target theoretically defined as

$$C_{i,j}^s = \frac{1}{Y_{i,j}} \int_0^\infty C_{i,j}(x) y_{i,j}(x) dx \tag{4.14}$$

, where $y_{i,j}(x)dx$ is the contribution to $Y_{i,j}$ from a layer dx at depth x and $C_{i,j}(x)$ is the concentration of species i,j at x.

Due to the preferential sputtering, target surface gradually becomes enriched or depleted with one component and finally a steady state will be reached, in which the composition of the sputtered flux is the same as that

of the bulk because mass should be conserved. Hence, in steady state the following expression should hold, i.e.

$$\frac{Y_j^\infty}{Y_i^\infty} = \frac{C_j^b}{C_i^b} \tag{4.15}$$

, where $C_{i,j}^b$ is the bulk concentration of i, jth element.

The origin of the preferential sputtering is said to be the mass and binding energy difference between constituent elements in the target. Qualitatively speaking, the component with smaller mass and lower binding energy is preferentially sputtered. Sigmund [1] derived an expression which describes the preferential sputtering in a binary alloy for the linear cascade regime as

$$\frac{Y_A^c}{Y_B^c} = \left(\frac{M_B}{M_A}\right)^{2m} \left(\frac{U_B}{U_A}\right)^{1-2m} \tag{4.16}$$

with $0 \leq m \leq 0.2$ depending on the ion energy. In eq.(4.16), the dependence on mass differences is rather small compared to the effect of surface binding energy differences. Assuming the linear cascade except the top monolayer and unchanged bulk composition during sputtering, Kelly [23,24] arrived at the expression as

$$\frac{Y_A^c}{Y_B^c} = \frac{C_A^b + \Lambda_{AB} C_B^b (1 + C_B^s)\Delta H_B + (1 - C_B^s)\Delta H_A}{C_B^b + \Lambda_{AB} C_A^b (1 + C_A^s)\Delta H_A + (1 - C_A^s)\Delta H_B} \tag{4.17}$$

predicting enrichment of the component with the higher surface binding energy, where $\Lambda_{AB} = 4M_A M_B/(M_A + M_B)^2$ and $\Delta H_{A,B}$ is the heat of atomization of A, B respectively. Sigmund [1] also derived an equation in spike regime for high energy($E \geq 50$ keV) heavy ions such as

$$\frac{Y_A^c}{Y_B^c} = \left(\frac{M_B}{M_A}\right)^{1/2} \exp\left(\frac{U_B - U_A}{kT}\right) \tag{4.18}$$

with a spike temperature T dependent on ion and target parameters. Generally, for alloys and compounds with components of not too different masses the surface binding energies of the constituents should play the dominant role, while enrichment in the heavier components is found mostly for systems with quite different constituent masses.

As a consequence of preferential sputtering the composition profile is expected to change near the target surface, usually in one or two monolayers. However, experimental results have been showing that compositional changes occur to much deeper depths, typically comparable to the range of the incident ions. This layer of changed composition is often called the altered layer. At high temperature the altered layer thickness could be orders of magnitude larger than the ion range. Changes under ion bombardment over such depth range must be caused, in addition to preferential sputtering, by transport processes [25,26] such as

- recoil implantation and cascade mixing
- thermal and radiation enhanced diffusion
- surface segregation
- radiation induced segregation

, all of which make the sputtering of multicomponent material more complicated phenomena and difficult to analyze the experimental results. These transport mechanisms will be discussed further in the following sections.

4.2 Collisional mixing

When an ion slows down in the solid, it transfers energy and momentum to the target lattice eventually developing a collision cascade in which the target atoms are displaced from their lattice sites and come to rest at an appreciable distance from their original positions. As discussed in the previous section, sputtering occurs when the cascade intersects the surface resulting in the removal of the target atoms. Similarly, the cascade inside the material contributes to rearrangement or mixing of the constituent atoms in the multicomponent target, which is often called collisional mixing. The collisional mixing can be divided into two intuitively different mechanisms, i.e. recoil implantation and cascade mixing. Recoil implantation is referred to the process in which direct collisions between incident ion and target atoms cause the relocation of the target atoms. This mechanism contributes to the long-range mixing of the target material. On the other hand, cascade mixing is defined as the mixing process resulted from the collisions between the target atoms and recoils in the cascade, which is much more efficient to overall mixing. This mechanism is also called as short-range mixing because the energy involved in the process is rather lower than in the recoil implantation. The collisional mixing has been treated theoretically by many authors either with analytical approaches [27,28,29,17,30,31,32,33,35,36,37,38] or via developments of Monte Carlo programs [39,40].

Based on the linear collision cascade theory applied on the system of dilute impurities in homogeneous matrices, Sigmund and Gras-Marti [31,32,33]

evaluated the shift and spreading due to the collisional mixing. If we denote $\delta\Phi d\sigma(x,z)$ as the probability that a single impurity atom located at x will be relocated at a depth $(x+z, dz)$ after a differential ion fluence $\delta\Phi$, then the impurity will on the average be found at a depth

$$< x+z >= x + \delta\Phi \int z d\sigma(x,z) \tag{4.19}$$

, where $d\sigma(x,z)$ is called the differential relocation cross section. For multiple recoil implantation, using the power law scattering cross section as

$$d\sigma_{ij}(E,T) = C_{ij} E^{-m} T^{-1-m} dT \tag{4.20}$$

and with energy-projected range relation such as

$$R_p(T) = AT^{\alpha} \qquad , \qquad 0 \leq \alpha \leq 2 \tag{4.21}$$

, then the mean relocation of the impurity atom can be expressed as

$$< z >= (\alpha + \frac{1}{2} - m)^{-1} B(x) z_m(x) \Phi \tag{4.22}$$

with

$$\begin{aligned} B(x) &= C_{01} \Lambda_{01}^{-m} E^{-2m}(x) \\ z_m(x) &= R_p(\Lambda_{01} E(x)) \end{aligned} \tag{4.23}$$

, where Λ_{01} is the energy transfer factor from ion to the impurity atom and $E(x)$ is the well-defined degraded ion energy at depth x, which is given by

$$E(x) = E_0 (1 - \frac{x}{R_o})^{1/2m} \tag{4.24}$$

, where E_0 is the incident ion energy and R_o is the path length of the ion in the target material. According to eq.(4.22) Sigmund and Gras-Marti concluded that recoil implantation is a mechanism which favors relocation of lighter species in a multicomponent target. Also, considering the relocation of matrix atoms followed by relaxation, the direction of the net shift was predicted, for a light impurity in a heavy matrix to be shifted toward greater depth and it is toward the surface in the case of heavy impurity in a light matrix.

Recoil implantation is a rather rare event leading to relatively large relocation. Indeed, the cascade mixing initiated by recoiled matrix atoms is a much more efficient mixing process because there may be hundreds or thousands of matrix recoils that potentially can dislocate an impurity. For the cascade mixing, the mean spread will be given by

$$\Omega^2 = \Phi \int z^2 d\sigma(x,z) \tag{4.25}$$

, resulting in the HWHM(half width at half maximum) as

$$\Delta x_{1/2} = \frac{\pi}{4N} \Gamma A \xi_{21} \Phi F_D(x) \tag{4.26}$$

for the high energy isotropic cascade and

$$\Delta x_{1/2} = \frac{\Gamma}{3(1-2\alpha)N} \frac{R_c^2}{E_c} \xi_{21} \Phi F_D(x) \tag{4.27}$$

for the low energy cascade, which are both proportional to the ion fluence Φ and energy deposition $F_D(x)$, where N is the target atomic density, Γ is a dimensionless parameter somewhat less than unity, $\xi_{21} = C_{21} \Lambda_{21}^{1-m} / C_{22}$, and the range R_c is related to the threshold energy E_c by eq.(4.21). Sigmund and Gras-Marti applied the expressions to the system of 300 keV Xe^+ incident on a

Si target with an embedded Pt marker layer. Fig. 4.3 [33] shows the estimated broadening and shift of an initially narrow Pt layer as a function of ion fluence. One may first recognize that the matrix relocation with relaxation mechanism gives the most pronounced spread and shift. However, in later experiment [34] this conclusion was asserted to be disproven due to the opposite direction of impurity shift. In the figure, one also sees that multiple recoil implantation gives rise to a significant r.m.s. spread, but small half-width.

Haff and Switkowski [27] proposed a simple model describing the process by analogy with diffusion in a gas. However, the parameters on the model are not easily accessible in theory or experiment. Andersen [29] has proposed a model for the cascade mixing based on a rather simple argument to suggest guidelines for selection of projectile species and energies in sputter-profiling techniques to minimize such mixing effect. Andersen [29] gave the expression for the attainable depth resolution on the surface as

$$\Delta_{FWHM} = 2R \times \left(\frac{U}{4E_d} \frac{E}{S_n(E)} \frac{1}{0.42\alpha} \right)^{\frac{1}{2}} \tag{4.28}$$

, where R is the range of recoil atom with energy E_d on the order of 10 Å and $S_n(E)$ is the nuclear stopping cross section of the ion in unit of eVÅ^2. Hofer and Littmark [17,30] have solved the transport equations for elastic atomic collision to treat the cascade mixing. The accumulation of implanted projectiles and compensation of density change by lattice relaxation has been accounted for in the analysis. Matteson et al. [35] have treated the mixing problem based on a theory of random flight , predicting that the mixing is analogous to thermal diffusion with an effective diffusion coefficient, which is proportional to

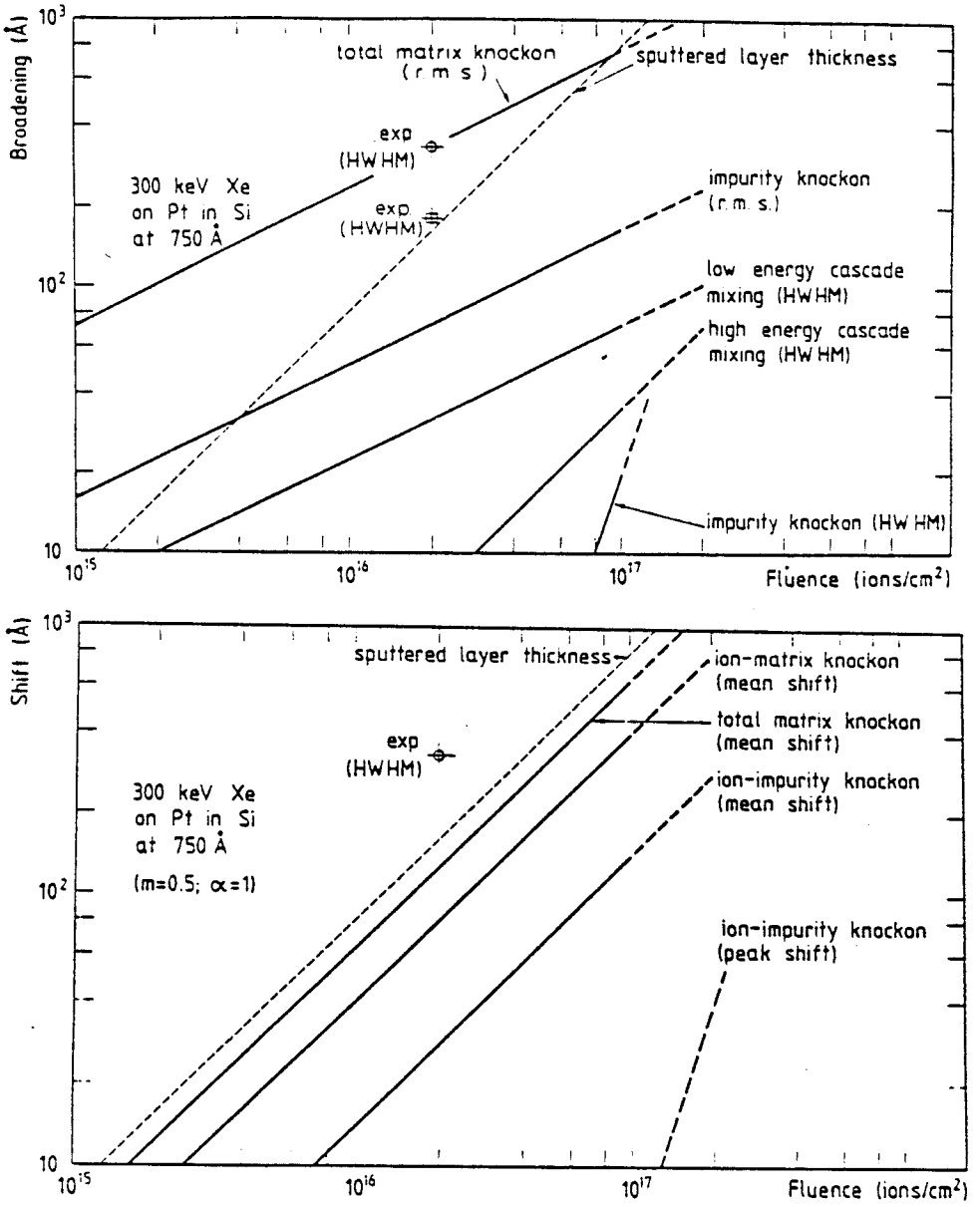

Figure 4.3: Calculated broadening and shift of a thin Pt marker in Si at 750 Å by 300 keV Xe bombardment [33]

the ion flux and energy deposition density. Collins et al. [36] have solved the problem with a diffusion approximation and using the collective current concept, which showed a good agreement with the results from transport approach [17,30,33]. Recently, Johannessen and Sigmund [38] showed that it is important to use the appropriate scattering cross section for the evaluation of the magnitude and direction of both the shift and broadening due to ion beam mixing.

Due to the limitations of various approximations imposed on the analytical modelling of the collisional mixing, a completely different solution method of the problem has been adopted by many authors, which is a development of a Monte Carlo program that can simulate the collisional mixing processes through a binary collision approximation [39,40].

4.3 Diffusional processes

4.3.1 Radiation enhanced diffusion

During ion bombardment many lattice atoms are displaced creating vacancies and interstitials, the concentrations of which often exceed the equilibrium thermal values in several orders. This increased concentration of point defects drastically enhances the diffusional processes in the target, which is called radiation enhanced diffusion [41,42]. In general, the diffusion coefficient is expressed as the summation of various contributing mechanisms, i.e.

$$D = f_v D_v C_v + f_i D_i C_i + f_{2v} D_{2v} C_{2v} + \cdots \tag{4.29}$$

, where f's, D's, and C's are the correlation factors, partial diffusivities, and concentrations for corresponding mechanisms(vacancy, interstitial, and divacancy mechanisms). Usually, the binding energies of divacancies and higher order aggregations are not well known, so it is common to consider only the contributions of single vacancies and interstitials to the diffusion coefficient. The radiation enhanced diffusion coefficient takes on one of three forms depending on the temperature ranges [43,44]. At high temperatures defect mobilities are so high that the radiation induced defects are lost quickly and the thermal equilibrium vacancy concentration is large compared to the radiation produced point defect concentration. Hence, the diffusion coefficient D takes the thermal value and the activation energy is equal to $E_v^f + E_v^m$, where E_v^f is the vacancy formation energy and E_v^m is the vacancy migration energy. In the intermediate temperature range, most of the vacancies and interstitials will be lost to fixed sinks, which leads to

$$D \simeq K\frac{k_i^2 + k_v^2}{k_i^2 k_v^2} \simeq \frac{2K}{k_i^2} \tag{4.30}$$

, where K is the defect production rate, k_i and k_v are the fixed sink strength for vacancies and interstitials respectively. The diffusion coefficient only depends on the damage rate and nearly independent of temperature(varying only as the fixed sink density such as dislocations). At lower temperature, the radiation produced vacancy concentration becomes high enough that recombination with interstitials begins to dominate, which gives

$$D \simeq \sqrt{\frac{K D_v a^2}{4\pi}} \tag{4.31}$$

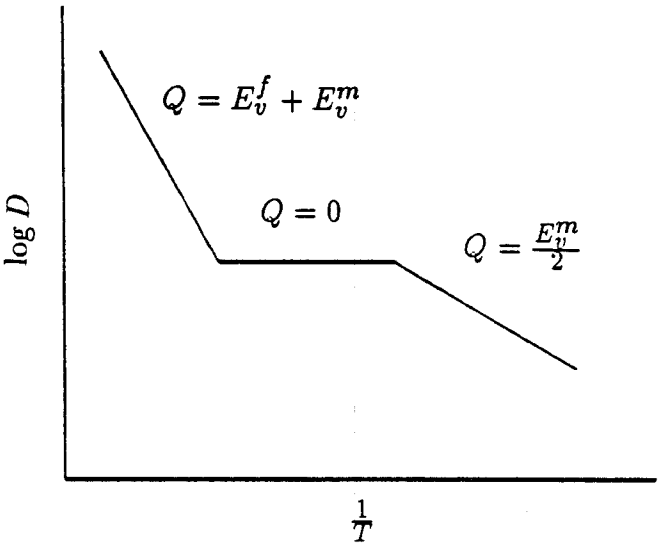

Figure 4.4: Temperature dependence of radiation enhanced diffusion

, where a is the lattice constant and D has an activation energy of $0.5E_v^m$. These three regimes are shown schematically in Fig. 4.4.

4.3.2 Radiation induced segregation

Under irradiation there are net fluxes of vacancies and interstitials to the various sinks such as dislocations, voids, grain boundaries, and free surfaces. If the composition of the defect flux is different from that of the target, there will be a segregation of alloying elements to and away from sinks. This radiation induced segregation caused by a coupling between defect and atomic fluxes is a commonly observed phenomenon, which may lead to a less-desirable redistribution of the alloying elements. Precipitates may form in locally enriched regions even though the precipitated phase is unstable at the average composition. Alternatively, precipitates which are stable may dissolve in de-

pleted regions. In addition, a local alteration in surface composition may give significant changes in the rates of void nucleation and growth.

Since Anthony [45] proposed the possibility of radiation induced segregation, there has been extensive theoretical work to model the mechanisms. However, due to the complexity of the phenomenon no complete physical model exists. Three kinetic models have been developed based on (1) size factor, (2) defect-solute binding for dilute alloys, (3) inverse Kirkendall effect for concentrated alloys [46].

The size factor model can be used to describe the segregation of undersized solute atoms which tend to preferentially exist as interstitials. Self-interstitials in BCC and FCC metals are believed to exist in a 'dumbbell' configuration, where two atoms share a single lattice site [47]. The strain energy of this configuration can be lowered by incorporating an undersized solute atom into the dumbbell for one of the solvent atoms. The small atom would tend to remain part of the dumbbell, which would migrate by interchanging solvent atoms. Thus, undersized solute atoms will be segregated to point defect sinks [48].

When the alloy is dilute enough that a point defect will usually interact with no more than one solute atom at a time, the solute-defect complexes may play an important role in segregation mechanism. Anthony [45] first proposed that a solute could be dragged toward a sink along with a point defect if there is a sufficient vacancy-solute binding. Johnson and Lam [49,50] and Wiedersich et al. [51] have developed a model applicable to dilute alloys, in which the various complexes are continually forming and dissociating, and the various mobile defects diffuse through the concentration gradients. In Johnson-Lam

model vacancies, interstitials, solute atoms, two kinds of interstitial-solute complexes, and vacancy-solute complexes are considered, which gives a set of six coupled partial differential equations for a binary alloy. When these equations were solved numerically, significant solute segregation was found at the surface in the temperature range $0.2T_m \sim 0.6T_m$ depending on the defect production rate. Furthermore, reduction of the displacement rate were found to increase the amount of solute segregation and shift the segregation temperature downwards. The Johnson-Lam model was modified subsequently to allow spatially varying defect production rates, predicting that solute atoms segregate to the surface and in the region beyond the damage peak of ion-irradiated metals [52,53,54].

In concentrated alloys, a vacancy or interstitial will be generally surrounded by several solute atoms, so the concept of binding between defect and solute atoms may reasonably ignored. Manning [55,56], Marwick [57], and Wiedersich et al. [58] have modeled solute segregation in concentrated alloys using the so-called 'inverse Kirkendall effect'. In the Kirkendall effect, unequal component diffusion coefficients in an alloy having a concentration gradient give rise to a vacancy flux resulting in destruction and creation of lattice planes. In the inverse Kirkendall effect, a radiation induced vacancy flux causes a flux of atoms and produces segregation of the alloy components.

The segregation model proposed by Marwick [57] for concentrated binary alloys considers only the vacancy contribution to the inverse Kirkendall effect, which is limited to alloys without a strong solute coupling to interstitial fluxes. This model predicts that the faster diffusing species will segregate away from

the sink climbing up the vacancy gradient. Wiedersich et al. [58] extended the Marwick's model to account for the radiation induced interstitial contribution to the inverse Kirkendall effect. For an alloy with n components, the diffusion equation can be written using the partial fluxes as

$$\begin{aligned} \frac{\partial C_v}{\partial t} &= K_o - L_{vd} - L_r - \nabla \cdot (\Omega \vec{J}_v) \\ \frac{\partial C_i}{\partial t} &= K_o - L_{id} - L_r - \nabla \cdot (\Omega \vec{J}_i) \\ \frac{\partial C_j}{\partial t} &= -\nabla \cdot (\Omega \vec{J}_j) \qquad , \qquad j = 1, \cdots, n \end{aligned} \tag{4.32}$$

, where v, i, and j denote vacancy, interstitial, and jth element in n-component target respectively, C's are concentrations, K_o is the defect production rate, L_{vd} and L_{id} are vacancy and interstitial loss rate to dislocations, L_r is v-i recombination loss rate, and Ω is the atomic volume. Furthermore, net vacancy, interstitial, and atomic flux $\vec{J}_v$, $\vec{J}_i$, and $\vec{J}_j$ are given by

$$\begin{aligned} \vec{J}_v &= \sum_j \vec{J}_{vj} \\ \vec{J}_i &= \sum_j \vec{J}_{ij} \\ \vec{J}_j &= \vec{J}_{ij} - \vec{J}_{vj} \end{aligned} \tag{4.33}$$

, where $\vec{J}_{vj}$ and $\vec{J}_{ij}$ are vacancy and interstitial fluxes via atom j, which are expressed as

$$\begin{aligned} \Omega \vec{J}_{vj} &= d_{vj}(C_v \nabla C_j - C_j \nabla C_v) \\ \Omega \vec{J}_{ij} &= -d_{ij}(C_i \nabla C_j + C_j \nabla C_i) \end{aligned} \tag{4.34}$$

, where the partial diffusivities d_{vj} and d_{ij} are given by

$$d_{vj} = \frac{\lambda_j^2}{6} Z_j \nu_{vj} \exp(-\frac{E_{vj}^m}{kT}) \tag{4.35}$$

$$d_{ij} = \frac{\lambda_j^2}{6} Z_j \nu_{ij} \exp(-\frac{E_{ij}^m}{kT})$$

, where λ_j and Z_j are the jump distance and coordination number of jth element and ν_{vj}, ν_{ij}, E_{vj}^m, and E_{ij}^m are the vibrational frequencies and energy of motion for the vacancy and interstitial of the jth alloy component. Moreover, the loss terms in eq.(4.32) can be expressed as

$$\begin{aligned} L_{vd} &= \frac{2\pi\rho_d}{\ln(R_d/R_o)}(C_v - C_v^{eq}) \sum_j d_{vj} C_j \\ L_{id} &= \frac{2\pi\rho_d}{\ln(R_d/R_o)} C_i \sum_j d_{ij} C_j \\ L_r &= 4\pi C_v C_i \sum_j \left(\frac{6(d_{ij} + d_{vj})}{\lambda_j^2 Z_j} C_j \right) \end{aligned} \tag{4.36}$$

, where ρ_d is the dislocation density, R_d is the spacing between dislocations calculated from $\pi R_d^2 = 1/\rho d$, R_o is the dislocation core radius, and C_v^{eq} is the equilibrium vacancy concentration. Wiedersich et al. [58] solved the equation for a binary alloy system, predicting the similar segregation behavior as Johnson-Lam model. This model is not applicable to dilute alloys in which segregation via vacancy-solute complexes is known to be important. Segregation by interstitial-solute complexes can be taken into account by modifying the energy of motion of A and B interstitials.

4.3.3 Surface(Gibbisian) segregation

In thermal equilibrium, the surface composition of an alloy is generally different from the bulk [59,60]. According to the pair-bond model, if an element has a lower surface binding energy than the other component, then the

free energy of system can be lowered by exchanging the tightly bound component on the surface with the loosely bound one from the interior [61]. The difference in size may also give surface segregation of the larger component in a concentrated alloys [62,63]. Because diffusion of atomic species is involved in the phenomenon, the thermodynamic equilibrium can be reached only at high temperatures. However, the high concentration of point defects produced during ion bombardment greatly enhances the atomic mobility to allow the equilibrium configuration even at low temperatures. In general, the surface segregation in binary alloys [59,61] can be expressed with

$$\begin{aligned} \frac{C_A^s}{C_B^s} &= \frac{C_A^b}{C_B^b}\exp(-\frac{\Delta G_s}{kT}) \\ &= \frac{C_A^b}{C_B^b}\exp(-\frac{\Delta H_s}{kT})\exp(\frac{\Delta S_s}{k}) \end{aligned} \tag{4.37}$$

, where C_A^s and C_B^s are the surface concentration of A and B atoms respectively, C_A^b andC_B^b are the corresponding bulk concentrations, ΔG_s, ΔH_s, and ΔS_s are the free energy, enthalpy, and entropy of segregation.

References

[1] P. Sigmund, "Sputtering by Particle Bombardment I"(R. Beherisch, ed.), p. 9 (1981).

[2] J. Bohdansky, J. Roth, and H. L. Bay, J. Appl. Phys. **51**, 2861 (1980).

[3] J. Roth, "Symposium on Sputtering"(P. Varga, G. Betz, and F. P. Viehböck, eds.), p. 773 (1980) Inst. Allgem, Physik, Vienna.

[4] U. Littmark and S. Fedder, Nucl. Instrum. Meth. **194**, 611 (1982).

[5] P. Sigmund, Phys. Rev. **184**, 383 (1969).

[6] H. H. Andersen and H. L. Bay, J. Appl. Phys. **45**, 953 (1974).

[7] A. R. Oliva-Florio et al., Rad. Effects Lett. **50**, 3 (1979).

[8] D. A. Thompson, "Symposium on Sputtering"(P. Varga, G. Betz, and F. P. Viehböck, eds.), p. 62 (1980) Inst. Allgem, Physik, Vienna.

[9] D. A. Thompson, Rad. Effects **56**, 104 (1981).

[10] P. Sigmund, Phys. Rev. **187**, 768 (1969).

[11] H. H. Andersen and H. L. Bay, J. Appl. Phys. **46**, 2416 (1975).

[12] G. K. Wehner and D. Rosenberg, J. Appl. Phys. **31**, 177 (1960).

[13] W. O. Hofer, "Sputtering by Particle Bombardment III"(R. Behrisch, ed.) (1983).

[14] B. Perović.4 and B. Cobić, "Proc. 5th Int. Conf. on Ion Phenomena in Gases"(M. Maecker ed.) p. 1165 (1961).

[15] P. Sigmund, M. T. Matties, and D. L. Phillips, Rad. Effect **11**, 34 (1971).

[16] N. Andersen and P. Sigmund, K. Dan. Vidensk. Selsk. Mat. Fys. Medd. **39**, No. 3 (1974).

[17] W. O. Hofer and U. Littmark, Phys. Lett. **71A**, 457 (1979).

[18] U. Littmark and G. Maderlechner, "Physics of Ionized Gases"(ed. by B. Navinsek et al.) (1976).

[19] U. Littmark and P. Sigmund, J. Phys. D. **8**, 241 (1975).

[20] H. L. Bay, J. Roth, and J. Bohdansky, J. Appl. Phys. **48**, 4722 (1977).

[21] J. Roth, J. Bohdansky, and W. Ottenberger, "Data on Low Energy Light Ion Sputtering", IPP 9/26 (1979).

[22] N. Matsunami et al., "Energy Dependence of Sputtering Yields of Monatomic Solids", IPPJ-AM-14 (1980).

[23] R. Kelly, Nucl. Instrum. Meth. **149**, 553 (1978).

[24] R. Kelly, Surf. Sci. **100**, 85 (1980).

[25] G. Betz and G. K. Wehner, "Sputtering by Particle Bombardment II"(R. Beherisch, ed.), p. 11 (1981).

[26] H. H. Andersen, "Ion Implantation and Beam Processing"(J. S. Williams and J. M. Poate, eds.) p. 127 (1984).

[27] P. K. Haff and Z. E. Switkowski, J. Appl. Phys. **48**, 3383 (1977).

[28] R. Kelly and J. B. Sanders, Surf. Sci. **57**, 143 (1976).

[29] H. H. Andersen, J. Appl. Phys. **18**, 131 (1979).

[30] U. Littmark and W. O. Hofer, Nucl. Instr. and Meth. **168**, 329 (1980).

[31] P. Sigmund and A. Gras-Marti, Nucl. Instr. and Meth. **168**, 389 (1980).

[32] A. Gras-Marti and P. Sigmund, Nucl. Instr. and Meth. **180**, 211 (1981).

[33] P. Sigmund and A. Gras-Marti, Nucl. Instr. and Meth. **182/183**, 25 (1981).

[34] B. M. Paine, J. Appl. Phys. **53**, 6828 (1982).

[35] S. Matteson, B. M. Paine, and M. A. Nicolet, Nucl. Instr. and Meth. **182/183**, 53 (1981).

[36] R. Collins et al., Nucl. Instr. and Meth. **209/210**, 147 (1983).

[37] G. Carter, R. Collins, and D. A. Thompson, Rad. Effect **54**, 235 (1981).

[38] K. Johannessen and P. Sigmund, Nucl. Instr. and Meth. **B19/20**, 85 (1987).

[39] M. L. Roush et al. Nucl. Instr. and Meth. **194**, 611 (1982).

[40] W. Möller and W. Eckstein, Nucl. Instr. and Meth. **B7/8**, 645 (1985).

[41] R. Sizmann, J. Nucl. Mater. **69 & 70**, 386 (1978).

[42] Y. Adda, M. Beyeler, and G. Brebec, Thin Solid Films **25**, 107 (1975).

[43] G. J. Dienes and A. C. Damask, J. Appl. Phys. **29**, 1713 (1958).

[44] K. C. Russell, Progress in Materials Science, Vol bf 28, 229 (1984).

[45] T. R. Anthony, "Radiation Induced Voids in Metals", p. 630 (1971).

[46] H. Wiedersich, "Phase Stability During Irradiation", p. 23 (1981).

[47] H. G. Haubold and D. Martinson, J. Nucl. Mater. **69/70**, 644 (1978).

[48] P. R. Okamoto and H. Wiedersich, J. Nucl. Mater. **53**, 336 (1974).

[49] R. A. Johnson and N. Q. Lam, Phys. Rev. B. **13**, 4364 (1976).

[50] R. A. Johnson and N. Q. Lam, Phys. Rev. B. **15**, 1794 (1977).

[51] H. Wiedersich, P. R. Okamoto, and N. Q. Lam, "Radiation Effects in Breeder Reactor Structural Materials"(eds. M. L. Bleiberg and J. W. Bennett) TMS-AIME, New York, p. 801 (1977).

[52] N. Q. Lam, P. R. Okamoto, and R. A. Johnson, J. Nucl. Mater. **78**, 408 (1978).

[53] N. Q. Lam et al., Met. Trans. **9A**, 1707 (1978).

[54] P. R. Okamoto, L. E. Rehn, and R. S. Averback, J. Nucl. Mater. **108/109**, 319 (1982).

[55] J. R. Manning, Bull. Am. Phys. Soc. **23**, 287 (1978).

[56] J. R. Manning, "Phase Stability During Irradiation", p. 3 (1981).

[57] A. D. Marwick, R. C. Pillar, and M. E. Horton, "Radiation Induced Segregation in Fe-Ni-Cr Alloys", Corsica Conf. (1979).

[58] H. Wiedersich, P. R. Okamoto, and N. Q. Lam, J. Nucl. Mater. **83**, 98 (1979).

[59] H. H. Brongersma, M. J. Sparnaay, and T. M. Buck, Surf. Sci. **71**, 657 (1978).

[60] A. Crucq et al., Surf. Sci. **80**, 78 (1979).

[61] R. Kelly, in "Proc. Symp. on Sputtering" (eds. P. Varga, G. Betz, and F. P. Viehböck), Perchtoldsdorf/Vienna, p. 390 (1980).

[62] W. M. H. Sachtler and R. A. von Santen, Appl. Surf. Sci. **3**, 121 (1979).

[63] F. F. Abraham and C. R. Brundle, J. Vac. Technol. Sci. **18**, 506 (1981).

Chapter 5.

Computer simulation of ion beam mixing

5.1 Computer simulation methods

The difficulties of analytic methods for the solution of ion transport problem in solids increase as the basic assumptions are removed to solve the transport equation describing more complicated situations such as multilayered targets. The high computational speed and large memory capacity of modern digital computers have enabled us to adopt a totally different approach and attempt to simulate the particle transport process directly without referring to the transport equation. These computer simulation methods being used for the study of radiation effects can be categorized in two groups, i.e. molecular dynamics simulation and Monte Carlo method.

5.1.1 Molecular dynamics simulation

In this method [1,2,3] collective particle transport is simulated using deterministic ways in which the microscopic equations of motion characterizing the dynamics of the many particle system are solved directly.

Suppose that the system consists of N particles. With the given initial position and velocity vector for each particle, the dynamical history of the system is generated by numerically integrating the $3N$ simultaneous equations of motion for the coordinate components of the N atoms in the system. This

method is very useful in demonstrating the directional effects such as focusing and channeling. However, it is presently limited to a few keV in ion energy due to the present limit of the computational speed in today's computers.

5.1.2 Monte Carlo method

Since particle collisions are usually described statistically, particle transport takes on a highly stochastic nature, that of a random walk. The statistical method for simulating transport process, commonly called Monte Carlo method [4,5,6,7,8] estimates the expected characteristics of the system as statistical averages over a large number of case histories of particles.

Definitions

Consider a random variable x defined on the interval $a \leq x \leq b$. Since we cannot predict with certainty what value this variable will assume, we introduce the probability distribution or probability density function $P(x)$ governing the random variable, which is defined such that $P(x)dx$ is the probability that x assumes a value between x and $x + dx$, with the normalizing condition as

$$\int_a^b P(x)dx = 1 \tag{5.1}$$

For example, the random number between 0 and 1 has the probability distribution function of

$$P(R) = 1 \qquad \text{for } 0 \leq R \leq 1 \tag{5.2}$$

that is, the probability distribution is uniform on the interval $[0, 1]$. The other example of interest is the probability of a nuclear collision in a distance dx about x, which is given by

$$P(x)dx = \Sigma_s \exp(-\Sigma_s x)dx \tag{5.3}$$

, where Σ_s is the macroscopic scattering cross section.

The probability that a random variable assumes a value less than x is given by the cumulative distribution function $C(x)$ as

$$C(x) = \int_a^x P(x')dx' \tag{5.4}$$

From this definition, $C(x)$ is a monotonically increasing function of x and is restricted to the interval $0 \leq C(x) \leq 1$. In particular, $C(a) = 0$ and $C(b) = 1$. The probability distribution function $P(x)$ and cumulative distribution function $C(x)$ are illustrated in Fig. 5.1.

Sampling technique

The selection of the value of a random variable distributed according to a given probability distribution plays a central role in Monte Carlo calculations. Let $P_{RN}(R)$ be the random number distribution function and $P(x)$ be the distribution function of a random variable x. The $P_{RN}(R)$ and $P(x)$ can be related as

$$P_{RN}(R)dR = P(x)dx \tag{5.5}$$

Integrating both sides and noting that $P_{RN}(R) = 1$, we get

$$R = \int_a^x P(x')dx' = C(x) \tag{5.6}$$

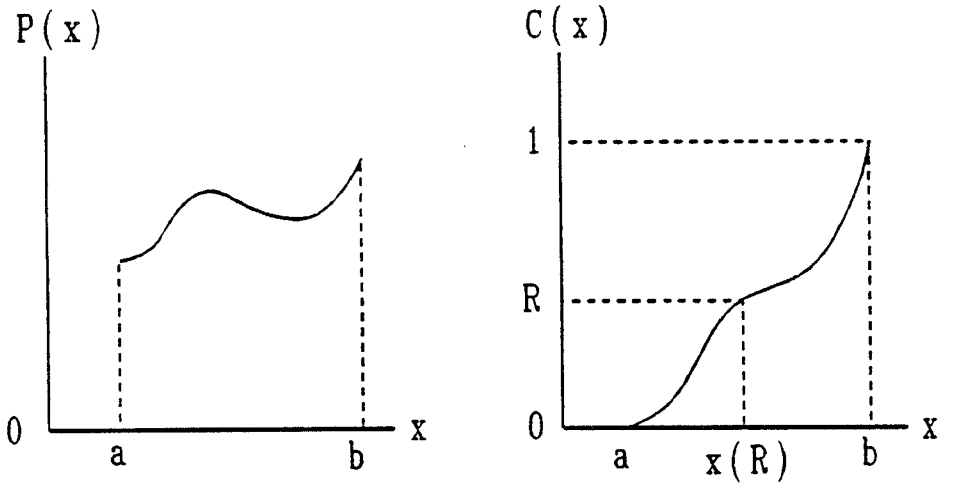

Figure 5.1: Probability distribution function $P(x)$ and cumulative distribution function $C(x)$

, or

$$x = C^{-1}(R) \tag{5.7}$$

, which gives the equation from which one can select x values from random numbers. This is also illustrated in Fig. 5.1.

If we consider again the previous example of path length for a nuclear collision, then from the probability distribution function we can get

$$\begin{aligned} C(x) &= \int_0^x P(x')dx' \\ &= 1 - \exp(-\Sigma_s x) \end{aligned} \tag{5.8}$$

If we denote a random number by R, then eq.(5.6) leads to

$$R = 1 - \exp(-\Sigma_s x) \tag{5.9}$$

, or

$$x = -\frac{1}{\Sigma_s} \ln(1 - R) \tag{5.10}$$

Since $1 - R$ is also distributed in the same manner as R on the interval $[0, 1]$, we obtain the well-known expression as

$$x = -\frac{1}{\Sigma_s} \ln R \tag{5.11}$$

, which shows how to determine the step length for a nuclear collision.

Accuracy of Monte Carlo method

The measurement of the accuracy of the Monte Carlo method can be expressed in terms of the standard deviation σ , which is defined as

$$\begin{aligned} \sigma &= \left(\frac{\sum_{i=1}^{N} (x_i - \bar{x})^2}{N} \right)^{1/2} \\ &= \left(\frac{1}{N} \sum_{i=1}^{N} x_i^2 - \bar{x}^2 \right)^{1/2} \end{aligned} \tag{5.12}$$

The accuracy increases as the number of simulated histories, however, in the manner of $N^{-\frac{1}{2}}$, which means that we must increase the sample size by a factor of 100 to reduce the error by a factor of 10. This slow convergence represents a major drawback of the Monte Carlo method.

Variance reduction technique

In an analogue Monte Carlo method, all particles which undergo a particular event contribute a score of 1 to the result of interest. However, the application of Monte Carlo methods to the direct simulation of transport

processes in which rare events are important is very inefficient because most computation time is spent on more probable particle histories that do not contribute significantly to the desired result. Such physical analogue calculations not only require enormous sample size to yield results of sufficient accuracy, but they can also push the problem beyond the capability of random number generators, possibly giving rise to correlated samples. Therefore, it is of great interest to reduce the error without necessarily increasing the sample size. In a non-analogue Monte Carlo simulation of particle transport, variance reduction methods are adopted to attempt to bias the original problem so that the regions which contribute most to the desired answer are sampled most frequently.

To illustrate the idea of importance sampling, let's consider a function $f(x)$ with a probability distribution function $p(x)$ defined on $[a, b]$. The mean value of $f(x)$ is given by

$$< f >= \int_a^b f(x)p(x)dx \tag{5.13}$$

In an attempt to reduce the error by reducing the variance given by

$$\sigma^2 =< f^2 > - < f >^2 \tag{5.14}$$

, let's sample x from a different probability distribution function $\tilde{p}(x)$ with a weight for each point x as

$$w(x) = \frac{p(x)}{\tilde{p}(x)} \tag{5.15}$$

and score the samples as $\tilde{f}(x) = f(x)w(x)$. In this way, we preserve the mean value, i.e.

$$< \tilde{f} > \; = \; \int_a^b \tilde{f}(x)\tilde{p}(x)dx \tag{5.16}$$

$$= \int_a^b f(x)p(x)dx =< f >$$

However, the variance will be different, that is

$$\begin{aligned} \tilde{\sigma}^2 &= < \tilde{f}^2 > - < \tilde{f} >^2 \\ &= \int_a^b \tilde{f}^2(x)\tilde{p}(x)dx - < f >^2 \\ &= \int_a^b f^2(x)p(x)\frac{p(x)}{\tilde{p}(x)}dx - < f >^2 \neq \sigma^2 \end{aligned} \tag{5.17}$$

Since $\tilde{\sigma}^2 > 0$, it is apparent that if we can choose $\tilde{p}(x)$ such that over an important region

$$\frac{p(x)}{\tilde{p}(x)} < 1 \tag{5.18}$$

, then we can reduce the variance. Actually, if we could choose $\tilde{p}(x)$ such as

$$\tilde{p}(x) = p(x)\frac{f(x)}{< f >} \tag{5.19}$$

, we find that $\tilde{\sigma}^2 = 0$. Of course, if we knew $< f >$, we would not need to sample for it. Instead, we can try to choose $\tilde{p}(x)$ such that

$$f(x)\frac{p(x)}{\tilde{p}(x)} \sim \text{constant} \tag{5.20}$$

To accomplish this, we may take more sample values in some region than the others.

The most frequently used and safe importance sampling method is the splitting and Russian roulette [8]. In splitting, we can artificially bias a Monte Carlo calculation to emphasize the particles moving toward more important region by replacing each particle with n equivalent particles, each with a new weight reduced by $\frac{1}{n}$. In Russian roulette procedure, we can randomly terminate particle histories moving toward less important region and increase the

weights of the surviving particles accordingly. In this way, the total weight of the system is conserved.

5.2 A dynamic Monte Carlo program TAMIX -Transport And MIXing from ion irradiation

5.2.1 Transport procedure

Assumptions

There are several assumptions on which TAMIX is based.

- The target is assumed to be amorphous, that is, the directional characteristics of the real lattice are neglected.
- A planar target geometry is considered, which imposes one dimensional variations of materials profile, even though the transport procedure is conducted in three dimensional space.
- A moving atom loses its energy via nuclear and electronic stopping processes, which are independent each other.
- Binary collision approximation is used for the nuclear scattering between a moving atom and a target atom. The simultaneous collision with more than one target atom is neglected.
- The scattering angle is calculated from the classical scattering integral given by eq.(2.36) and eq.(2.37).

- The mean free path assumption is used, that is the distance between successive collisions has the exponential distribution as in eq.(5.3).
- Between nuclear collisions, a moving atom loses its energy continuously through electronic stopping process, which however doesn't alter the direction of the moving atom.
- The history of moving atom is terminated if it gets out of the target surface or its energy goes down below a cutoff energy.

Scattering cross section calculation

To determine the path length traversed before next nuclear collision, the scattering cross section has to be calculated. From physical understanding of a nuclear collision, the scattering cross section will be given by

$$\sigma_t = N_t^{-\frac{2}{3}} = \pi p_{max,o}^2 \tag{5.21}$$

, where N_t is the total atomic density of the target and $p_{max,o}$ is the radius of the equivalent circular cell, which is shown in Fig. 5.2. Eq.(5.21) gives the upper limit of scattering cross section, which results in the average interatomic distance for a mean free path between collisions. However, at high energy most of the collisions give small deflections of the moving atom and consequently, small energy transfer to the target atoms, which does not contribute significantly to change the simulation results. Hence, to accelerate the calculation at high energy an adjusted maximum impact parameter p_{max} smaller than $p_{max,o}$ is used, which gives the larger mean free path or less nuclear col-

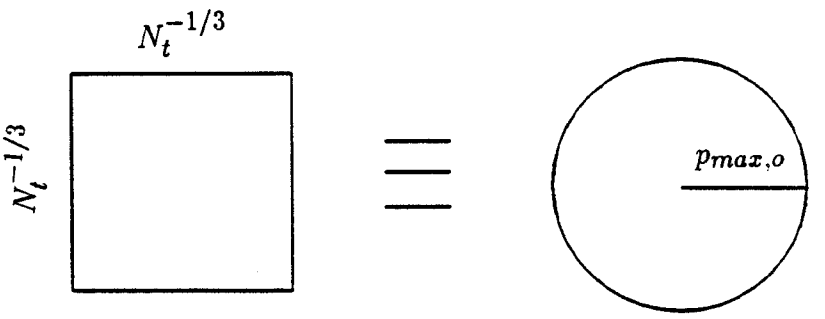

Figure 5.2: Equivalent target atomic cell

lisions ignoring the insignificant ones. Two criteria are used to determine the appropriate p_{max}, which are based upon deflection angle and energy transfer.

- $p_{max,a}$ is the impact parameter which gives the deflection angle of the moving atom $\theta_{min}(\sim 1°)$, by which the collisions with a smaller deflection angle are neglected.

- $p_{max,e}$ is the impact parameter at which the moving atom transfers the displacement energy E_d, resulting that the lower energy transfer collisions are neglected.

To be conservative, the larger value between $p_{max,a}$ and $p_{max,e}$ is used. Therefore, the final expression for p_{max} will be

$$p_{max} = \min(p_{max,o}, \max(p_{max,a}, p_{max,e})) \tag{5.22}$$

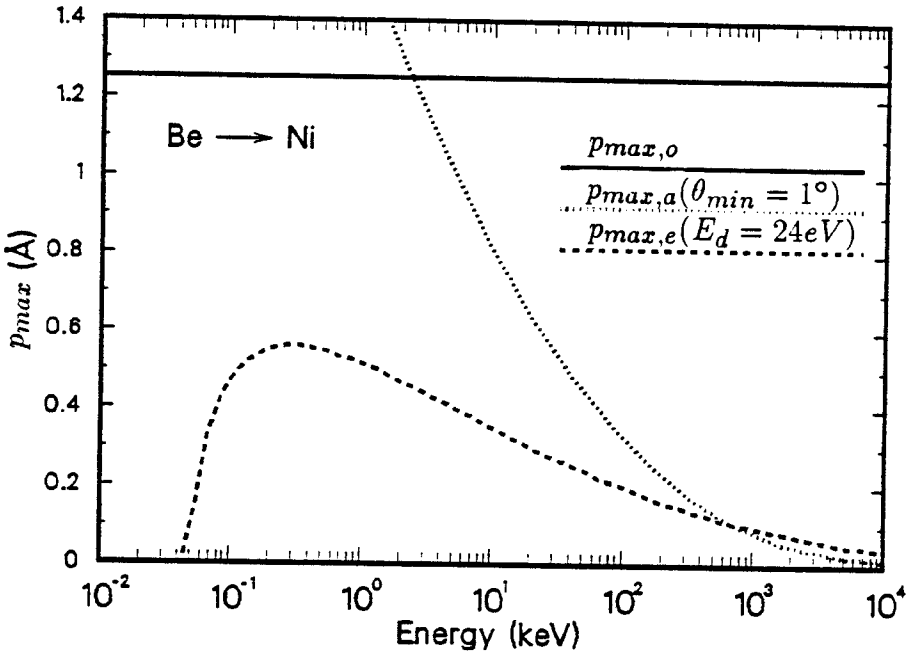

Figure 5.3: Various p_{max}'s for Be into Ni

, or equivalently

$$\sigma_t = \min(N_t^{-\frac{2}{3}}, \max(\pi p_{max,a}^2, \pi p_{max,e}^2)) \tag{5.23}$$

Fig. 5.3 shows an example of Be ion in Ni target. As seen in the figure, the angle criteria gives a monotonic increasing impact parameter as the ion energy is reduced. But, the energy criteria shows a maximum behavior, below which the impact parameter to transfer E_d decreases rapidly approaching a threshold energy $\frac{E_d}{\Lambda}$, where Λ is the energy transfer factor.

In a surface region, however, sputtering is an important process resulted from the near-surface collisions, which is dominated by low energy collisions. Hence, if the collision occurs within some distance from the surface, the most conservative way is used, i.e.

$$p_{max} = p_{max,o} \qquad \text{if} \qquad z \leq n_{sl} N_t^{-\frac{1}{3}} \tag{5.24}$$

, or

$$\sigma_t = N_t^{-\frac{2}{3}} \qquad \text{if} \qquad z \leq n_{sl} N_t^{-\frac{1}{3}} \tag{5.25}$$

, where z is the position of the moving atom from the surface and n_{sl} is the number of atomic layers considered as surface region (~ 8).

Step length determination

Before describing the way to determine the step length between collisions, let's examine the electronic stopping processes. The program TAMIX uses S_e developed by Ziegler et al. [9], which is described in section **2.2** along with the velocity proportional formula as in Lindhard's for low energy region [10]. Because the interactions with target electrons reduce the energy of the moving atom continuously, the effective S_e is also changing with energy during its motion. To take into account of this continuous energy loss, we can assume a linear dependence of $S_e(E)$ for a small interval of energy difference ΔE, that is

$$\begin{aligned} S_e(E) &= C_1 E + C_2 \\ S_e(E - \Delta E) &= C_1(E - \Delta E) + C_2 \end{aligned} \tag{5.26}$$

, which gives the expression for the slope C_1 as

$$C_1 = \frac{S_e(E) - S_e(E - \Delta E)}{\Delta E} \tag{5.27}$$

Furthermore, the step length l_e traversed during the energy loss ΔE is expressed as

$$l_e = \int_0^{l_e} dl = \int_E^{E-\Delta E} \frac{dE'}{dE'/dl} = -\int_E^{E-\Delta E} \frac{dE'}{N_t S e(E')} \tag{5.28}$$

$$= \frac{\Delta E}{N_t(S_e(E) - S_e(E - \Delta E))} \ln\left(\frac{S_e(E)}{S_e(E - \Delta E)}\right)$$

Hence, if ΔE is set as a fraction of the initial energy E such that

$$\Delta E = fE \quad , \quad f \sim 0.2 \tag{5.29}$$

, then

$$l_e = \frac{fE}{N_t(S_e(E) - S_e((1-f)E)} \ln\left(\frac{S_e(E)}{S_e((1-f)E)}\right) \tag{5.30}$$

In general, the target is composed of many layers with different materials and compositions, which are again divided into small sublayers. To determine the step length, three dimensionless distances are compared, which are given by

$$\begin{aligned} S_1 &= -\ln R \\ S_2 &= \frac{l_b}{\lambda} = \frac{l_b}{N_t \sigma_t} \\ S_3 &= \frac{l_e}{\lambda} = \frac{l_e}{N_t \sigma_t} \end{aligned} \tag{5.31}$$

, where R is a random number between 0 and 1, λ is the mean free path, σ_t is the total scattering cross section in the present layer calculated from eq.(5.23) and eq.(5.25), l_b is the distance from the present position to the next material boundary along the direction of motion and l_e is the distance associated with the fractional energy loss given by eq.(5.30). The first equation comes from the exponential distribution of the step lengths given by eq.(5.3) and the final step length S is determined from

$$S = \min(S_1, S_2, S_3) \tag{5.32}$$

If $S = S_1$, then it will make a collision at the new position. If not, it will move further in the present layer(if $S = S_3$) or begin to move in the next layer(if $S = S_2$) with a reduced energy and S_1 such that

$$\begin{aligned} E &\longrightarrow E - \Delta E \\ S_1 &\longrightarrow S_1 - S \end{aligned} \tag{5.33}$$

, where ΔE is calculated from

$$\Delta E = (1-f)E\left(\frac{1-\exp(-k\lambda S)}{1-\exp(-kl_e)}\right) \tag{5.34}$$

with k given by

$$k = N_t \frac{S_e(E) - S_e((1-f)E)}{fE} \tag{5.35}$$

In this way, the particle will proceed until S equals S_1, where will be the next collision point. Fig. 5.4 shows the situation for $S = S_3$.

Target atom selection

For a multicomponent solid, the target atom as a collision partner is selected using the discrete probability distribution function as

$$P_i = \frac{\sigma_i \chi_i}{\sum_{j=1}^{n} \sigma_j \chi_j} \quad , \quad i = 1, \cdots, n \tag{5.36}$$

, where n is the number of the atomic species, σ_i is the scattering cross section of ith element described previously, and χ_i is its atomic fraction. The cumulative distribution function will be

$$\begin{aligned} C_i &= \frac{\sum_{j=1}^{i} \sigma_j \chi_j}{\sum_{j=1}^{n} \sigma_j \chi_j} \equiv \frac{\sigma_c^i}{\sigma_c^n} \\ &= R \end{aligned} \tag{5.37}$$

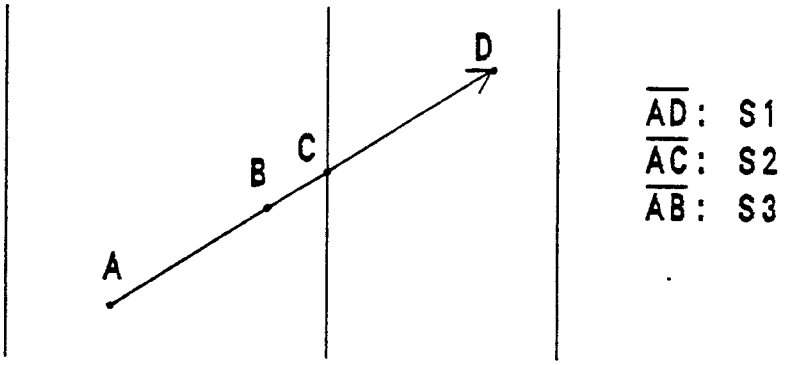

Figure 5.4: Illustration of step length selection

, where R is a random number between 0 and 1. Thus, the target atom for collision will be ith atomic species if

$$\frac{\sigma_c^{i-1}}{\sigma_c^n} \leq R \leq \frac{\sigma_c^i}{\sigma_c^n} \qquad , \qquad i = 1, \cdots, n \tag{5.38}$$

Impact parameter selection

After determining the target atom we have to choose the impact parameter to calculate the scattering angle. The impact parameter p for a nuclear collision is selected by sampling for a point from a uniform areal distribution of points inside a circle of radius p_{max}, which is given by eq.(5.22) and eq.(5.24). From Fig. 5.5 the probability distribution function can be written as

$$P(p)dp = \frac{2\pi p dp}{\pi p_{max}^2} = \frac{2pdp}{p_{max}^2} \tag{5.39}$$

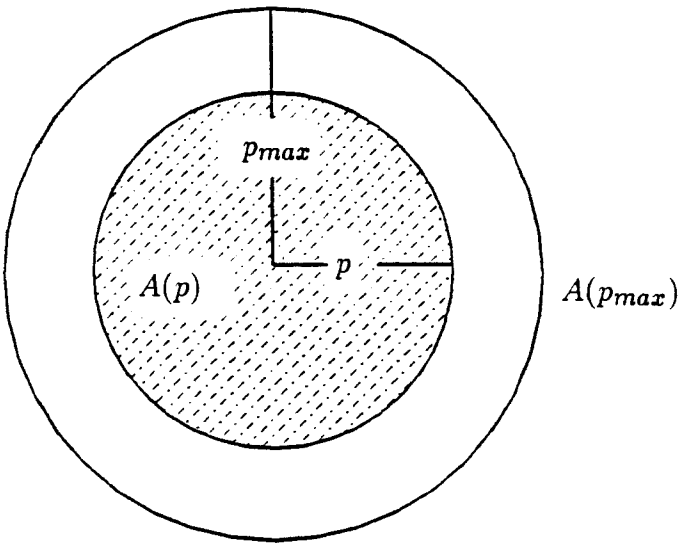

Figure 5.5: Illustration of impact parameter selection

, which gives the cumulative distribution function as

$$\begin{aligned} C(p) &= \frac{p^2}{p_{max}^2} \\ &= R \end{aligned} \tag{5.40}$$

, where R is a random number. Hence, the final expression for the impact parameter selection will be

$$p = p_{max}\sqrt{R} \tag{5.41}$$

Scattering angle calculation

The axial scattering angle in the center of mass system between two charged particles under the influence of a repulsive screened Coulomb po-

tential is given by eq.(2.36) and eq.(2.37), i.e.

$$\theta = \pi - 2b\int_0^{z_0} \frac{dz}{\sqrt{1-\frac{z}{\varepsilon}\Phi(\frac{1}{z})-b^2z^2}} \tag{5.42}$$

, where z_0 is the root of the equation:

$$1-\frac{z}{\varepsilon}\Phi(\frac{1}{z})-b^2z^2=0 \tag{5.43}$$

, where b is the reduced impact parameter (p/a), ε is the reduced energy, and Φ is the screening function. This equation cannot be solved analytically, so we have to use a numerical integration. However, one sees that the integrand has a singularity at $z = z_0$. To get around this problem [11], the integral (I) can be expressed as

$$\begin{aligned} I = I_1 + I_2 &= \int_0^{z_0} \frac{dz}{\sqrt{1-\frac{z}{\varepsilon}\Phi(\frac{1}{z_0})-b^2z^2}} \\ &+ \int_0^{z_0} \left(\frac{1}{\sqrt{1-\frac{z}{\varepsilon}\Phi(\frac{1}{z})-b^2z^2}} - \frac{1}{\sqrt{1-\frac{z}{\varepsilon}\Phi(\frac{1}{z_0})-b^2z^2}} \right) dz \end{aligned} \tag{5.44}$$

The first integral I_1 has an analytic solution as

$$I_1 = \frac{1}{b}\left\{\frac{\pi}{2} - \sin^{-1}\left(\frac{1-b^2z_0^2}{1+b^2z_0^2}\right)\right\} \tag{5.45}$$

and one can calculate I_2 using a numerical integration quadrature. The resulting expression is

$$\theta = 2\sin^{-1}\left(\frac{1-b^2z_0^2}{1+b^2z_0^2}\right) - 2bI_2 \tag{5.46}$$

In Fig. 5.6 , the scattering angle for the Universal potential is shown as a function of ϵ and b.

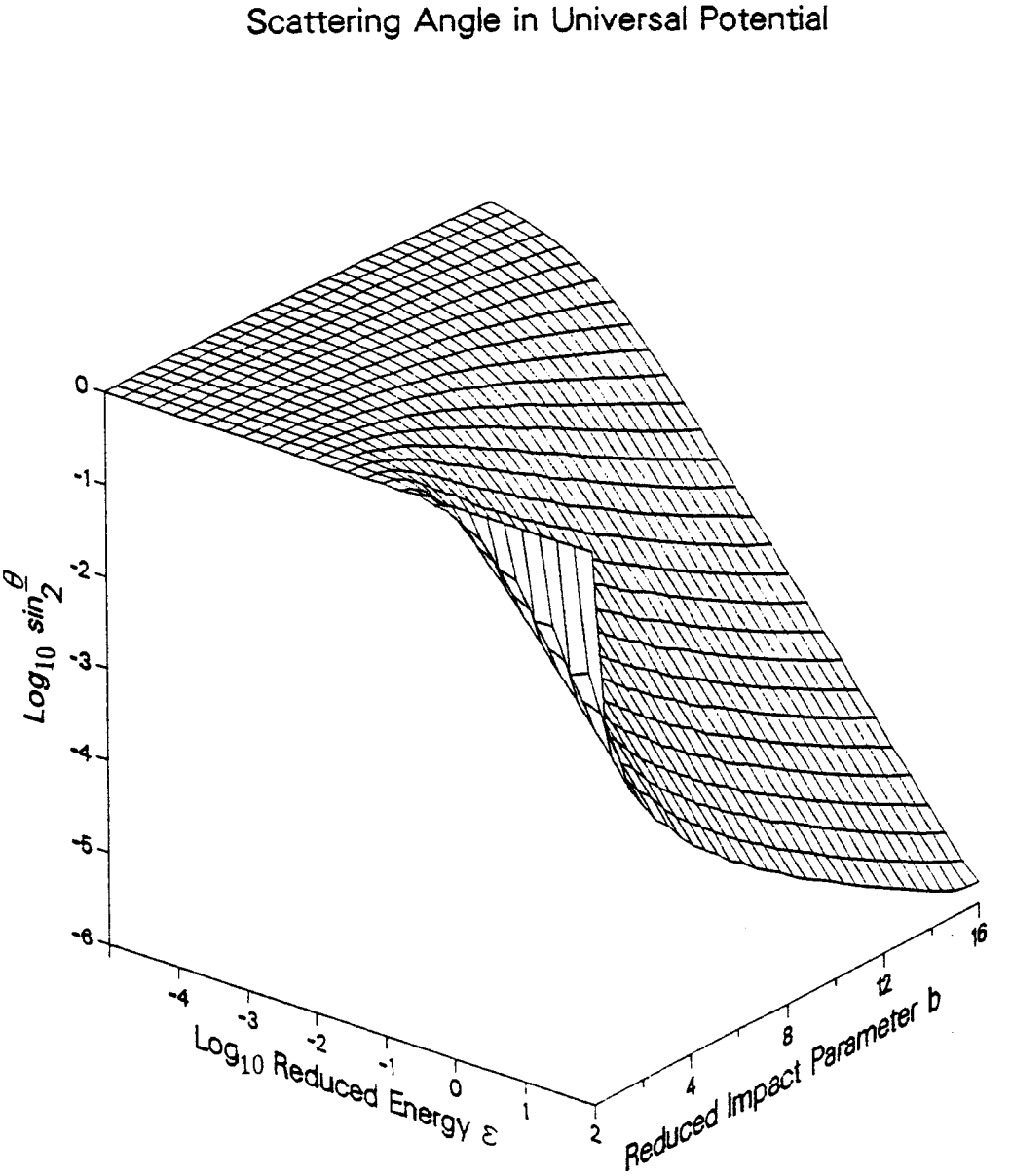

Figure 5.6: Scattering angle for the Universal potential

The program does not perform the numerical integration during its run because of the long cpu time devoted to the repeated integration. Instead, it evaluates the scattering angles using two dimensional scattering angle table that is prepared beforehand as a function of ϵ and b for a specific interatomic potential. The scattering angle is calculated at any ϵ and b from a 2-dimensional interpolation with the table. At very high energy or with a small impact parameter compared to energy, the simple Coulomb potential is used, which gives the analytic expression for the scattering angle as

$$\theta_{Coul} = 2\tan^{-1}(\frac{1}{2\epsilon b}) \quad \text{if} \quad \epsilon > 10^3, \text{or} \, b < 0.05(1+\log\epsilon) \tag{5.47}$$

The average relative error was estimated as low as 0.2 % and the maximum error of about 3 % at high energies with small impact parameters, which doesn't contribute much to the final result because the collision with a small impact parameter has the lowest probability to occur.

Eventually, the scattering angle in the center of mass system is converted to the scattering angles of the incident particle and the recoil atom in the laboratory frame using the relation as

$$\begin{aligned} \vartheta_1 &= \tan^{-1}(\frac{M_2 \sin\theta}{M_1 + M_2\cos\theta}) \\ \vartheta_2 &= \frac{\pi - \theta}{2} \end{aligned} \tag{5.48}$$

, where ϑ_1 and ϑ_2 are the scattering angles of the incident and recoil particles respectively.

The azimuthal scattering angle φ can be calculated from the assumption of the azimuthal symmetry, which yields

$$\varphi_1 = 2\pi R \tag{5.49}$$

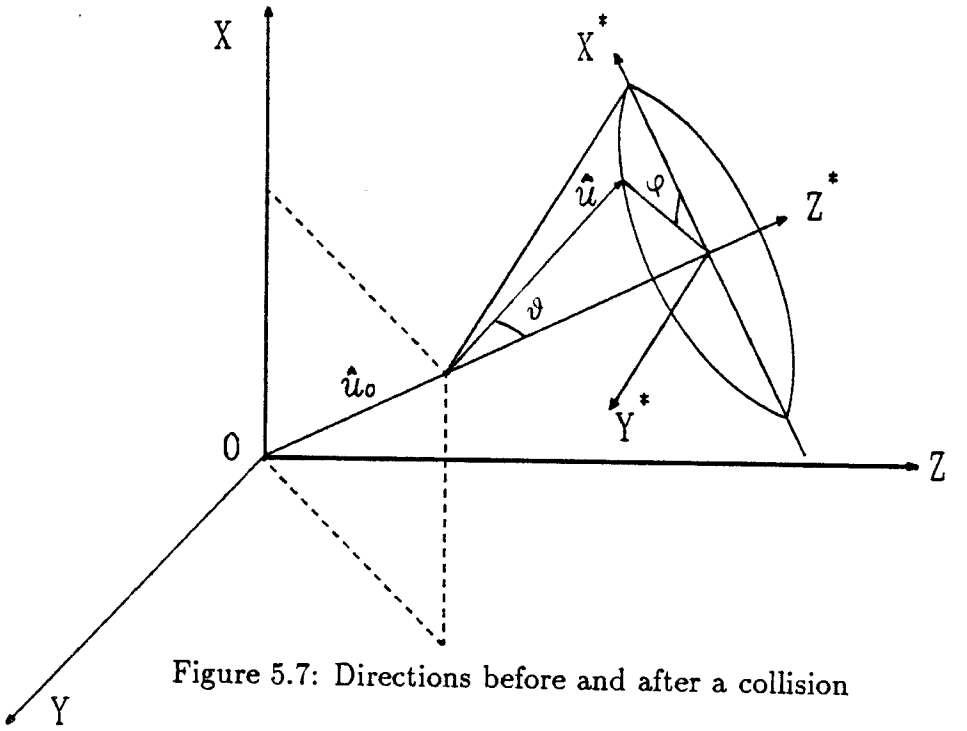

Figure 5.7: Directions before and after a collision

$$\varphi_2 = \pi - \varphi_1$$

, where R is a random number.

New direction after collision

To track the particle position we have to know the new direction after a collision. Suppose that we wish to calculate the new direction $\hat{u}$ from the original direction $\hat{u}_0$, scattering angle ϑ, and azimuthal scattering angle φ, which is illustrated in Fig. 5.7. $\hat{u}$ and $\hat{u}_0$ can be expressed with their direction cosines with respect to X, Y, and Z axis respectively as

$$\begin{aligned} \hat{u}_0 &= (a_{x0}, a_{y0}, a_{z0}) \\ \hat{u} &= (a_x, a_y, a_z) \end{aligned} \tag{5.50}$$

From the figure it can be seen that

$$\hat{u} = \sin\vartheta\cos\varphi\hat{x}^* + \sin\vartheta\sin\varphi\hat{y}^* + \cos\vartheta\hat{z}^* \tag{5.51}$$

, where $\hat{x}^*$, $\hat{y}^*$, and $\hat{z}^*$ are the unit vectors in the new coordinate system X^*, Y^*, and Z^*. Obviously,

$$\hat{z}^* = \hat{u}_0 = (a_{x0}, a_{y0}, a_{z0}) \tag{5.52}$$

Because the plane from which the azimuthal angle φ is defined is arbitrary, we can take a plane that is normal to the $Y - Z$ plane. To get $\hat{x}^*$, we can use the relations as

$$\begin{aligned} \hat{x}^* \cdot \hat{u}_0 &= 0 \\ \hat{x}^* \cdot \hat{x} &= \sqrt{1 - a_{x0}^2} \end{aligned} \tag{5.53}$$

, which gives $\hat{x}^*$ as

$$\hat{x}^* = \frac{1}{\sqrt{1 - a_{x0}^2}}(1 - a_{x0}^2, -a_{x0}a_{y0}, -a_{x0}a_{z0}) \tag{5.54}$$

Furthermore, $\hat{y}^*$ can be obtained using $\hat{y}^* = \hat{z}^* \times \hat{x}^*$, which yields

$$\hat{y}^* = \frac{1}{\sqrt{1 - a_{x0}^2}}(0, a_{z0}, -a_{y0}) \tag{5.55}$$

Using the eq.(5.51), we finally get the expression for the new direction cosines as

$$\begin{aligned} a_x &= \sqrt{1 - a_{x0}^2}\sin\vartheta\cos\varphi + a_{x0}\cos\vartheta \\ a_y &= \frac{-a_{x0}a_{y0}\sin\vartheta\cos\varphi + a_{z0}\sin\vartheta\sin\varphi + a_{y0}\sqrt{1 - a_{x0}^2}\cos\vartheta}{\sqrt{1 - a_{x0}^2}} \\ a_z &= \frac{-a_{x0}a_{z0}\sin\vartheta\cos\varphi - a_{y0}\sin\vartheta\sin\varphi + a_{z0}\sqrt{1 - a_{x0}^2}\cos\vartheta}{\sqrt{1 - a_{x0}^2}} \end{aligned} \tag{5.56}$$

Similarly, the new direction cosines for the recoil atom can be obtained with its axial scattering ϑ_2 and azimuthal scattering angle φ_2.

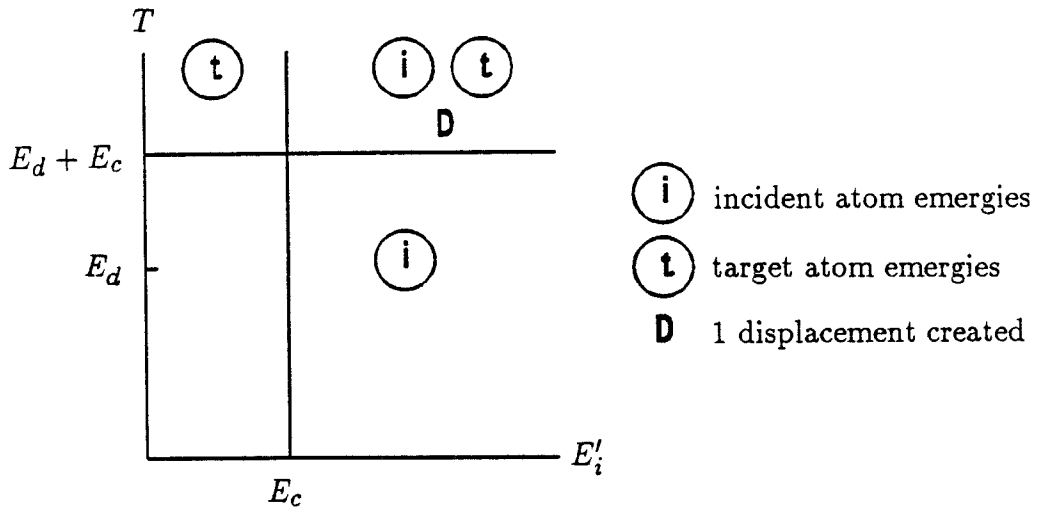

Figure 5.8: Displacement model used in TAMIX

5.2.2 Displacement model

A modified Kinchin-Pease model [12] is used for the defect production mechanism in TAMIX, which is illustrated in Fig. 5.8. In the figure, E_i' denotes the energy of the incident atom after collision, T denotes the energy transferred to the target atom, and E_c is the cutoff energy at which the particle trajectory is terminated.

To accurately assess the defect distribution one has to follow all of the recoils generated, which needs a large amount of computation time. However, an approximation can be made for the higher order recoils using an analytical expression for the defect production because the higher order recoils have lower energies and do not penetrate a long distance from their creation points. The

program TAMIX uses the expression given by Robinson [13].

$$\nu(T) = \begin{cases} 0.8\frac{E_\nu}{2E_d} & \text{if} \quad 2E_d \leq E_\nu \\ 1 & \text{if} \quad E_d \leq E_\nu < 2E_d \\ 0 & \text{if} \quad E_\nu < E_d \end{cases} \tag{5.57}$$

, where

$$E_\nu = \frac{T}{1 + k_d g(\varepsilon_d)} \tag{5.58}$$

, where

$$\begin{aligned} k_d &= 0.1334 Z_2^{2/3} M_2^{-1/2} \\ g(\varepsilon_d) &= \varepsilon_d + 0.40244\varepsilon_d^{3/4} + 3.4008\varepsilon_d^{1/6} \end{aligned} \tag{5.59}$$

, where $\varepsilon_d = 0.01014 Z_2^{-7/3} T$.

Usually the displacement energy E_d is defined in the bulk far from the target surface. It is the minimum energy to create a stable Frenkel pair survived from the instantaneous recombination. The minimum distance between vacancy and interstitial is supposed to be $3 \sim 5$ interatomic spacings [14]. However, in the sputtering process most of the sputtered atoms come from the near-surface atomic layers, from which the surface binding energy is necessary for an atom to be ejected. Especially for an atom located just at the surface we can assume that the effective displacement energy would be zero. From this simple argument it can be concluded that there should be some smooth transition of the effective displacement energy near the surface of the target from 0 to the bulk value E_d. In the view that the binding energy is proportional to the number of bonds by which an atom is connected, the displacement energy can be modeled as

$$E_d \propto \text{number of bonds} \propto \text{volume} \propto z^3 \tag{5.60}$$

, where z is the distance from the surface in the unit of interatomic spacing. Therefore, E_d can be expressed as

$$E_d(z) = \begin{cases} E_d(\frac{z}{n_{sl}})^3 & \text{if} \quad z < n_{sl} \\ E_d & \text{if} \quad z \geq n_{sl} \end{cases} \tag{5.61}$$

, where n_{sl} is the number of atomic layers considered as the surface region($\sim$ 8).

5.2.3 Sputtering process

Sputtering model

When a moving atom reaches the surface directing outwards, it is considered to be sputtered if it has enough energy to surmount the surface barrier denoted by the surface binding energy. Because of the existence of material's discontinuity at the surface, it is necessary to modify some of the collision model in the near-surface region. In addition to the scattering cross section the impact parameter selection model should also be modified.

The surface model adopted in TAMIX is the 'random surface model', in which the atomically rough nature of the surface is modeled along with the distant collisions that are presumably believed to occur at the surface. The idea of random surface model is shown schematically in Fig. 5.9, where the geometric surface is a fixed mathematical boundary between the target and the vacuum. However, it is very unusual to have such atomically flat surface, especially during ion bombardment. Hence, for a collision near the surface

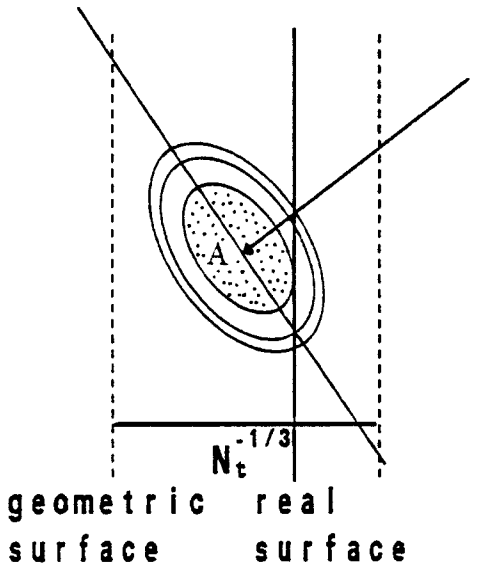

Figure 5.9: Illustration of the random surface model

another plane is constructed randomly within the first interatomic distance from the geometric surface, which will be called the real surface hereafter. The location of the real surface is given by

$$z_{rs} = RN_t^{-\frac{1}{3}} \tag{5.62}$$

, where R is a random number, and N_t is the target atomic density in the surface region. Suppose that a moving atom has come to make a collision at the position A in the direction shown. The first trial to search for its collision partner will be made on the disc with a radius p_{max}, which is perpendicular to the direction of the moving atom. Two random numbers are used to locate the position of the target atom, one of which is for the impact parameter and the other for the azimuthal scattering angle. If the target atom found in this way is inside of the real surface, then the moving atom is forced to

make a collision with that target atom. If it is outside the real surface, the search will be tried on an adjacent concentric ring disc which has the same area as the first disc, checking the position of the target atom. In this way, the probability for each trial will be the same. If the last trial(set to 3 in TAMIX) fails, the moving atom is considered not to make a collision at that position and proceeds further for a next collision. A moving atom is considered to be out of the target only if it reaches the geometric surface with enough energy to overcome the surface potential. Otherwise, it is considered to remain inside of the target, making collisions and moving through the solids.

The binding energy between atoms on the target surface influences sputtering in two ways, First, it provides a barrier which must be surmounted by escaping atoms and hence plays an important role in determining the sputtering yield. Second, its directional properties influence the direction taken by the sputtered atoms. Two forms of surface barrier have been considered in TAMIX [15]. One is a planar surface barrier and the other is a spherical(or isotropic) surface barrier, which are expressed respectively as

$$U = \begin{cases} \frac{E_s}{\cos^2\theta} & : \text{planar surface barrier} \\ E_s & : \text{spherical surface barrier} \end{cases} \tag{5.63}$$

, where θ is the angle from the surface normal and E_s is the magnitude of the surface binding energy. The planar potential is more suitable for most metal targets and the isotropic potential is better for semiconductors.

In the planar barrier parallel to the target surface, only the normal component of the velocity is affected. Consequently, the atom is refracted away from the surface normal and if its normal component is low enough, it may even be

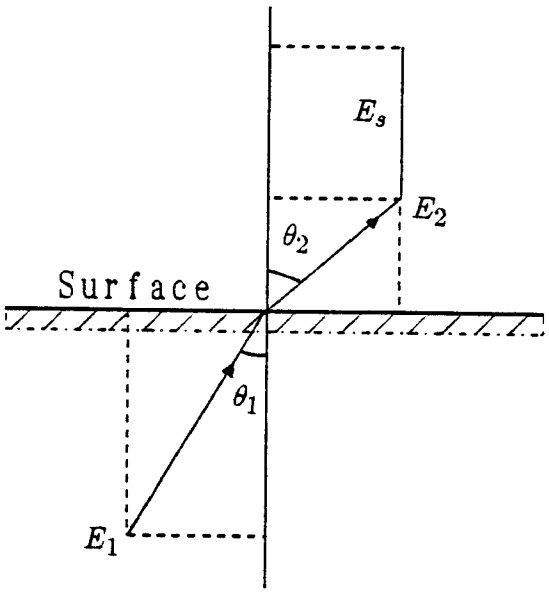

Figure 5.10: Refraction of the sputtered atom by a planar surface barrier

reflected back into the solid. The amount of refraction can be calculated with Fig. 5.10, which gives the component-energy conservation as

$$\begin{aligned} E_1 \sin^2\theta_1 &= E_2 \sin^2\theta_2 \\ E_1 \cos^2\theta_1 &= E_2 \cos^2\theta_2 + E_s \end{aligned} \tag{5.64}$$

, where E_1, θ_1 are the energy and angle of the atom before passing the surface barrier respectively and E_2, θ_2 are those after it is sputtered. The final expression for the energy and angle taken by the sputtered atom will be

$$\begin{aligned} E_2 &= E_1 - E_s \\ \cos\theta_2 &= \sqrt{\frac{E_1 \cos^2\theta_1 - E_s}{E_1 - E_s}} \end{aligned} \tag{5.65}$$

According to the above equation, it can be easily seen that for a given angle, θ_1, there should be a minimum energy for sputtering given by

$$E_{1,min} = \frac{E_s}{\cos^2 \theta_1} \tag{5.66}$$

, in other words, if the energy of the atom reaching the surface is smaller than $E_{1,min}$, then it will be reflected back into the solid.

In an isotropic surface barrier, there is no refraction at the surface, hence the energy and direction of the sputtered atom will be given by

$$\begin{aligned} E_2 &= E_1 - E_s \\ \theta_2 &= \theta_1 \end{aligned} \tag{5.67}$$

As in the planar barrier, if the energy is lower than E_s, then it will be also be reflected back into the target.

Surface binding energy

For a single element target, the sublimation energy ΔH^s will be a good approximation to the surface binding energy E_s. However, in multicomponent targets such as alloys or compounds, the surface binding energy should be different from element to element. The surface binding energy in a general multicomponent target can be modeled using 'pair binding model', in which only the nearest neighbor interactions are considered. If we denote the binding energy for a pair of atoms as U, then for a pure elemental target

$$E_s = \frac{Z}{2} U = \Delta H^s \tag{5.68}$$

, where Z is the coordination number and in the expression it is divided by 2 because the number of bonds at the surface is half of that in the bulk. Suppose that A and B form a binary alloy with composition χ_A and χ_B, then the heat of mixing per atom will be expressed as

$$\Delta H^m = Z\chi_A\chi_B(\frac{U_{AA}+U_{BB}}{2} - U_{AB}) \tag{5.69}$$

, where the coordination number Z is assumed to be the same for each component and U_{AA}, U_{BB}, and U_{AB} are the binding energy between $A-A$, $B-B$, and $A-B$ atom pairs respectively. Similarly, if A and B make a compound with a known composition χ_A^c and χ_B^c, then

$$\Delta H^f = Z\chi_A^c\chi_B^c(\frac{U_{AA}+U_{BB}}{2} - U_{AB}) \tag{5.70}$$

, where ΔH^f is the heat of formation of the compound per atom. Hence, we can obtain the general expression for U_{ij} as

$$\begin{aligned} U_{ij} &= \frac{1}{Z}(\frac{Z}{2}U_{ii} + \frac{Z}{2}U_{jj} - \frac{\Delta H^f}{\chi_i^c\chi_j^c}) \\ &= \frac{1}{Z}(\Delta H_{io}^s + \Delta H_{jo}^s - \frac{\Delta H^f}{\chi_i^c\chi_j^c}) \end{aligned} \tag{5.71}$$

, where ΔH_{io}^s and ΔH_{jo}^s are the heat of sublimation of i and j component in their elemental state and ΔH^f is the heat of formation(or mixing) per atom of the compound(or alloy).

As in the elemental target, the surface binding energy of the ith component can be expressed as

$$E_s^i = \frac{Z}{2}\sum_{j=1}^{n}\chi_j U_{ij} \tag{5.72}$$

, where n is the number of components in the target. Inserting eq.(5.71) for U_{ij}, we can get the final expression for the surface binding energy of the ith element in a multicomponent target as

$$E_s^i = \frac{1}{2}\sum_{j=1}^{n}\chi_j(\Delta H_{io}^s + \Delta H_{jo}^s - \frac{\Delta H^f}{\chi_i^c\chi_j^c}) \tag{5.73}$$

In Fig. 5.11, the component surface binding energies are shown for a binary alloy with $\Delta H^f = 0$ as in ideal solution.

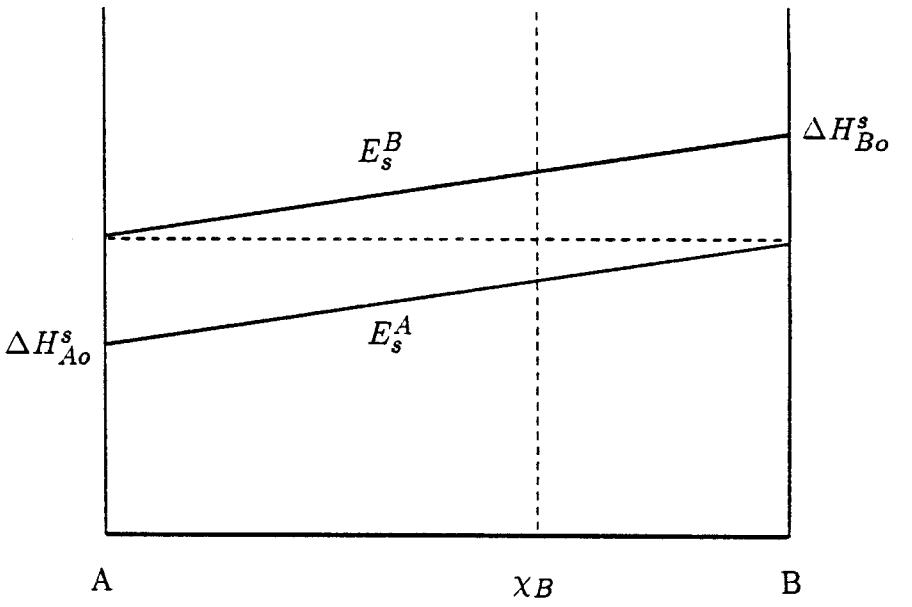

Figure 5.11: Component surface binding energy for an ideal binary solution

5.2.4 Optimization

Importance sampling

As discussed in section **1.2**, the program TAMIX adopts splitting and Russian roulette as a variance reduction technique. In the target, one important region is designated with an importance I and the importance of the unimportant region is set to 1. If a particle enters the important region from an unimportant region, then the splitting is activated such that the particle is replaced with I equivalent particles, each with a weight reduced by $\frac{1}{I}$ and the split particles are followed individually. On the other hand, if a particle is coming out of the important region to unimportant region, then the Russian roulette is applied as follows. First, a random number R between 0 and 1 is generated. Next, if R is greater than$\frac{1}{I}$. then the particle is killed. If R is

smaller than $\frac{1}{I}$, the weight of the particle is increased by I, then is followed further. In this way, the total weight of the system is preserved and more precise picture is taken in the important region compared to the unimportant region.

Vectorization

The state-of-the-art supercomputers such as Crays and CYBER-205 are characterized by their special capabilities for vectorized or parallel calculations. However, their full potential speed is attainable only in 'vectorized' programs. The very nature of Monte Carlo program precludes direct conversion of scalar codes to the vector computers. Indeed, the effective vectorization of Monte Carlo program can be achieved only through major changes in global algorithms and careful selection of compatible physics treatment. The vectorized algorithm may be described as an 'event-based' algorithm versus the conventional 'history-based' algorithms of scalar Monte Carlo codes. In a scalar Monte Carlo algorithm, one particle at a time is followed until its history is terminated. In a vectorized Monte Carlo code, the algorithm follows 'event'-a portion of a history, and processes the particle vector for many events, continually updating the particle vector by eliminating depleted particles and adding new particles until the requisite number of simulation is performed. There have been studies related with the vectorization of scalar Monte Carlo codes, increasing the speed by a factor of $20 \sim 85$ [16,17,18]. The program TAMIX is vectorized such that a given number of ions are followed simultaneously, continuously adding the generated recoil atoms in the particle

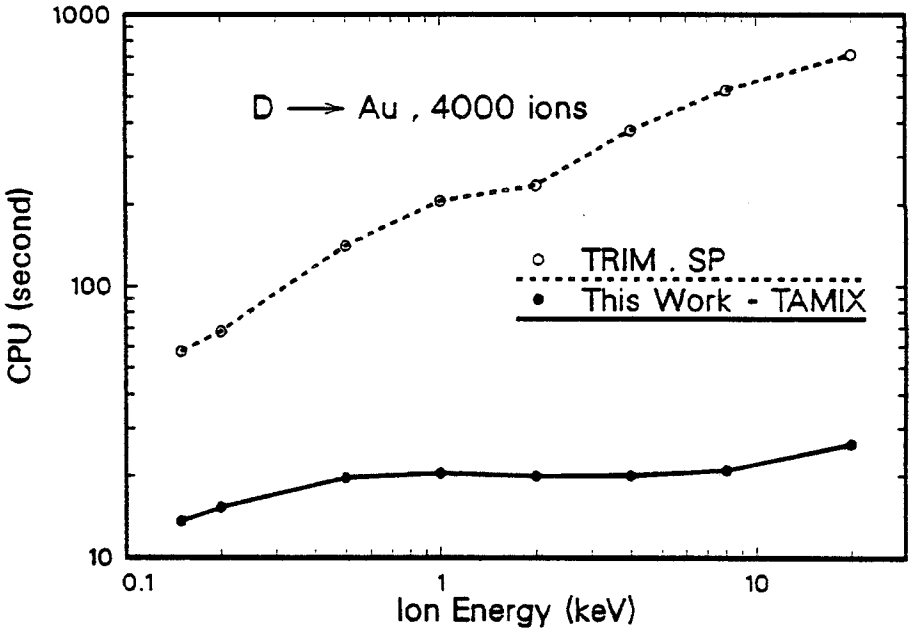

Figure 5.12: CPU comparison with TRIM.SP and TAMIX for a sputtering calculation, D on Au

stack until all of the moving atoms are deleted from the stack by one of the termination mechanisms. Then, the next ion bundle is followed until the given number of ion histories are simulated.

In Fig. 5.12, the CPU's used with TRIM.SP code [19]-most heavily used sputtering code and TAMIX code are compared for a sputtering calculation for D on Au with 4000 ion histories. As seen in the figure, the non-analogue and vectorized TAMIX code is more than 20 times faster than the analogue and non-vectorized TRIM.SP at the highest energy investigated of 20 keV. The speed gain at the lowest energy of 0.15 keV is about 4. The increased speed gain at the higher ion energy comes from the fact that for higher ion energy more recoils are generated, all of which are added to the particle stack

and followed simultaneously in TAMIX. Similarly, it can be expected that the speed gain will be higher for heavy ions than for light ions for the same reason.

Other features

For the purpose of efficient use of the program to a given specific problem, some special features are built in TAMIX. The first thing is the grouping of the recoils. The incident ion is designated as group 0. The primary recoils will have the group index 1, the secondaries 2, and so on. For example, if we are interested only in the ion distribution, we just need to follow the ion, ignoring the recoils. Hence, the group number to be followed will be set to 0. Furthermore, in some problems the exact results, which are only attainable by following all of the recoils, can be approximated by using a smaller group number without spending much simulation time. This grouping of recoils are shown schematically in Fig. 5.13.

The second feature is the use of dynamic memory allocation because the actual memory size necessary to store the particle information depends on the specific problem. For example, the number of recoils generated by light ions is much smaller than that by heavy ions. Since the size of an executable program strongly depends on the memory size used, the appropriate use of the dynamic memory allocation routine will increase the efficiency of the program.

5.2.5 Dynamic simulation

The program TAMIX is a dynamic Monte Carlo program which can simulate the dynamic change of the target as a function of ion fluence. Actually,

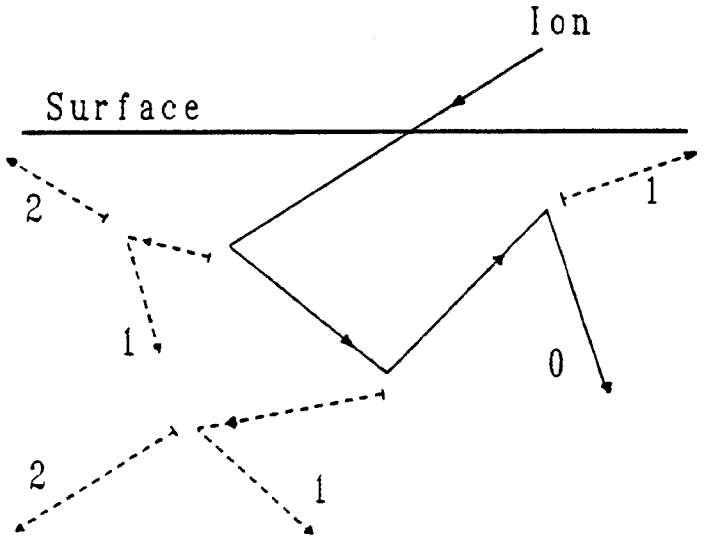

Figure 5.13: Grouping of recoils

at low ion fluence the problem can be simulated using the static simulation because the target is not much different from the initial target. However, at high ion fluence the target is changing significantly from the initial state. Also, the ions implanted previously will behave as another target species, affecting the ions bombarding later.

The dynamic feature of the TAMIX is carried out by use of the 'pseudo-particles' and layering of the target. A pseudo-particle is a particle that is equivalent to a given number of real particles(ions, target atoms). Suppose that the total ion fluence Φ_t is simulated with N_H ion histories. Then, each pseudo-ion corresponds to $\frac{\Phi_t}{N_H}$ ions. Also, the target atoms contained in a small layer are scaled accordingly, that is, if a layer has N_t target atoms per unit area, the number of pseudo-particles associated with the layer will be

$$N_{pp} = \frac{N_t}{(\Phi_t / N_H)} \tag{5.74}$$

Of course, these N_{pp} pseudo-particles are distributed according to the atomic fraction in the layer such that

$$N_{pp}^i = N_{pp} C_i \tag{5.75}$$

, where C_i is the atomic fraction of ith atom in that layer. The deposition and removal of each atomic species for all layers are recorded during the history of one pseudo-ion. After the termination of a pseudo-ion history, the net change in each layer is calculated. Because the accumulation or depletion of pseudo-particles gives physically unreasonable atomic densities in some layers, each layer is relaxed to the normal density using the corresponding atomic volume of each component. Furthermore, to prevent the averaging effect in the extremely expanded layers due to accumulation, the expanded layers are appropriately divided such that its thickness lies between $0.5\Delta z_o$ and $1.5\Delta z_o$, where Δz_o is the initial thickness of the layers. Also, if a layer is collapsed to a thickness smaller than $0.5\Delta z_o$, then it is combined with the next layer to give the new thickness and composition. Using this dynamic capability of TAMIX, not only the collisional mixing in the bulk but also the erosion of the surface due to sputtering can be properly taken into account as a function of ion fluence.

It is not an easy task to determine the proper number of the simulated ion histories for a given ion fluence. If too small number of ion histories is used, the result will be far from the real situation. On the other hand, if too many ion histories are used, it will require extreme computation time even though

it is closer to the real world. In TAMIX, the maximum fractional number change in a layer is being checked to be around 0.2. If it is much higher than 0.2, one has to use more ion histories. On the other hand, if it is much smaller than 0.2, a fewer number of ion histories can be used to save the computation time.

5.2.6 Diffusion incorporation

The radiation enhanced diffusion due to the high point defect concentration produced during ion irradiation and the radiation induced segregation caused by coupling of defect and atom fluxes were described by the diffusion equation in section **4.3**. In one dimension as in ion irradiation, the resulting equation will be

$$\begin{aligned}
\frac{\partial C_v}{\partial t} &= K_o - L_{vd} - L_r - \sum_j d_{vj}\left(\frac{\partial}{\partial x}\left(C_v\frac{\partial C_j}{\partial x}\right) - \frac{\partial}{\partial x}\left(C_j\frac{\partial C_v}{\partial x}\right)\right) \quad (5.76)\\
\frac{\partial C_i}{\partial t} &= K_o - L_{id} - L_r + \sum_j d_{ij}\left(\frac{\partial}{\partial x}\left(C_i\frac{\partial C_j}{\partial x}\right) + \frac{\partial}{\partial x}\left(C_j\frac{\partial C_i}{\partial x}\right)\right)\\
\frac{\partial C_j}{\partial t} &= d_{ij}\frac{\partial}{\partial x}\left(C_i\frac{\partial C_j}{\partial x} + C_j\frac{\partial C_i}{\partial x}\right) + d_{vj}\frac{\partial}{\partial x}\left(C_v\frac{\partial C_j}{\partial x} - C_j\frac{\partial C_v}{\partial x}\right)\\
&, \quad j = 1, \cdots, n
\end{aligned}$$

with

$$\begin{aligned}
L_{vd} &= \frac{2\pi\rho_d}{\ln(R_d/R_o)}(C_v - C_v^{eq})\sum_j d_{vj}C_j \quad (5.77)\\
L_{id} &= \frac{2\pi\rho_d}{\ln(R_d/R_o)}C_i\sum_j d_{ij}C_j\\
L_r &= 4\pi C_v C_i \sum_j \left(\frac{6(d_{ij}+d_{vj})}{\lambda_j^2 Z_j}C_j\right)
\end{aligned}$$

and

$$d_{vj} = \frac{\lambda_j^2}{6} Z_j \nu_{vj} \exp(-\frac{E_{vj}^m}{kT}) \qquad (5.78)$$
$$d_{ij} = \frac{\lambda_j^2}{6} Z_j \nu_{ij} \exp(-\frac{E_{ij}^m}{kT})$$

, where the notations are the same as in section **4.3**. In the TAMIX program this diffusion equation is numerically solved simultaneously, along with the collisional part of the code as follows. First, the total irradiation time is appropriately divided with a global time step Δt_g. Next, the corresponding number of ion histories are followed without diffusion, creating defects and modifying the target by only collisional processes. Then, the resulting target profile is used as an initial condition to solve the diffusion equation from time=0 to time=Δt_g. The defect production rate is assumed to be constant during diffusion, which is

$$K_o(x) = \frac{\Delta C_d(x)}{\Delta t_g} \qquad (5.79)$$

, where $\Delta C_d(x)$ is the depth-dependent defect concentration resulted from the collisional simulation in Δt_g. The concentration profile obtained from the diffusion equation will then be used as an initial target configuration for the next collisional simulation, and so on.

Numerical technique

To solve the diffusion equation, TAMIX uses 'methods of lines', in which the space variable x is discretized while leaving the time t continuous [20,21]. The resulting system of stiff ordinary differential equation is solved with an

ODE solver(LSODE) [22] in Crays along with boundary conditions. Since the target geometry in ion irradiation is semi-infinite, the boundary conditions will be

$$\begin{aligned} C_v(0,t) &= C_v^{eq} \\ C_i(0,t) &= C_i^{eq} \end{aligned} \tag{5.80}$$

at the surface and

$$\begin{aligned} C_v(\infty,t) &= C_v^{eq} \\ C_i(\infty,t) &= C_i^{eq} \\ C_j(\infty,t) &= C_j^o \quad , \quad j=1,\cdots,n \end{aligned} \tag{5.81}$$

, where C_j^o is the initial concentration of the jth atom far from the surface. The missing boundary condition can be obtained from the conservation of atoms in the target, that is

$$\frac{\partial}{\partial t}\int_0^\infty C_j(x,t)dx = 0 \quad , \quad j=1,\cdots,n \tag{5.82}$$

The space is discretized with its nodal values $x^1, x^2, \cdots, x^N$, where x^1 corresponds to the surface and x^N to the point far inside the target. The nodes near the surface are made denser than in the bulk since large concentration gradients will develop near the surface. At the kth node the differencing can be made with

$$\begin{aligned} \frac{\partial}{\partial x}(C_1\frac{\partial C_2}{\partial x}) \simeq \frac{2}{(h^{k-1}+h^k)}\Bigg(& C_1^{k+\frac{1}{2}}\frac{C_2^{k+1}-C_2^k}{h^k} \\ & -C_1^{k-\frac{1}{2}}\frac{C_2^k-C_2^{k-1}}{h^{k-1}}\Bigg) \end{aligned} \tag{5.83}$$

$$= \frac{1}{h^{k-1}+h^k}\left\{\frac{(C_1^k+C_1^{k+1})(C_2^{k+1}-C_2^k)}{h^k} - \frac{(C_1^{k-1}+C_1^k)(C_2^k-C_2^{k-1})}{h^{k-1}}\right\}$$

, where $k = 2, \cdots, N-1$ and $h^k = x^{k+1} - x^k$. Applying this to the diffusion equation yields $(n+2)(N-2)$ ordinary differential equations for n component target.

At the right boundary($x = x^N$),

$$\frac{\partial C_v^N}{\partial t} = \frac{\partial C_i^N}{\partial t} = \frac{\partial C_j^N}{\partial t} = 0 \quad , \quad j = 1, \cdots, n \tag{5.84}$$

At the surface($x = x^1$),

$$\frac{\partial C_v^1}{\partial t} = \frac{\partial C_i^1}{\partial t} = 0 \tag{5.85}$$

However, for the jth atomic component, we only have the implicit boundary condition given by eq.(5.82) imposing the atom conservation. The equation for the jth component can be rewritten as

$$\frac{\partial C_j}{\partial t} = -\frac{\partial}{\partial x}(\Omega J_j) \quad , \quad j = 1, \cdots, n \tag{5.86}$$

Inserting this into eq.(5.82) and noting that at the right boundary all of the fluxes are 0,

$$\begin{aligned} \int_0^\infty -\frac{\partial}{\partial t}(\Omega J_j)dx &= \Omega J_j \mid_{x=0} -\Omega J_j \mid_{x=\infty} \\ &= \Omega J_j \mid_{x=0} \\ &= 0 \end{aligned} \tag{5.87}$$

Thus, the differencing at the surface yields

$$\begin{aligned} \frac{\partial C_j^1}{\partial t} &\simeq -\frac{1}{0.5h^1}(\Omega J_j^{\frac{3}{2}} - \Omega J_j^1) \\ &= -\frac{1}{0.5h^1}\Omega J_j^{\frac{3}{2}} \quad , \quad j = 1, \cdots, n \end{aligned} \tag{5.88}$$

Using the expression for ΩJ_j, we finally get

$$\begin{aligned} & \frac{\partial C_j^1}{\partial t} \\ \simeq \quad & \frac{1}{(h^1)^2}\left\{d_{ij}((C_i^1 + C_i^2)(C_j^2 - C_j^1) + (C_j^1 + C_j^2)(C_i^2 - C_i^1))\right. \\ + \quad & \left. d_{vj}((C_v^1 + C_v^2)(C_j^2 - C_j^1) - (C_j^1 + C_j^2)(C_v^2 - C_v^1))\right\} \\ , \quad & j = 1, \cdots, n \end{aligned} \tag{5.89}$$

5.2.7 Structure of TAMIX

The structure of TAMIX is shown in Fig. 5.14 with respect to the flow of logic.

- Input: reads the input file, atomic data file, and scattering angle table.
- Preparation: prepares the scattering cross section table, electronic stopping table, intermediate variables, and frequently used temporary variables. Only when preparing S_e table, subroutine HSTOP, HESTOP, HISTOP are used.
- Collisional: simulates the collisional processes, which is one of the major bodies of the program.
- Diffusional: solves the diffusion equation numerically.
- Output: outputs the results at intermediate and final ion fluences.

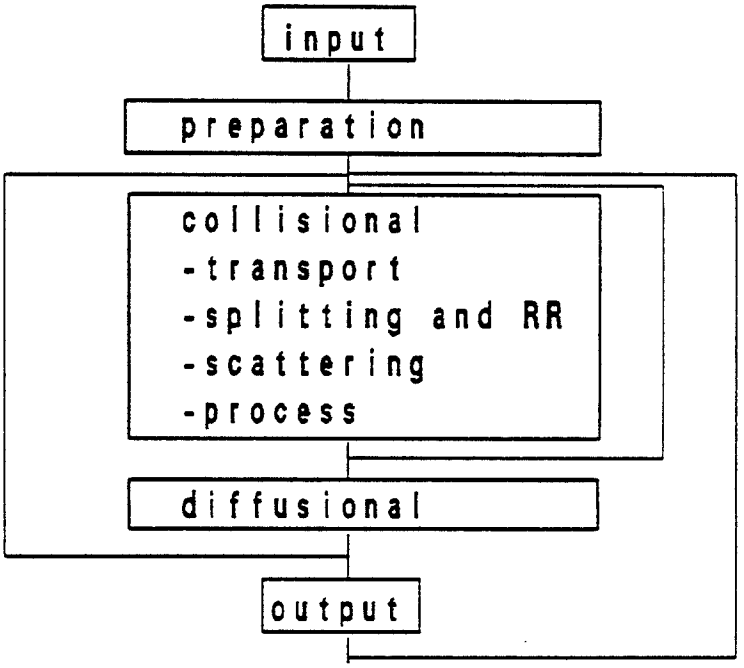

Figure 5.14: Structure of TAMIX

References

[1] G. H. Vineyard et al., Bull. Am. Phys. Soc. **5**, 26 (1960).

[2] J. B. Gibson et al., Phys. Rev. **120**, 1229 (1960).

[3] G. H. Vineyard, "Interatomic Potentials and Simulation of Lattice Defects", eds. P. C. Gehlen, J. R. Beeler, Jr., and R. I. Jaffee, Plenum Press, New York, 13 (1972).

[4] H. Kahn, "Applications of Monte Carlo", USA-AEC Report AECU-3259, The RAND Corporation (1956).

[5] W. Feller, "Introduction to Probability Theory and Its Applications", 2nd ed., John Wiley and Sons (1957).

[6] E. D. Cashwell and C. J. Everett, "A Practical Manual on the Monte Carlo Method for Random Walk Problems", Pergamon Press (1959).

[7] J. R. Beeler, Jr. and D. G. Besco, J. Appl. Phys. **34**, 3873 (1963).

[8] L. L. Carter and E. D. Cashwell, "Particle Transport Simulation with the Monte Carlo Method", USERDA TID-26607 (1975).

[9] Z. F. Ziegler, J. P. Biersack, U. Littmark, "Stopping and Range of Ions in Solids"(Pergamon Press, New York, 1985) Vol. **1**.

[10] H. H. Andersen and J. F. Ziegler, "The Stopping and Range of Ions in Matter"(Pergamon Press, New York, 1977) Vol. **3**.

[11] E. Everhart, G. Stone, and R. J. Carbone, Phys. Rev. **99**, 1287 (1955).

[12] G. H. Kinchin and R. S. Pease, Rep. Progr. Phys. **18**, 1 (1955).

[13] M. T. Robinson, "Nuclear Fission Reactors", British Nuclear Energy Society, London, p. 364 (1970).

[14] H. H. Andersen, Appl. Phys. **18**, 131 (1979).

[15] P. Sigmund, Phys. Rev. **184**, 383 (1969).

[16] F. B. Brown and W. R. Martin, Prog. Nucl. Energy **14**, 269 (1984).

[17] F. B. Brown, "Vectorized Monte Carlo Methods for Reactor Lattice Problems" in Proc. of the ANS Topical Meeting on Advances in Reactor Computations, Salt Lake City, UT, p 108 (1983).

[18] W. R. Martin, P. F. Nowak, and J. A. Rathkopf, IBM J. of Research and Development, Vol. **30**, No 2 (1986).

[19] J. P. Biersack and W. Eckstein, Appl. Phys. **A 34**, 73 (1984).

[20] G. D. Byrne and A. C. Hindmarsh, ACM Trans. Math. Software **1**, 71 (1975).

[21] S. M. Myers, D. E. Amos, and D. K. Brice, J. Appl. Phys. **47**, 1812 (1976).

[22] A. C. Hindmarsh, in "Scientific Computing"(eds. R. S. Stepleman et al.), p 55 (1983).

Chapter 6.

Results and discussion

The program TAMIX can be run in three modes, that is

1. **Static mode**

2. **C-Dynamic mode**(collisional)

3. **CD-Dynamic mode**(collisional and diffusional)

For low ion fluence, typically under 10^{16} ions/cm^2, the implanted ion concentration is quite low compared to that of the target atom and the target changes very little from its initial state. Hence, the program can be run in **Static mode**, where the modification of the target due to the bombarding ions is neglected.

At high ion fluence and at low target temperature, there should be a substantial modification of the target and the implanted ions will be incorporated as one of the target species for the ions arriving later. Thus, any nonself-ion irradiation will be eventually result in a multicomponent target, which is continuously modified. Furthermore, the low temperature of the target suppresses the diffusional processes, even though there is some possibility of enhanced diffusion due to the increased point defect concentration during ion irradiation. To see the dynamic response of the target for this case, the **C-dynamic mode** can be used, where only the collisional processes are considered. With

this mode the preferential sputtering, altered layer formation, collisional mixing and rearrangement of the target composition profiles can be studied as a function of ion fluence.

At high fluence with high target temperature, the diffusional process is triggered, which includes the surface segregation, radiation enhanced diffusion, and radiation induced segregation. In the program TAMIX, the several diffusional processes are considered, in which the radiation enhanced diffusion and radiation induced segregation are taken into account with the use of coupling of the partial fluxes between point defects and atomic species. This mode of TAMIX corresponds to the third mode, **CD-dynamic mode.** In the following sections, each run mode has been applied for the investigation of specific interest.

6.1 Static mode

6.1.1 Range and damage distribution

Fig. 6.1 shows the TAMIX calculation result of the damage and ion distribution for the 14 MeV Cu irradiation on Ni target along with the measured Cu distribution measured by L. M. Wang using AEM techniques [1]. The heavy ions are frequently used to simulate the neutron damage to the materials because of the higher damage efficiency compared to that of the fast neutrons [2]. The fluence was 6×10^{16} ions/cm^2 and the target temperature during irradiation was maintained to 500 °C. As seen in the figure, the projected range of the ion is quite the same as that from experiment. However,

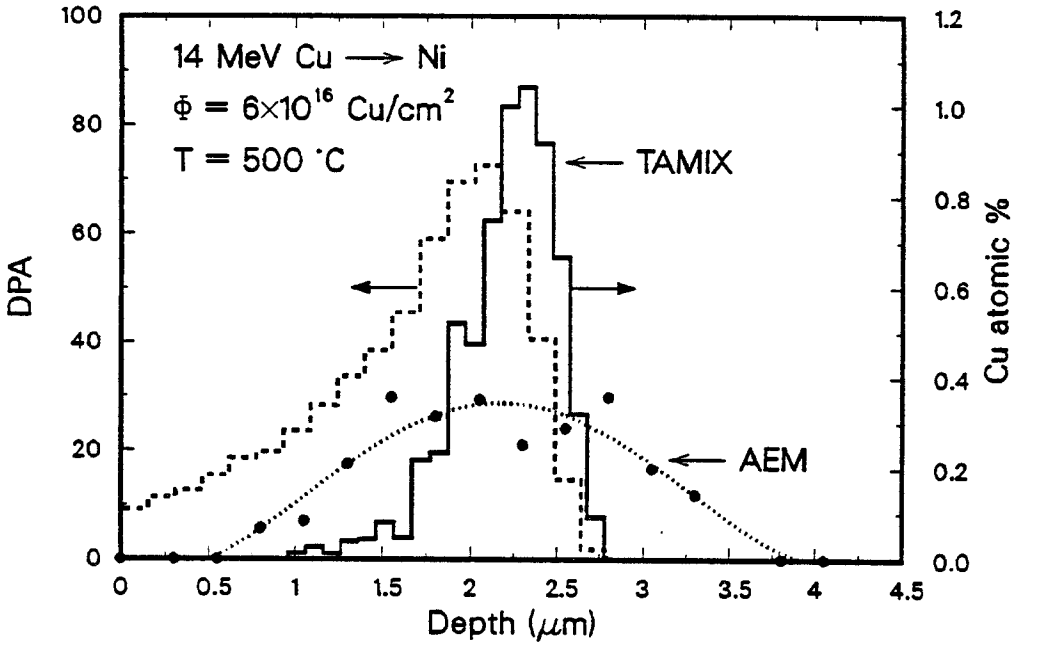

Figure 6.1: Ion and damage distribution for 14 MeV Cu in Ni

the measured Cu profile shows much broader distribution compared to the calculation, which is believed to be due to the high temperature of the target during irradiation. At this temperature the point defects are mobile, hence the diffusional processes are affecting the resultant profile. The peak of the damage profile is located at a shallower depth than that of the deposited ion peak. Moreover, the damage distribution curve is seen to be highly skewed in contrast to the almost Gaussian distribution of the implanted ions.

In Fig. 6.2, the projected range and straggling for Bi in Si are shown as a function of ion energy along with the experimental data [3,4]. It shows quite a good agreement with the experiment except the underestimation of the straggling especially at low energy region.

Because of the widespread use of ion implantation in the semiconductor

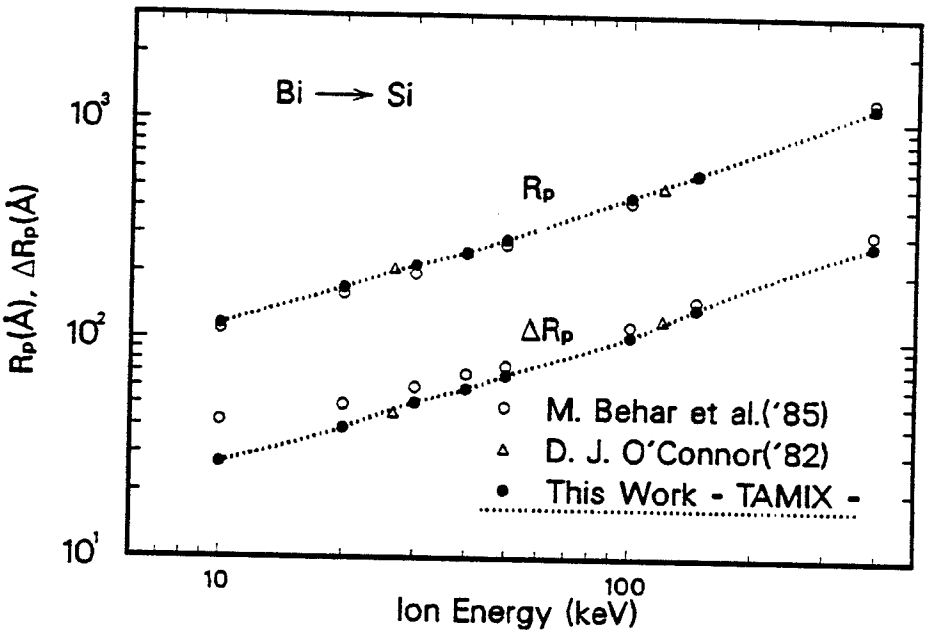

Figure 6.2: Projected range and range straggling of Bi in Si

industry, there has been a vast accumulation of range data for Si [3,4,5,6]. In Fig. 6.3, the heavy ion ranges and stragglings in Si are compared to the calculation result from the TAMIX code for three interatomic potentials, i.e. the Moliere approximation to the Thomas-Fermi potential, the Kr-C potential, and the recently suggested Universal potential. As seen in the range picture, the heavy ion ranges in Si can be reduced to a well-defined curve in reduced units except for Au. Because the nuclear stopping process dominates the ion stopping in this reduced energy region, it can be concluded that the interatomic potential for Au is different from the average behavior found in other elements, especially in the low energy region. Also, it can be seen that the results calculated with Universal potential gives the most satisfactory prediction to the experimental data. In the straggling picture, it can be noted that

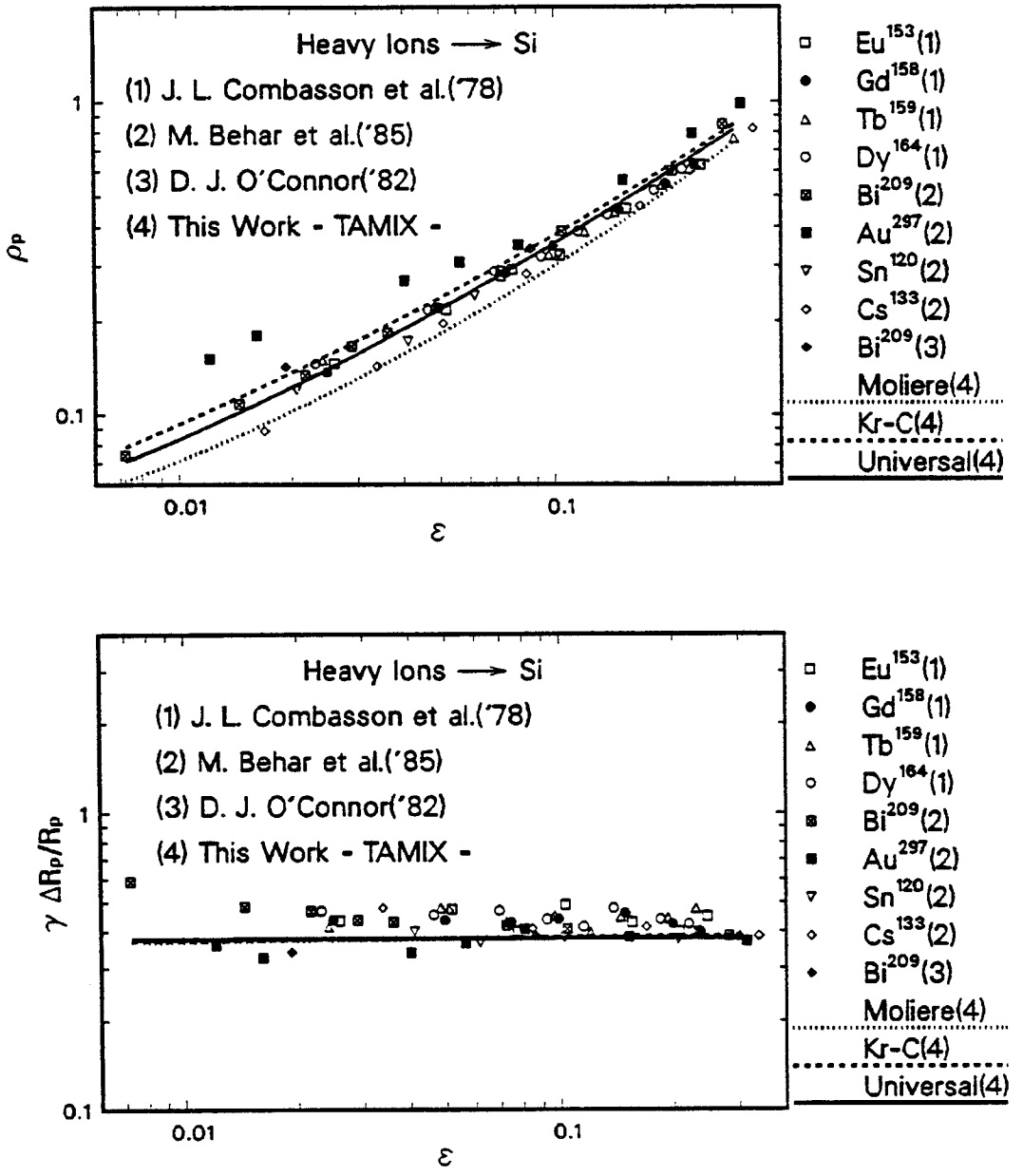

Figure 6.3: Projected range and range straggling of heavy ions in Si

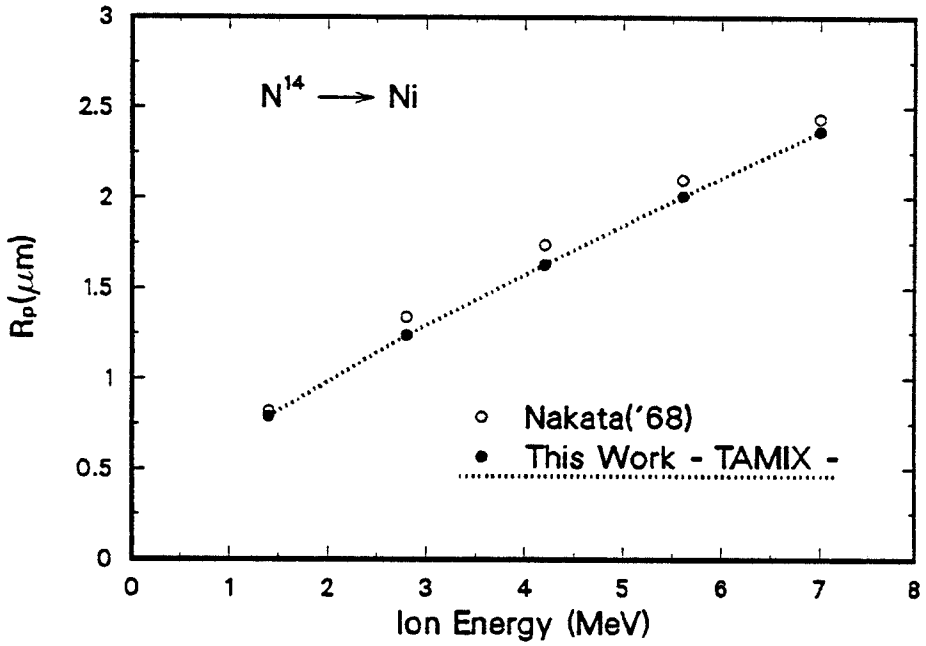

Figure 6.4: Projected range of N^{14} in Ni

the reduced stragglings do not depend strongly on the choice of the potential compared to the range. In the figure, γ is defined as $\frac{1}{\Lambda}$, where Λ is the energy transfer factor from ion to target atom.

In Fig. 6.4, the calculated projected range of MeV N^{14} in Ni is compared to the experimental data from Nakata [7], where it shows small underestimation. However, the agreement is quite satisfactory.

Conventional ion implantation to modify the surface region has been performed using various kinds of ion accelerators. Recently, a new technique to implant ions in the material has been developed, which utilizes the ion behavior in the plasma sheath near the material surface [8,9,10,11]. The new technique, so-called PSII(plasma source ion implantation) has shown to have significant advantages compared to the conventional beam line ion implanta-

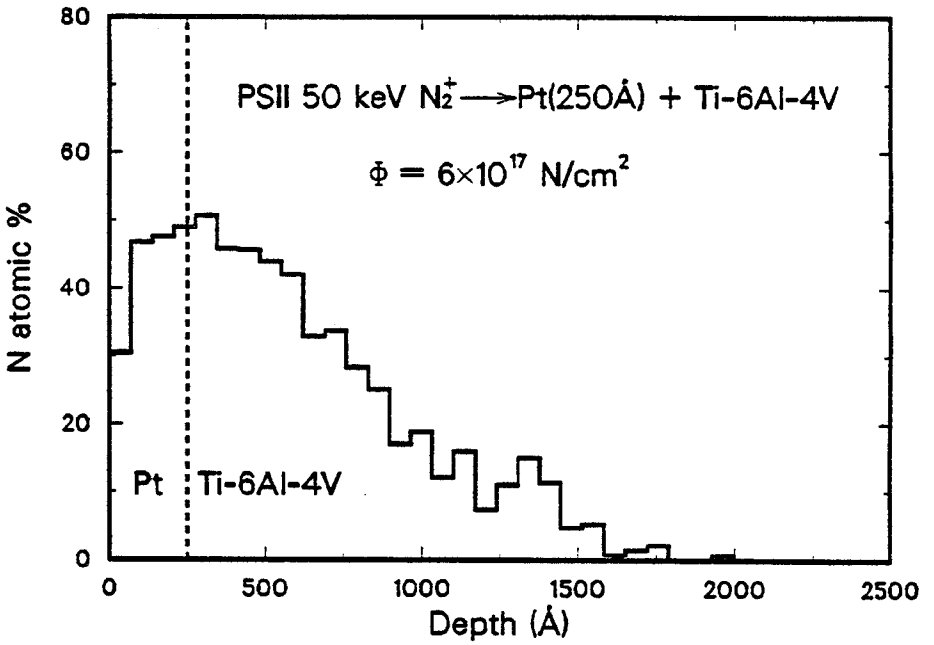

Figure 6.5: PSII-N distribution in a bilayer target

tion. Throughout the various test procedures, the PSII-modified samples have been proved to have same or even better materials properties with respect to those treated with conventional ion implantation. The major advantages of PSII come from the fact that it is not a line-of-sight process, which results in a uniformly implanted ion dose on the surface without the use of target manipulation equipment, no need for masking of the target to reduce the excessive sputtering by glancing incident ions, and the elimination of the ion accelerator stages along with a raster-scan apparatus to get uniform dose. In Fig. 6.5, the static simulation result with TAMIX is shown for an ion beam mixing geometry, where a 250 Å Pt layer was deposited on a Ti alloy(Ti-6Al-4V) and irradiated with the PSII-N plasma at the bias voltage of 50 keV up to the fluence of 6×10^{17} N atoms/cm^2. In the simulation dual ion energies were

used, that is, 75 % of the N ions had 25 keV energy and 25 % of the ions had 50 keV when striking the target surface. In the figure, it can be noted that the nitrogen peak position corresponds to the interface, but most of the implanted nitrogen reside in the Ti alloy substrate up to 2000 Å from the surface, which enables the improved mechanical properties via the formation of TiN. In the figure, it can also be noted that besides the major peak occurring at the interface from 25 keV N, there exists another small peak in the far deep region, which is from 50 keV N contribution. Because the static mode is used in this simulation, the sputtering of the surface and mixing between two layers are not considered, which may affect the final concentration profiles at this high ion fluence.

6.1.2 Sputtering

The light ion back-scattering from the fusion first wall material has been one of the issues related with the thermonuclear fusion research, hence there has been accumulation of experimental data for the back-scattering coefficients. Basically, the ion back-scattering is a collisional process, which can be simulated effectively with static mode TAMIX. In Fig. 6.6, the back-scattering coefficients of atomic species in fusion plasma are compared with experimental data [12,13,14,15,16] for various ion energies. The number reflection coefficient R_N and energy reflection coefficient R_E are defined respectively as

$$R_N \equiv \frac{\text{total number of reflected ions}}{\text{total number of incident ions}}$$

$$R_E \equiv \frac{\text{total energy carried by reflected ions}}{\text{total energy carried by incident ions}}$$

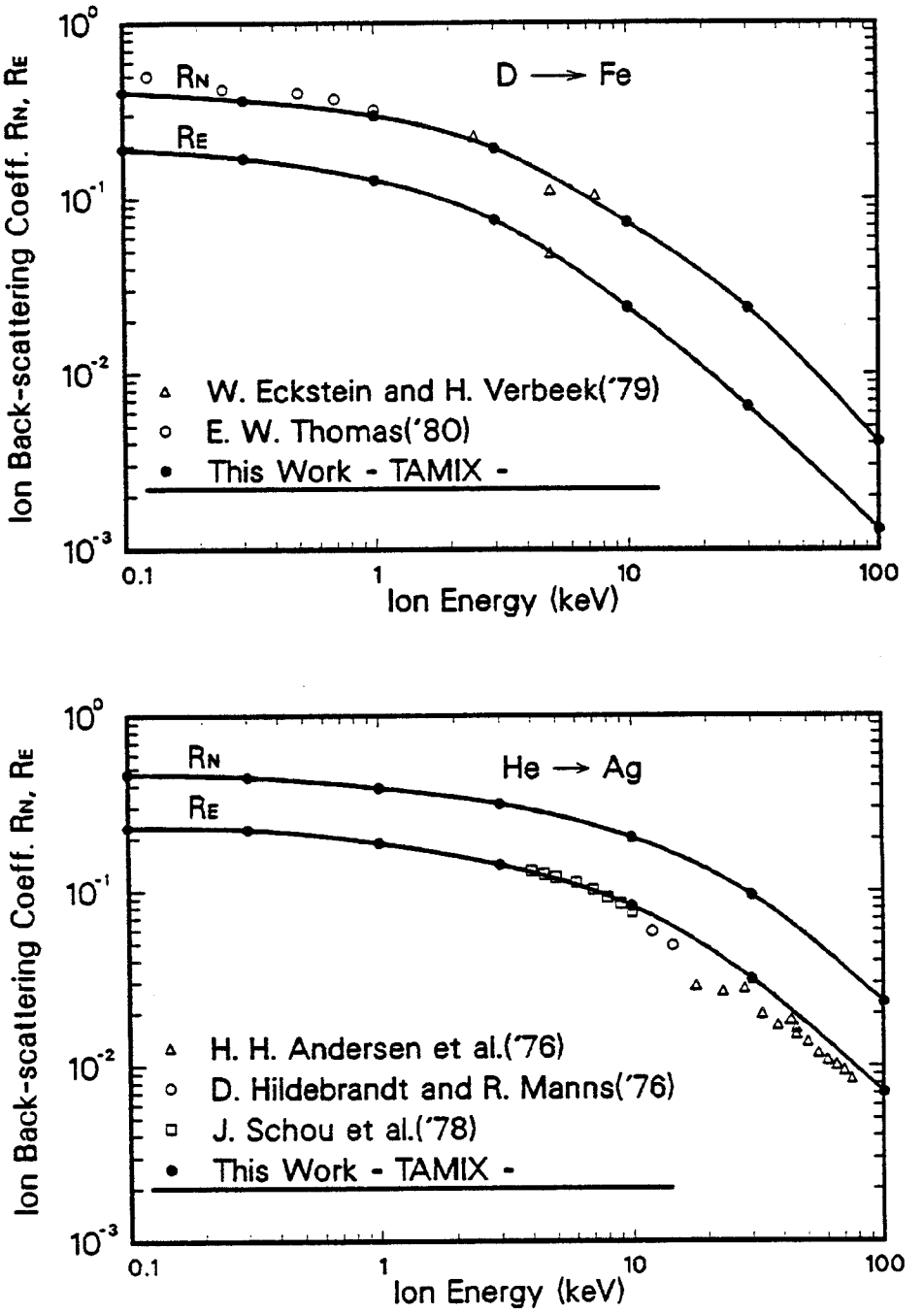

Figure 6.6: Light ion back-scattering coefficients, D on Fe and He on Ag

As seen in the figures, the predicted values from TAMIX show a good agreement with the experimental data. It is obvious that the reflection coefficients decrease with increasing ion energy due to the deep penetration of ions, which results in lower escape probability. Also, due to the energy loss of ions inside the solid the energy reflection coefficient R_E is always smaller than the number reflection coefficient R_N.

Because most of the sputtering by ion bombardment has been known to be a collisional process, it is a reasonable step to compare TAMIX sputtering results with experimental sputtering yields. Through Fig. 6.7 to 6.11 the calculated sputtering yields by TAMIX are shown along with the available experimental data. In the figures, the left axes is for heavy ions, the right axes is for light ions, and solid lines are just interconnections between TAMIX data points to guide eyes.

For Be in Fig. 6.7 the measured sputtering yields by Kr ion are higher more than a factor of 2 compared to the TAMIX results, especially at lower ion energies. Because Be is a strong oxide-forming material, the surface may be contaminated with oxygen. In general, the chemical sputtering plays an important role in the oxides in addition to the physical sputtering process. However, this kind of explanation should be applied the same to the He bombardment, which shows much better agreement with the experimental data even though the data are so scattered. Other possible explanation can be sought from a systematic error for the relatively old data [17,18], if we note that the old data give higher values than more recent ones by J. Roth et al. [19] for both Kr and He ions. Hence, more experimental data would be

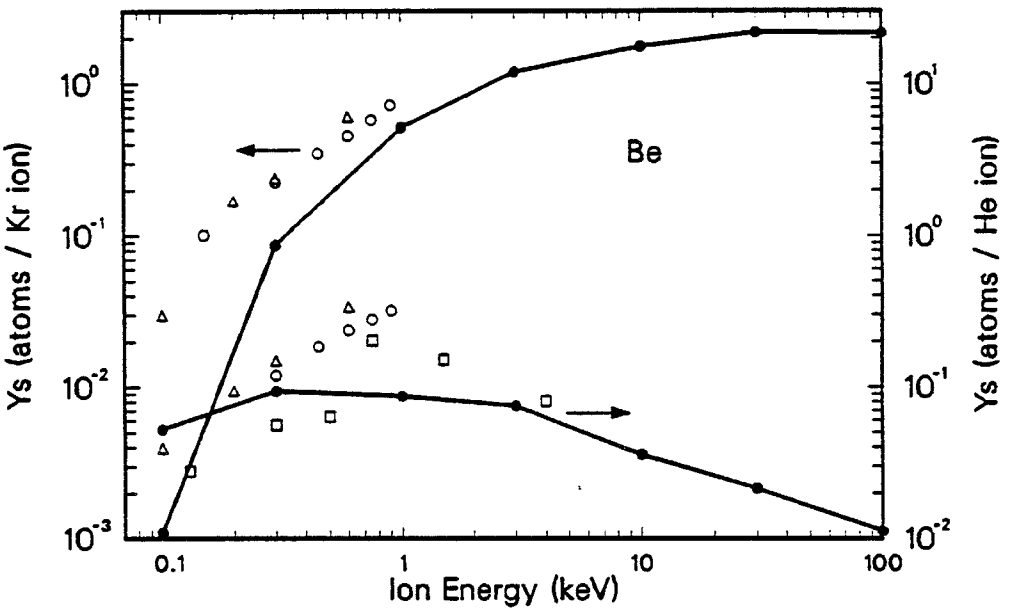

- △ D. Rosenberg & G. K. Wehner('62)
- ○ H. Fetz & H.Oechsner('63)
- □ J. Roth et al.('79)
- • This Work - TAMIX -

Figure 6.7: Sputtering yield of Kr and He on Be

highly demanded for Be.

For the Ni target in Fig. 6.8, the TAMIX code reproduced the experimental data for both heavy and light ions [20,21,17,18,22]. Also, for Mo [23,24,20,21, 25,26,27,28,29,30,31,32,33,34,35] in Fig. 6.9 the simulation results are quite satisfactory except for the overestimation of yield from D ions at low energies. For Au [20,17,36,37,38,39,33,40] the discrepancies can be explained with the same argument sought in the interpretation of the ion range data, i.e. the deviation from the average behavior of interatomic potential for Au. In Fig. 6.11, the sputtering yield of stainless steel which is a candidate for the fusion first wall materials is shown for the D bombardment and is given satisfactory agreement up to 6 keV [19].

According to Sigmund theory of sputtering [41], the dependence of the sputtering yield on the angle of incidence is given by $\frac{1}{\cos^f \theta}$ up to about the maximum in the yield($\theta_{max} \sim 60°$) and with $1 < f < 2$. It has been shown however, that the Sigmund theory can not be applied to light ion sputtering with low incident ion energy. The theory gives much larger values, being as much as one to several orders for ion energies lower than 10 keV [33]. In Fig. 6.12, TAMIX simulation results show the experimentally observed behavior. For Xe ions on a Ni target the angular dependence of the sputtering yields can be well fitted to Sigmund theory up to the angle of maximum yields($60 \sim 70°$). But, for the low energy He ion bombardment, the enhancement of yields by glancing angle of incidence is negligible. Also, in the figures, it can be noted that the angles of maximum yield are shifted to the higher values for He ion compared to Xe ion.

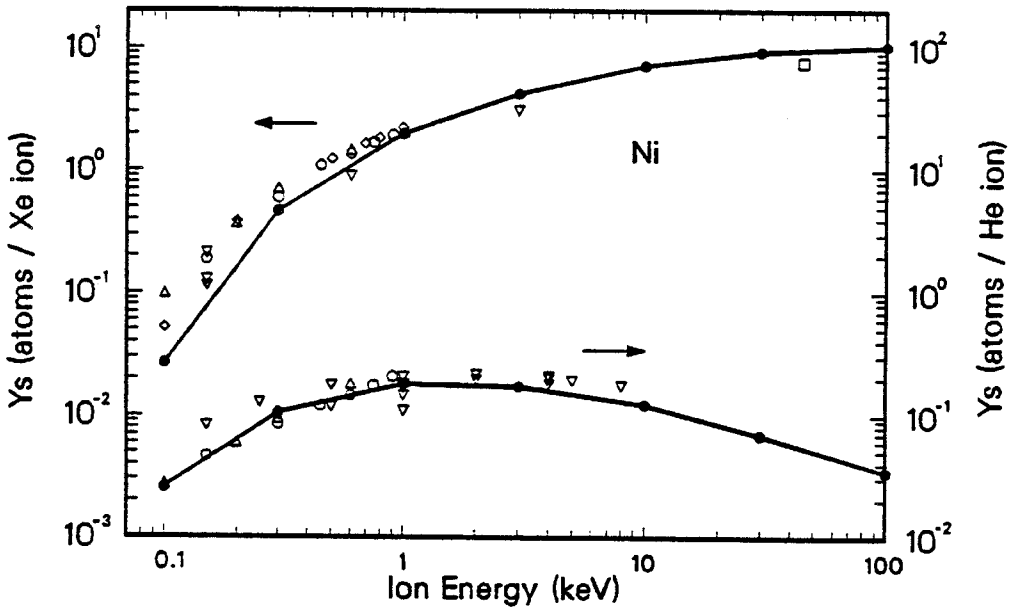

- O. Almen & G. Bruce('61)
- C. H. Weijsenfeld et al.('61)
- D. Rosenberg & G. K. Wehner('62)
- H. Fetz & H Oechsner('63)
- H. L. Bay et al.('79)
- This Work - TAMIX -

Figure 6.8: Sputtering yield of Xe and He on Ni

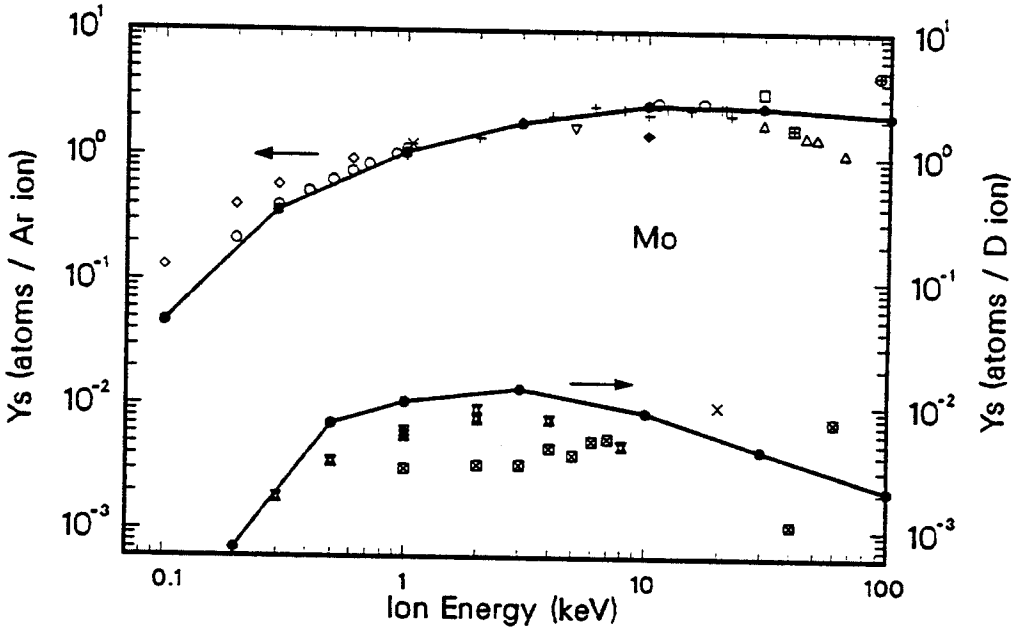

- O. C. Yonts et al.('60)
- N. Laegreid & G. K. Wehner('61)
- O. Almen & G. Bruce('61)
- C. H. Weijsenfeld et al.('61)
- H. Schirrwitz('62)
- B. M. Gurmin et al.('68)
- V. K. Koshkin et al.('69)
- O. C. Yonts('69)
- C. R. Finfgeld('70)
- H. Oechsner('71)
- G. Sletten & P. Knudsen('72)
- Z. E. Switkowski et al.('76)
- H. L. Bay et al.('77)
- B. Emmoth et al.('78)
- M. Kaminsky et al.('78)
- This Work -TAMIX -

Figure 6.9: Sputtering yield of Ar and D on Mo

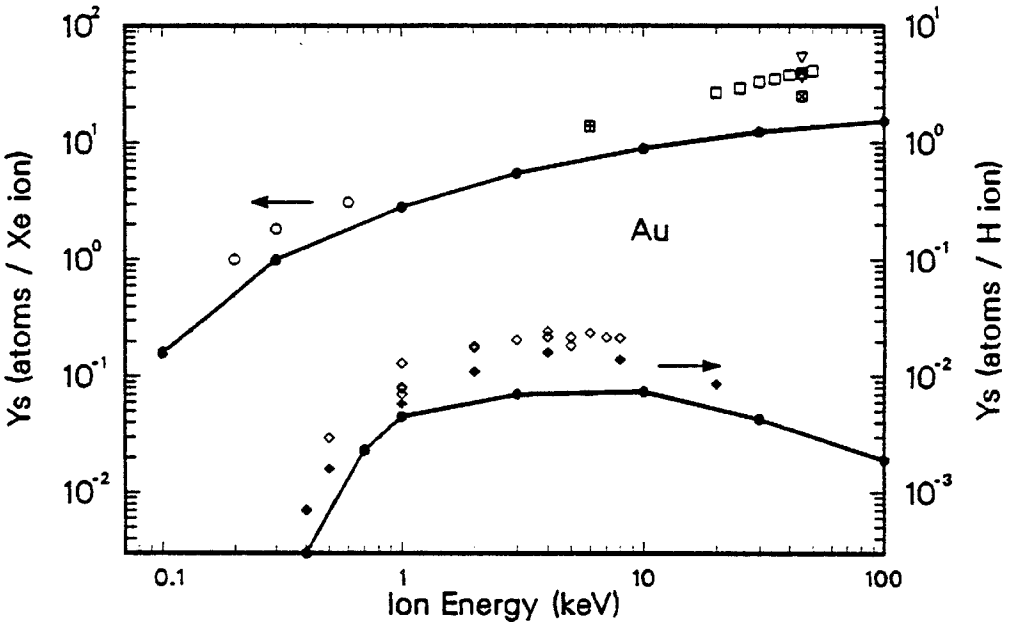

- △ O. Almen & G. Bruce('61)
- ○ D. Rosenberg & G. K. Wehner('62)
- □ T. Nenadovic & Z. Jurela('69)
- ◇ A. K. Furr & C. R. Finfgeld('70)
- ▽ H. H. Andersen & H. L. Bay('74)
- ◙ E. P. Eernisse('76)
- ◆ H. L. Bay et al.('77)
- ⊞ M. Szymonski('78)
- ● This Work - TAMIX -

Figure 6.10: Sputtering yield of Xe and H on Au

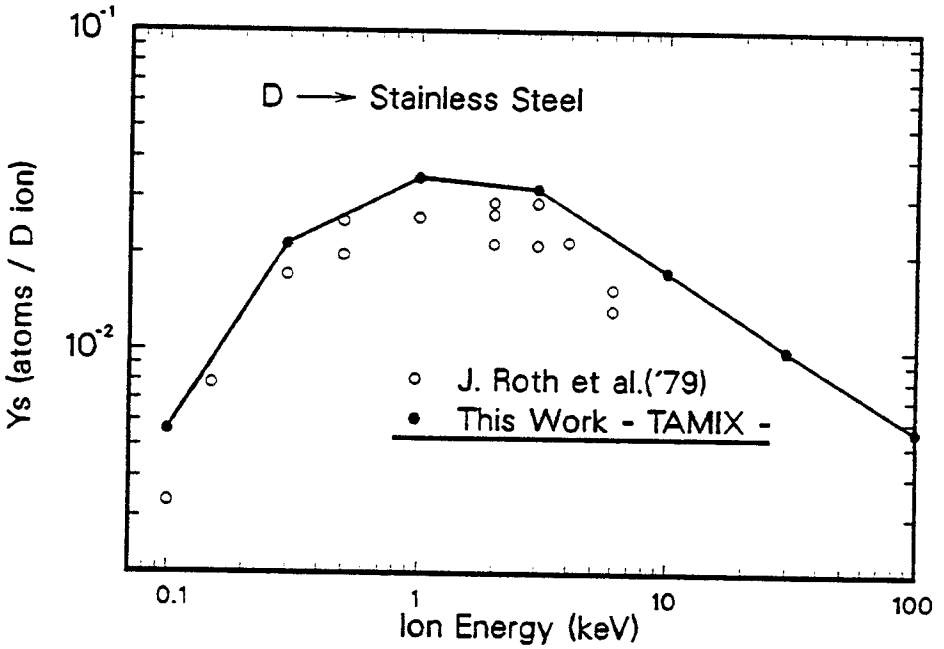

Figure 6.11: Sputtering yield of D on stainless steel

The sputtered atoms from a solid surface are ejected with a distribution in direction, which is described by a differential yield $\frac{d^2Y_s}{d\Omega^2}$. Using a linear cascade theory, Sigmund predicted the cosine angular distribution for the normal ion incidence. However, in the experiments it was found that at low ion energies the angular distributions are under-cosine becoming cosine-like and at higher energies they become over-cosine [42,43,44]. In Fig. 6.13, the angular distribution of sputtered atoms calculated from TAMIX are shown in polar plots for normal ion incidence. For Xe ion bombardment the transition from under-cosine to over-cosine with increasing energy is clearly seen. But, for He ions, a slight over-cosine can be observed even at the lowest energy of 0.1 keV. In Fig. 6.14, the angular distributions are shown for different incident angles for 1 keV Xe ion on Ni. It can be seen that the emission is mainly in the

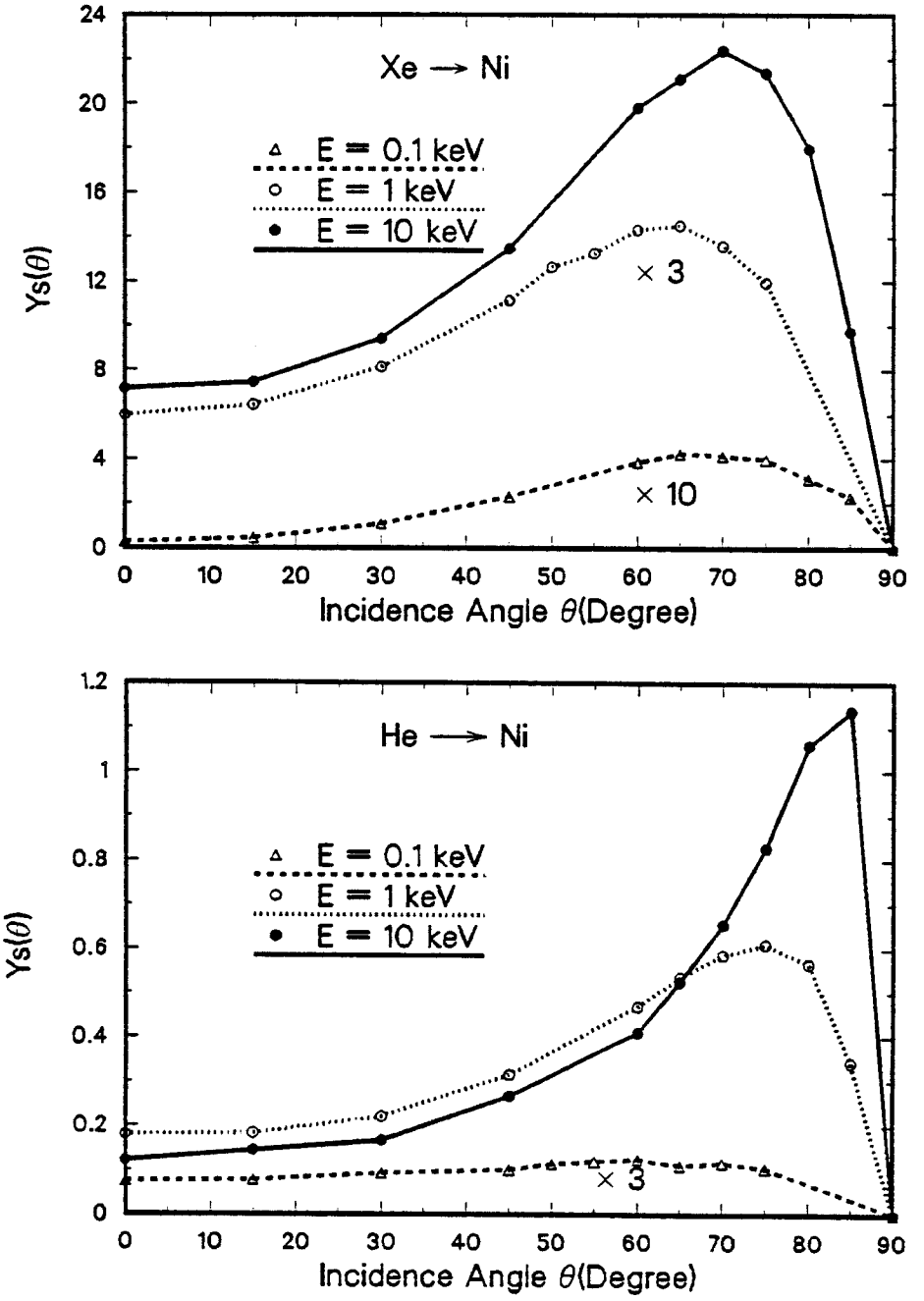

Figure 6.12: Incidence angle dependence of sputtering yield, Xe on Ni and He on Ni

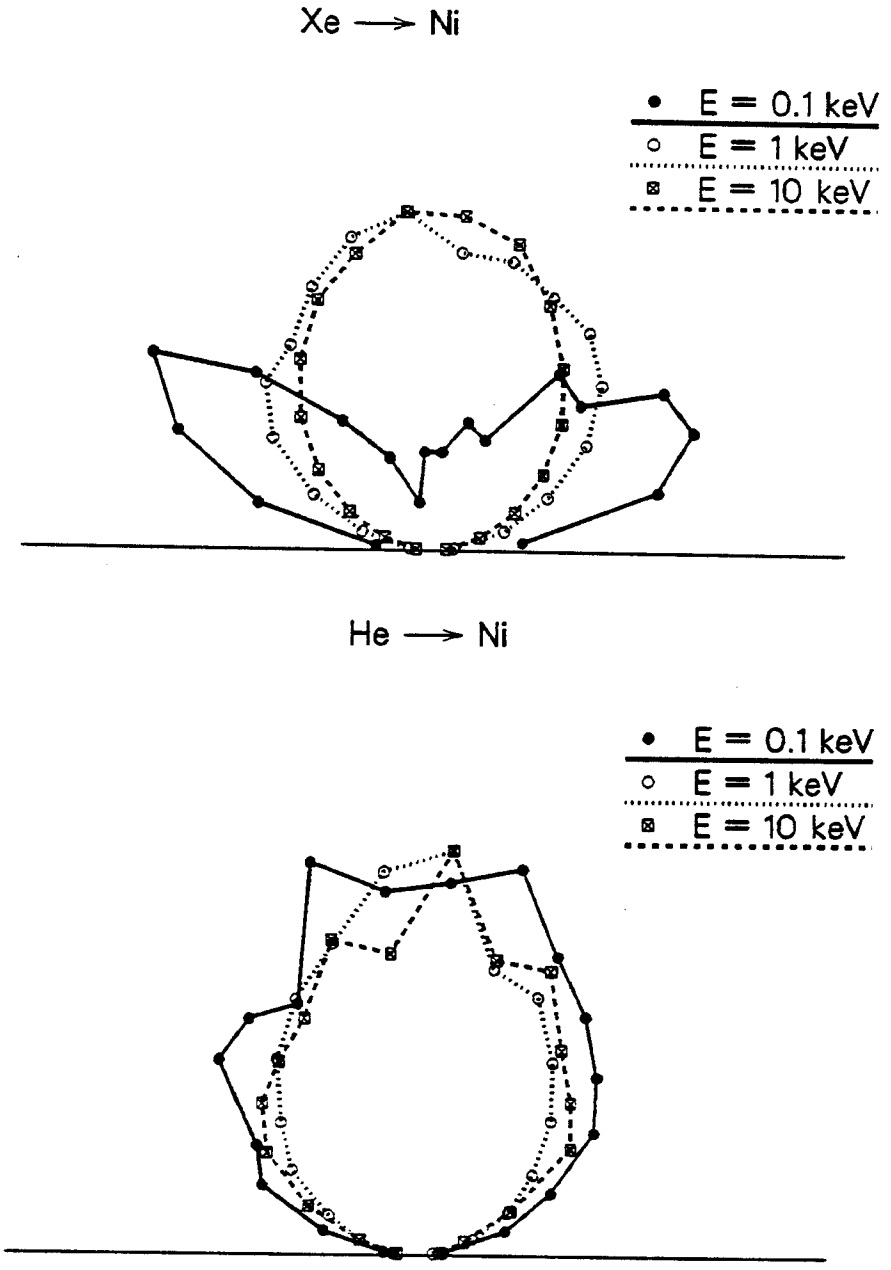

Figure 6.13: Angular distribution of sputtered atoms for normal ion incidence, Xe on Ni and He on Ni

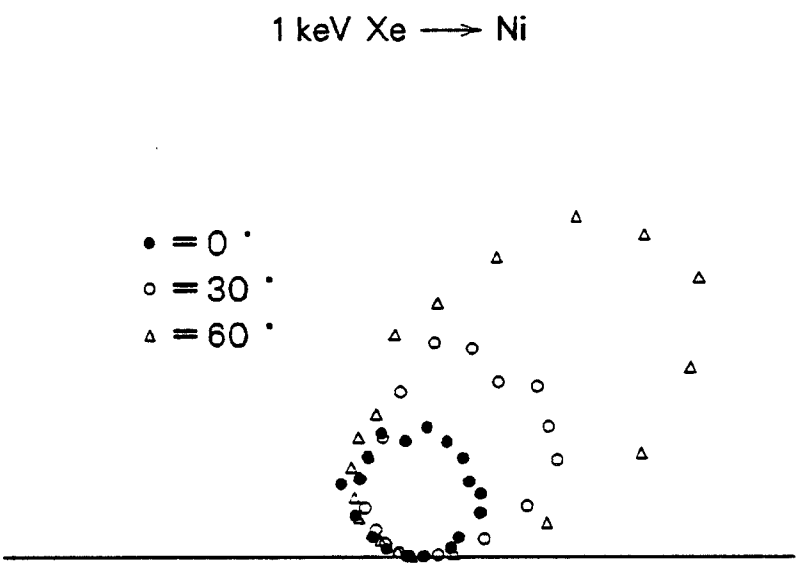

Figure 6.14: Angular distribution of sputtered atoms for glancing incidence, Xe on Ni

specular direction opposite to the incidence angle. The angular distribution of sputtered atoms are important in sputter-deposition technique for thin film production.

In addition to the angular distribution, the sputtered atoms are emitted with a distribution in energy. From sputtering theory the sputtered atoms are predicted to have maximum at the energy of $U/2$, where U is the surface binding energy and to have a $1/E^2$ tail for the sputtered atoms with higher energies. In Fig. 6.15, the energy distribution $\frac{dY_s}{dE}$ is shown from TAMIX calculation for Xe ion bombardment on Ni target with different energies. In the TAMIX code, the sublimation energy of the target is used as the surface binding energy(4.46 eV for Ni). Indeed, it is seen in the figure that the maximum occurs at $\sim U/2$ for ion energy of 10 keV, but it shows a slight shift

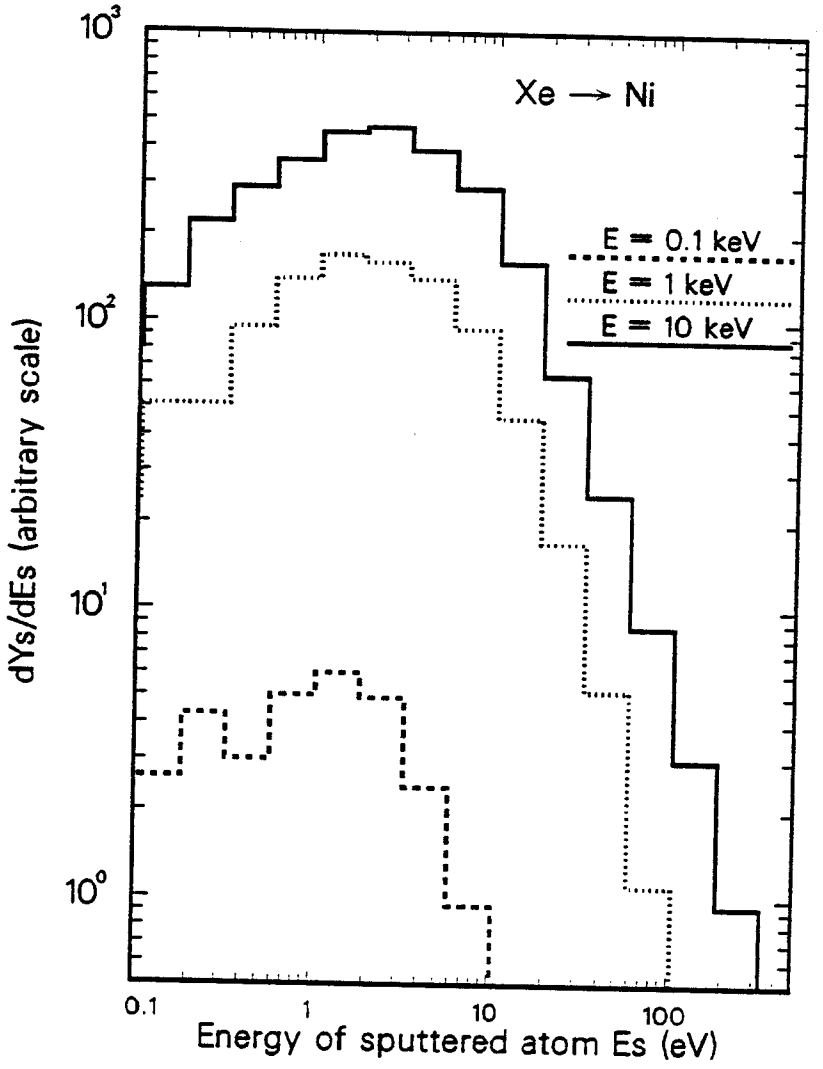

Figure 6.15: Energy distribution of sputtered atoms, Xe on Ni

to a lower values for lower ion energies. Furthermore, for all ion energies the distributions are seen to have $1/E^2$ tail at high energy region. In Fig. 6.16, the double differential yield $\frac{d^3Y_s}{dEd\Omega^2}$ is shown in a three dimensional plot for normal incidence of 1 keV Xe ion on Ni.

The grouping of recoils in TAMIX enables us to see which generations of recoils are contributing to the sputtered atoms. As discussed in the previous chapter, group $0(I_g = 0)$ corresponds to the ion, group $1(I_g = 1)$ is for the primary knock-on atoms, group $2(I_g = 1)$ is for the secondary knock-ons, and so on. From Fig. 6.17, it can be seen that for sputtering by light ions lower-indexed recoils dominates the sputtered flux. Due to the momentum of the incident ion, it is impossible for the primary-knock-on to be sputtered without the collision by back-scattered ions inside the target. Hence, for light ion sputtering the largest portion of the sputtered atoms comes from the collision with back-scattered ions. On the contrary, for Xe ion bombardment the middle-indexed recoils contribute more than either of the extremes.

In Fig. 6.18, the originated depth distribution of sputtered atoms is shown for Xe ion on Ni target at three different energies. From the constant slope of the curves it can be concluded that the origin depths are distributed exponentially, however with more contribution from deep-originated atoms for higher ion energies. It can also be seen that the most of the sputtered atoms($80 \sim 90$ %) are from a few atomic layers just beneath the surface. In the figure, the decrease of the sputtering yield from the first few Åthickness is due to 'random surface' model of TAMIX, in which the atomically rough surface was taken into account. This results in the reduction of the effective thickness of the first

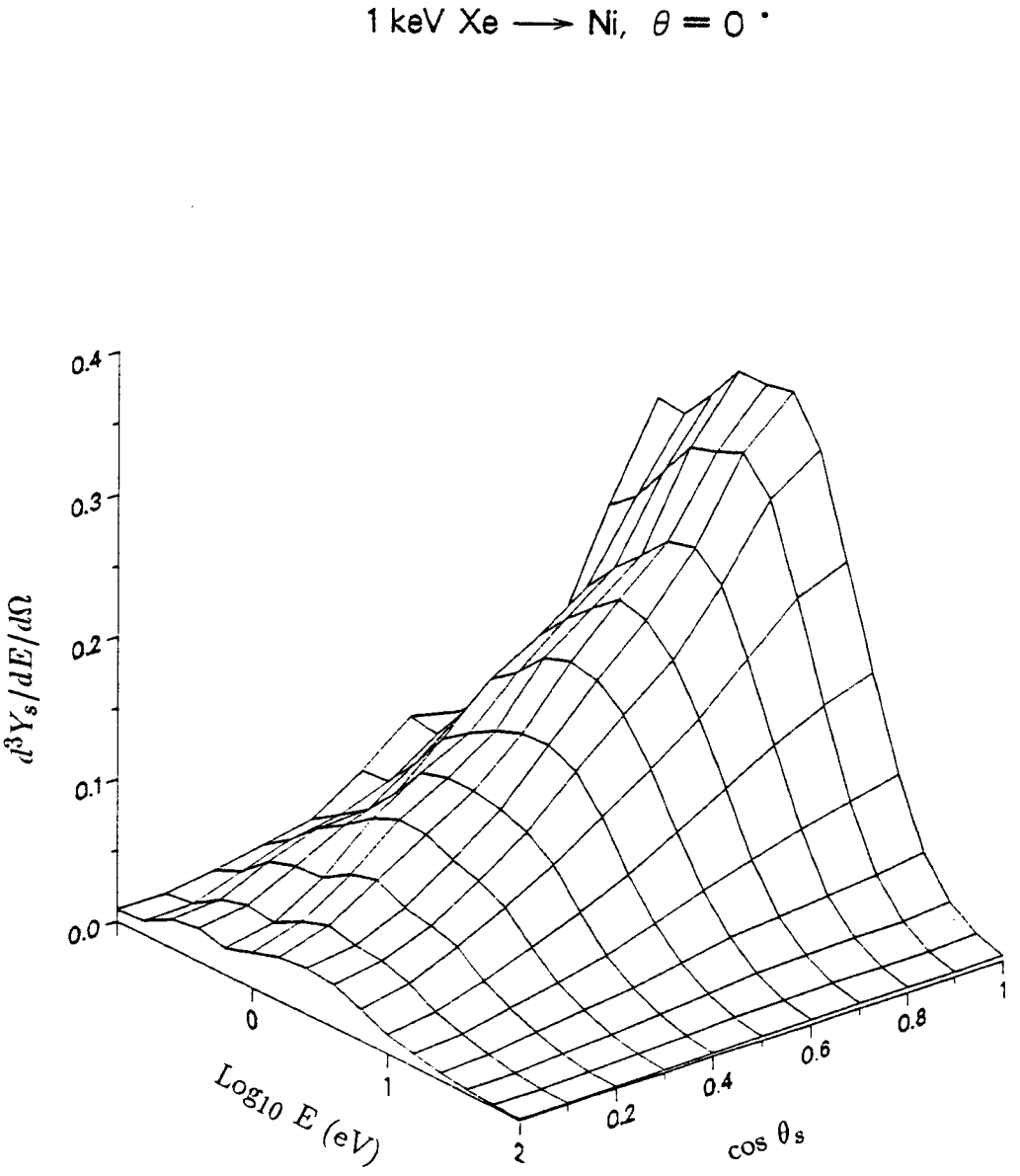

Figure 6.16: Double differential distribution of sputtered atoms, Xe on Ni

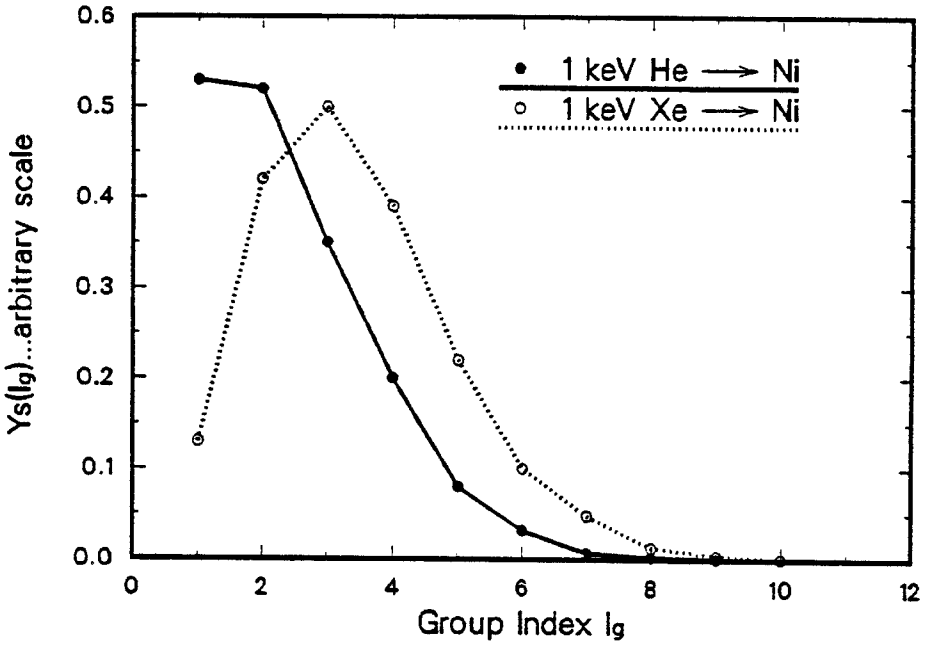

Figure 6.17: Group distribution of sputtered atoms, He on Ni and Xe on Ni

atomic layer by half of it, hence decreasing the contribution to the sputtered atoms.

6.2 Collisional dynamic mode

6.2.1 Preferential sputtering and altered layer formation

The dynamic change of the target due to the collisional processes during ion bombardment can be simulated with this simulation mode. The first thing which can be studied with this mode is the preferential sputtering of the initially uniform multicomponent target and the subsequent formation of the altered layer.

In Fig. 6.19, 6.20, and 6.21, the concentration profile evolution of an initially uniform Lu-Fe binary alloy bombarded with three different energy Ar

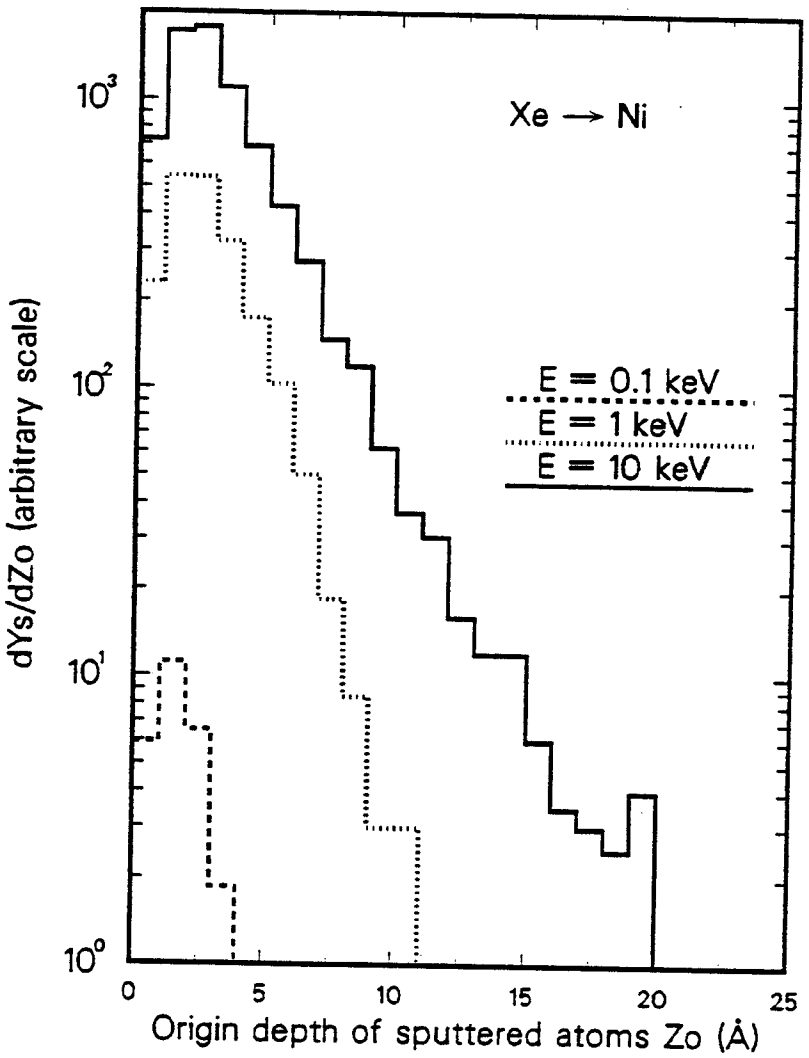

Figure 6.18: Origin depth distribution of sputtered atoms, Xe on Ni

ion is shown along with the partial sputtering yield of each component. The implanted Ar is also sputtered again by upcoming Ar ions, hence is shown, too. The depth is measured from the original surface to see the surface erosion due to sputtering. The first thing to note is the formation of the altered layer with thickness comparable to the maximum ion range. In general, the preferential sputtering is supposed to occur due to the difference of masses and surface binding energies of constituent elements. In Lu-Fe system, the mass effect is dominant because the sublimation energies of Lu and Fe are quite similar, 4.29 eV for Lu and 4.34 eV for Fe. However, the mass of Lu is more than 3 times heavier than Fe. Hence, the lighter Fe is preferentially sputtered, forming Lu-enriched region just underneath the surface. The other thing to note is the Fe-enrichment at the end of ion range, which is believed to be from the preferential recoil implantation of lighter Fe as predicted by Sigmund and Gras-Marti [45].

In the steady state, the mass conservation law states that the sputtered atoms must be removed stoichiometrically, i.e. with the same composition as the bulk. Indeed, the partial sputtering yields of Lu and Fe approach each other to give an equal values at the final ion fluence, 4×10^{16} /cm^2. The necessary Ar fluence to reach steady state is the lowest for 5 keV Ar, which is about 1×10^{16} /cm^2 compared to 2×10^{16} /cm^2 for 1 and 10 keV Ar. Normally, a material thickness comparable to the ion range should be removed to reach the steady state, therefore two factors must be determining the steady-state ion fluence, i.e. sputtering yield and range. If we examine the energy dependence of the range and sputtering yield, it is found that they have

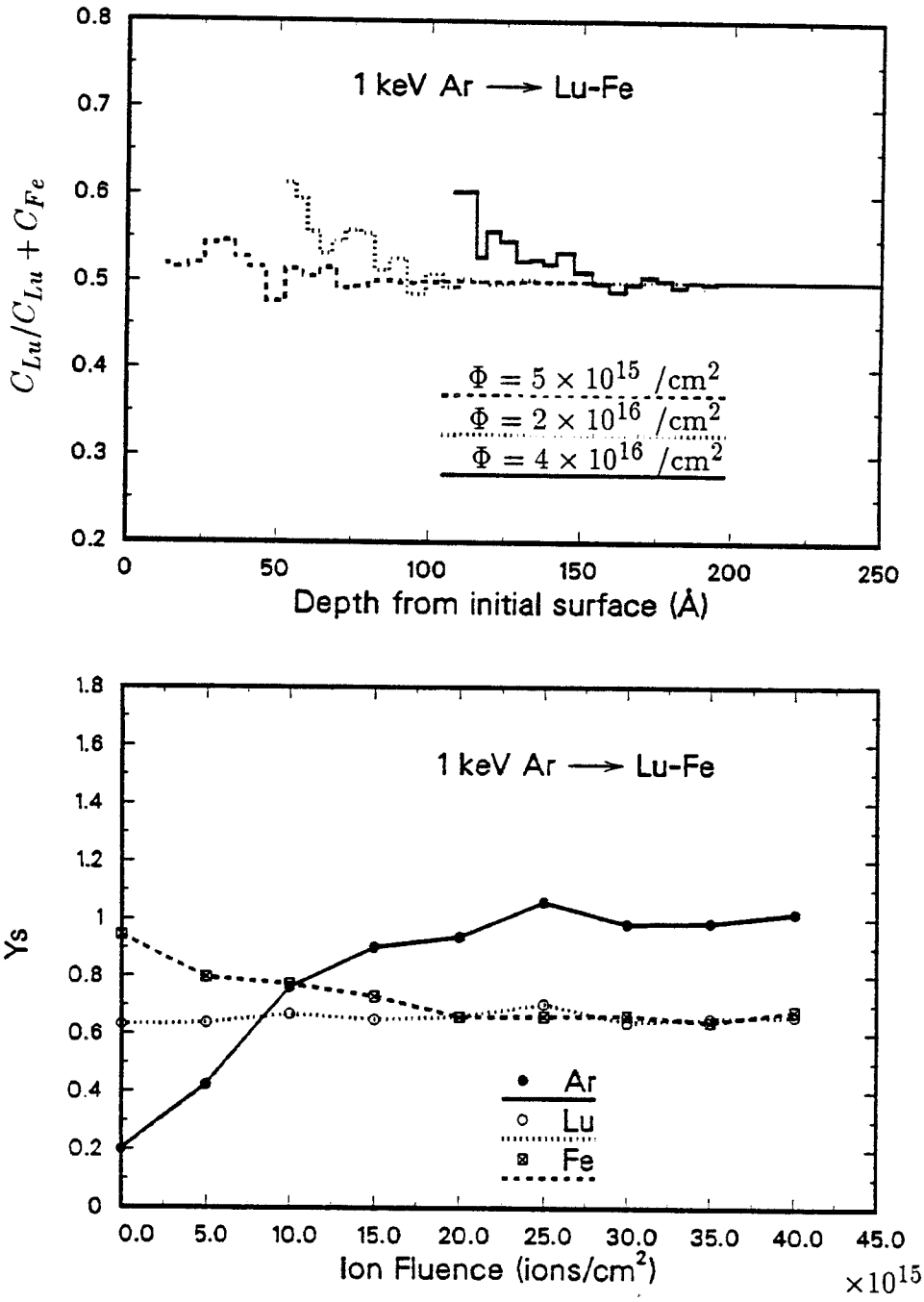

Figure 6.19: Dynamic composition change and instantaneous partial sputtering yield of Lu-Fe by 1 keV Ar irradiation

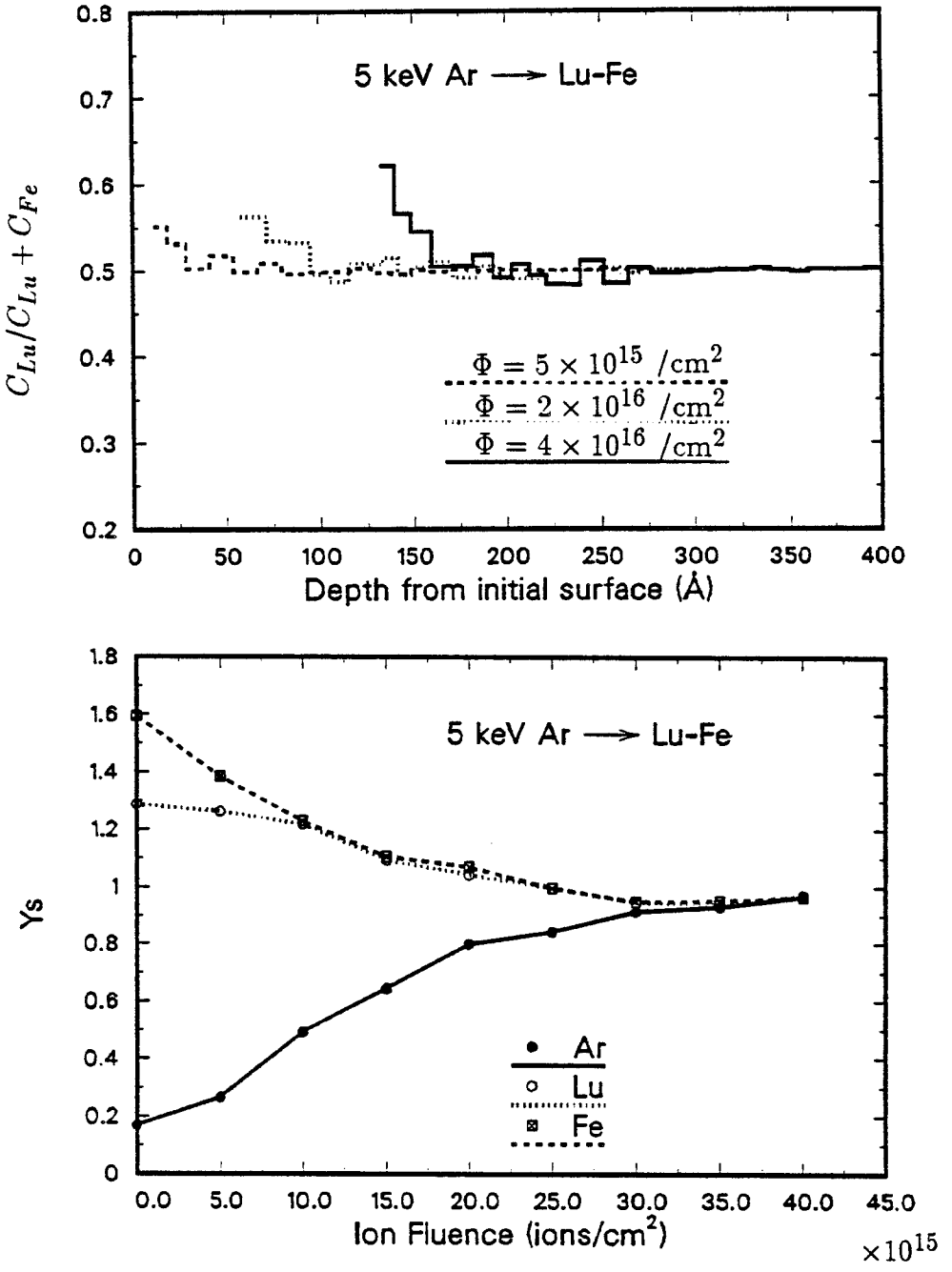

Figure 6.20: Dynamic composition change and instantaneous partial sputtering yield of Lu-Fe by 5 keV Ar irradiation

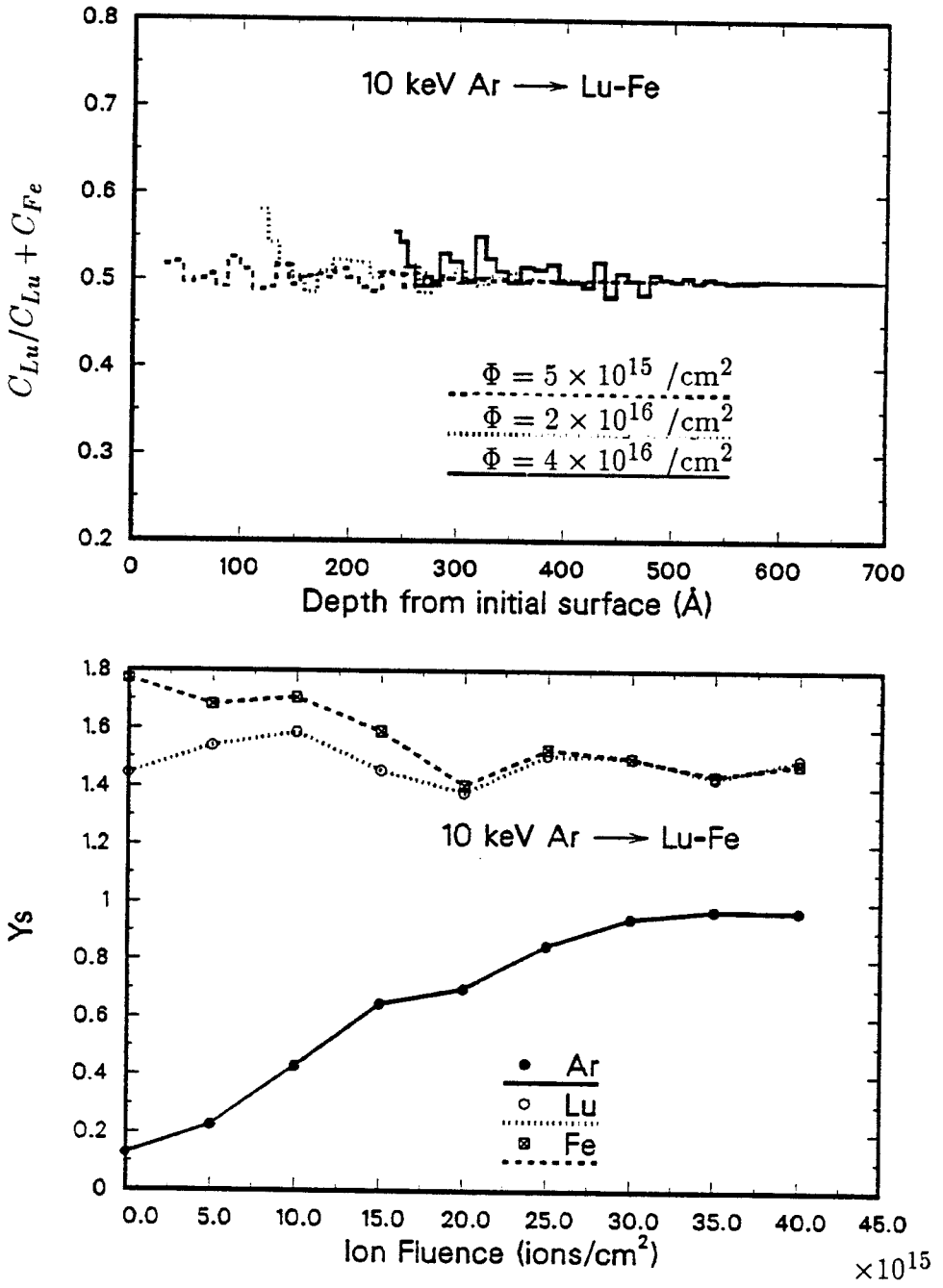

Figure 6.21: Dynamic composition change and instantaneous partial sputtering yield of Lu-Fe by 10 keV Ar irradiation

different sign of convexity even though both are increasing with increasing ion energy. In log-log plot, the sputtering yield curve is convex downward in contrast to the range curve which is linear or convex slightly upward. Because the required ion fluence to reach the steady state is proportional to the ratio of range to sputtering yield, it is easily concluded that there is an ion energy at which the steady state will be reached with a minimum amount of ion fluence.

For Ar sputtering yield, the conservation of mass does not apply because there is a net inflow of Ar atoms from outside. Hence, steady state should be defined differently for Ar, that is, in steady state the partial sputtering yield of Ar should be unity. In other words, beyond the steady state no more Ar can be implanted due to the self-sputtering, which is a major concentration-limiting factor in high dose ion implantation. From the figures, it can be seen that the necessary ion fluence to reach Ar-steady state increases with ion energy.

The effect of different binding energies of constituent elements can be seen in Fig. 6.22, where the TAMIX result is shown for 5 keV Ar bombardment on Pt-Au alloy. Pt and Au have similar mass numbers but rather different sublimation energies, i.e. 5.86 eV for Pt and 3.8 eV for Au. In the figure, the surface region is seen to be enriched with strongly bound Pt due to the preferential loss of less tightly bound Au.

6.2.2 Collisional mixing

Due to the collisional mixing processes during ion irradiation an initially sharp interface between different materials becomes broadened. In Fig. 6.23, the broadening of a thin Pt marker layer embedded in Si at the depth of

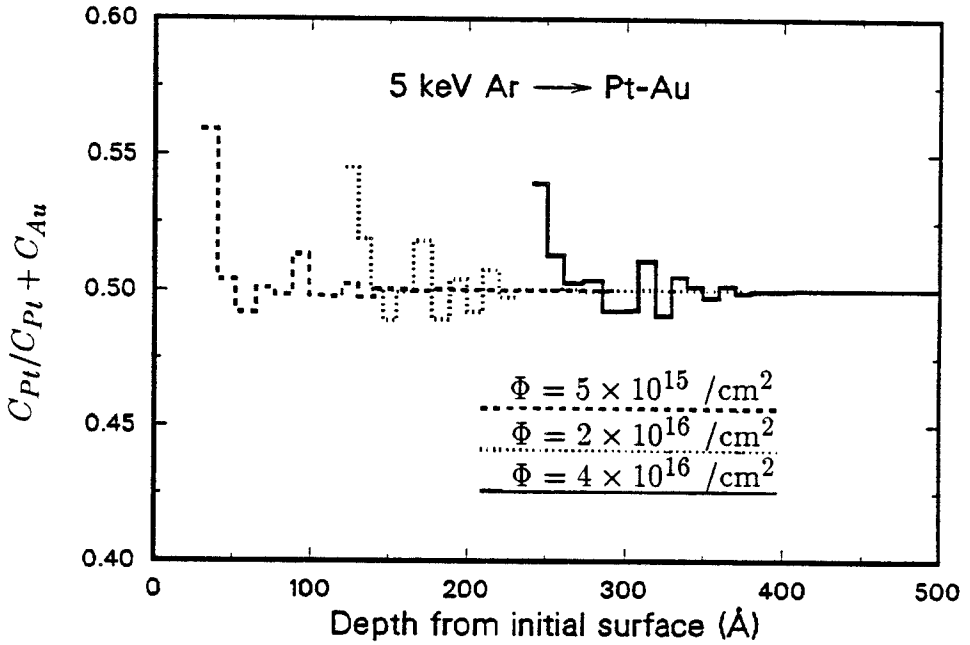

Figure 6.22: Dynamic composition change and instantaneous partial sputtering yield of Pt-Au by 5 keV Ar irradiation

500 Å was simulated with TAMIX for 300 keV Xe ion irradiation, which gives a projected range of about 1000 Å. Also shown are the experimental data [46] and analytic estimation from Sigmund and Gras-Marti [45]. Because the marker layer is so thin, it will soon be dispersed by ion irradiation, reducing the chemical effect to minimum. Hence, the marker system is often adopted to investigate the collisional mixing mechanisms. In the figure, it is obvious that the broadenings predicted from TAMIX and analytic theory are proportional to the square root of the ion fluence as found in the experiment. However, the magnitudes are quite different. The analytic theory gives the broadening about an order of smaller than the experiment. The TAMIX result is closer to the experiment, but still lower. The reason for the discrepancy between the

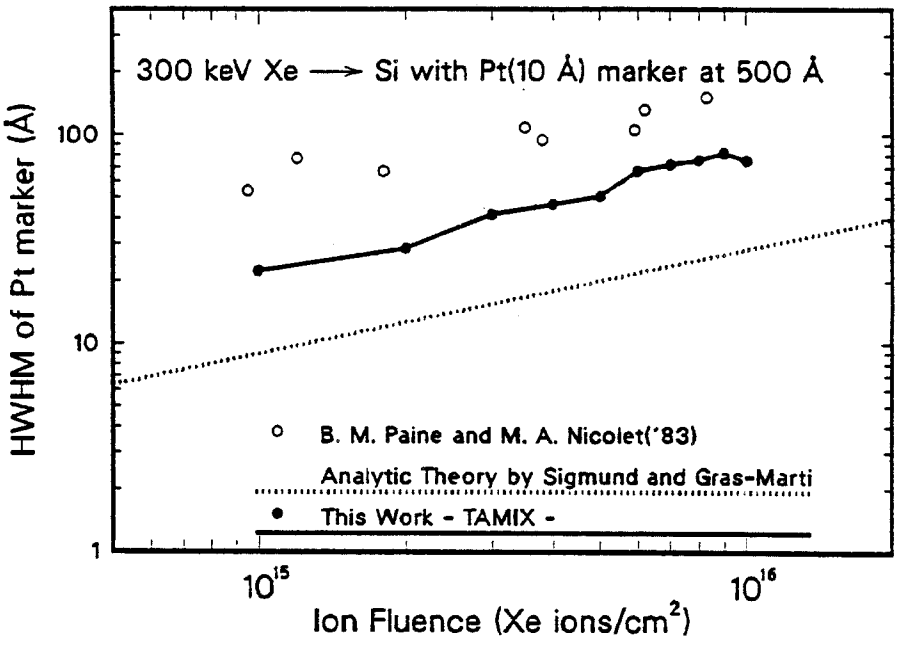

Figure 6.23: Broadening of Pt marker in Si by 300 keV Xe irradiation

TAMIX result and experiment is not clear at this time.

In Fig. 6.24, the collisional mixing of a bilayer was simulated with TAMIX. The target consists of a 250 Å Cu on Ni substrate and is irradiated with 50 keV Ar ions up to a fluence of 2×10^{16} /cm^2. The intermixing between two layers is obvious in the figure. Also, it can be seen that at the fluence of 1×10^{16} /cm^2 the substrate atoms are already seen on the surface.

The scanning AES is frequently used to obtain the concentration profile of a multicomponent target. Because some kind of heavy inert gas ions is used to sputter off the surface layer, it is often asked if there is further modification of the target by the working ions. It is because the scanning AES detects the composition on the surface region, which is rather sensitive to the ion bombardment. An attempt has been made to simulate the AES experimental

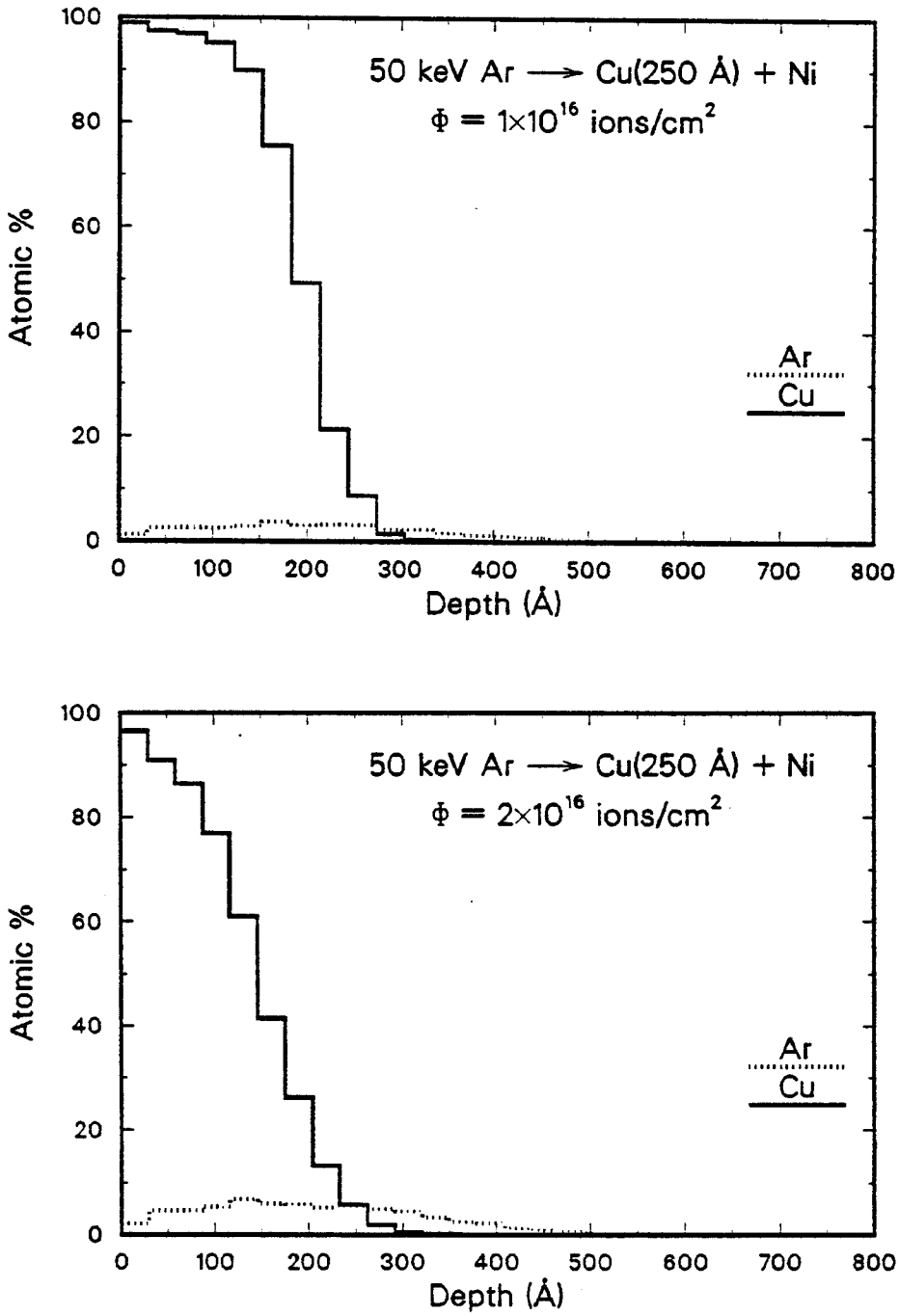

Figure 6.24: Collisional mixing of Cu + Ni by 50 keV Ar irradiation

situation with TAMIX. The original target was a Ti alloy(Ti-6Al-4V) with a 250 Å Pt layer deposited on it. In the upper part of Fig. 6.25, the calculated concentration profile is shown after 50 keV Ar irradiation with a fluence of 1×10^{16} /cm^2. The target is then irradiated with 5 keV Ar ions, which is a working ion to peel off the surface. During this subsequent irradiation the surface composition is recorded as a function of sputtered layer thickness just the same as in real scanning AES. The lower figure shows the result from this simulation. Comparing the two profiles, it is easily seen that both are quite similar except the longer tail of Pt and smoothened Ti profile accordingly, which is obviously a result of the surface modification by the working ions. Hence, it can be concluded that the scanning AES gives rather smoother profiles than the real one.

In the next few figures, a more complicated situation is simulated with the TAMIX code. In Fig. 6.26, the measured concentration profile by SIMS is shown for a Si target irradiated with PSII-CH_4 with a bias voltage of 50 keV [47]. Noting the Si-free surface region and a good possibility of floating carbon deposition during irradiation, an attempt was made to simulate the experiment with TAMIX for a sequential deposition of C layer on the irradiated surface. Fig. 6.27 shows the simulation result with a C deposition rate of 100 Åper every 2×10^{17} /cm^2 of total atomic fluence. In the simulation, multiple ion species and energy were used because the major species in CH_4 plasma is CH_4^+, which will break into a 37.5 keV C atom and four 3.13 keV H atoms upon striking the target surface. Also, it was assumed that there are small amounts of 25 keV and 50 keV H bombarding the surface, which are from

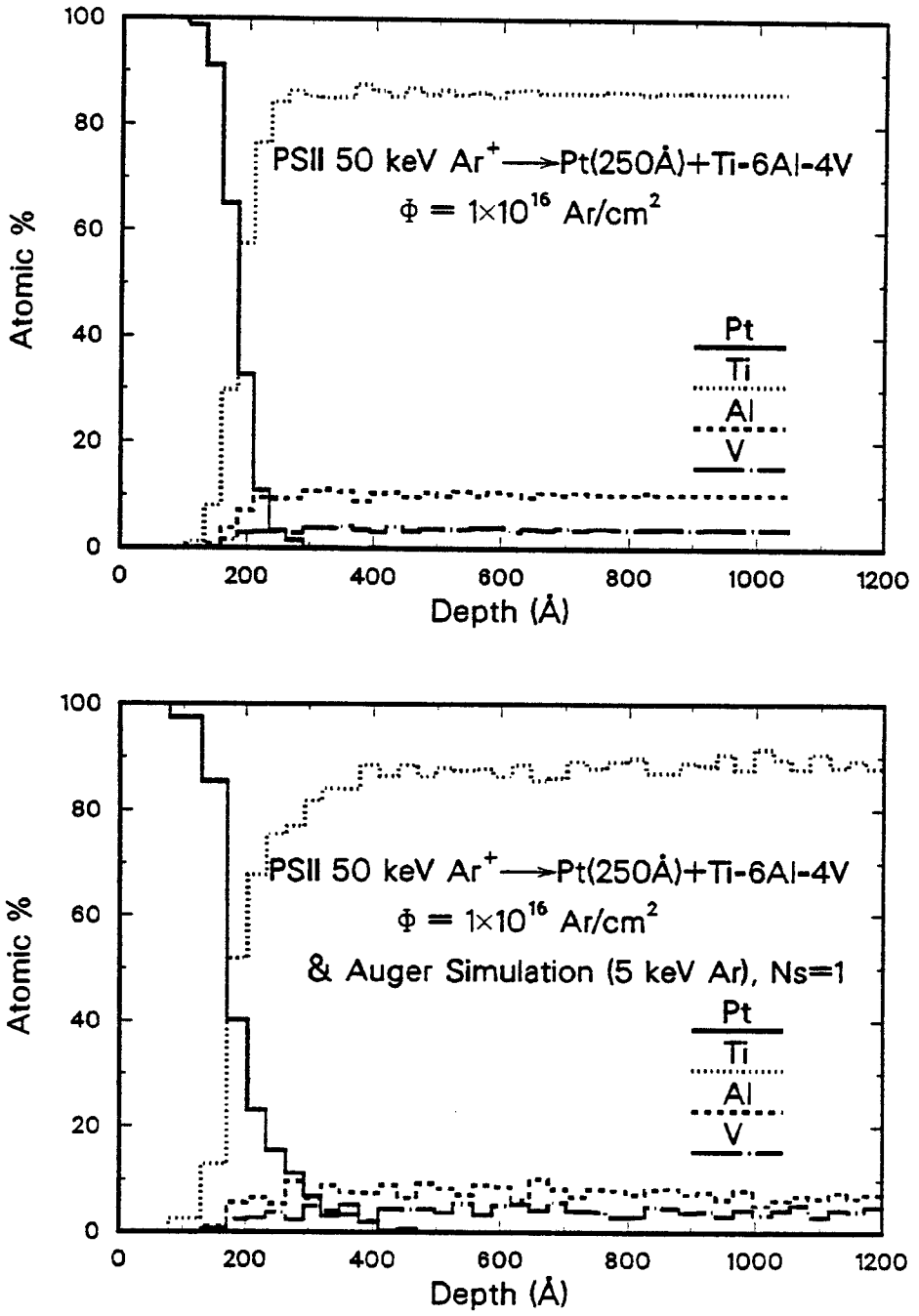

Figure 6.25: TAMIX simulation of scanning AES

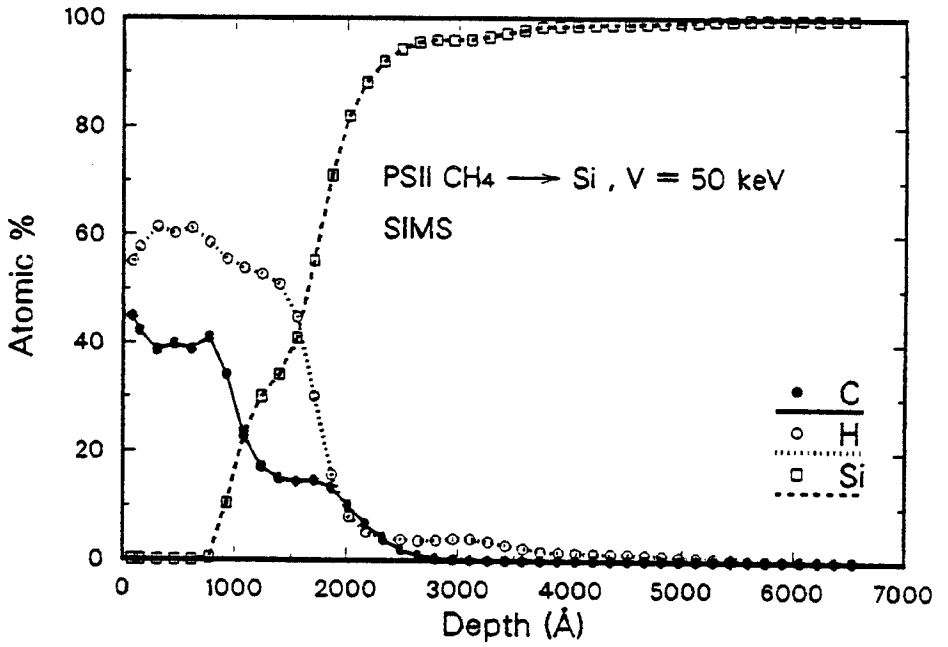

Figure 6.26: SIMS profile for PSII-CH_4 on Si

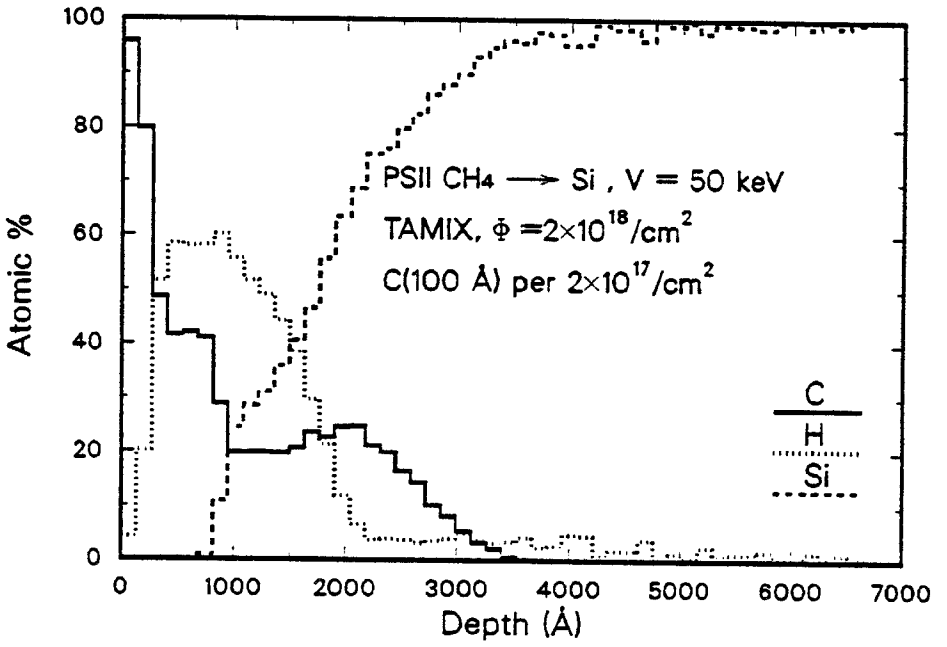

Figure 6.27: TAMIX simulation of PSII-CH_4 on Si

H^+ and H_2^+ ions in the system. The simulation result with a final fluence of 2×10^{18} /cm^2 shows a relatively good agreement with the experimental profile except minor variations. In Fig. 6.28, the simulation results are shown for different C deposition rates, none of which succeeded to reproduce the experimental profile. In order to check the effect of a finer sequential deposition but with the same net deposition rate, a simulation was performed using a deposition rate of 20 Å per every 4×10^{16} /cm^2, which gives the profile in Fig. 6.29 just the same as Fig. 6.27. The ability of the TAMIX code to simulate this kind of complicated situation is amply demonstrated in this section.

6.2.3 High dose ion implantation

As mentioned previously, in high dose ion implantation the self-sputtering of implanted species is a limiting factor to get enough concentration to modify the material. In Fig. 6.30, the retained N areal density resulting from PSII-N irradiation on Ti-6Al-4V target is shown as a function of ion fluence for three different ion energies. As seen in the figure, the retained N shows a saturation behavior with increasing ion fluence. Furthermore, the saturation level is higher for higher ion energy and is achieved at higher ion fluence.

6.3 Collisional and diffusional dynamic mode

Before actually attaching the diffusion part to the main body of the TAMIX code, the numerical solution of the diffusion equation was applied to a simpler geometry, i.e. a thin foil with a uniform irradiation such as in neutron irradiation from fast reactor. The system considered was Ni-25Cu homogeneous

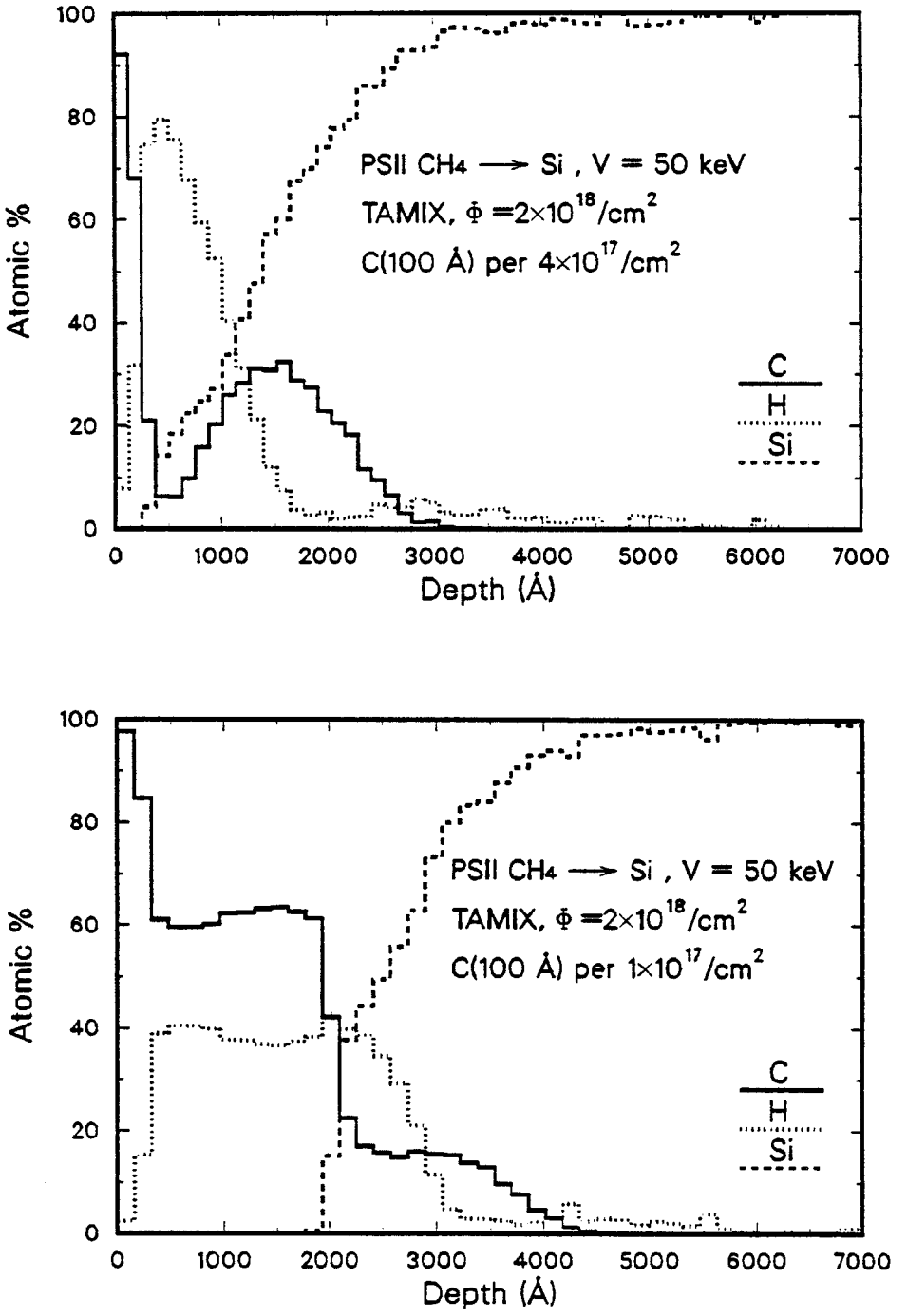

Figure 6.28: TAMIX simulation of PSII-CH_4 on Si

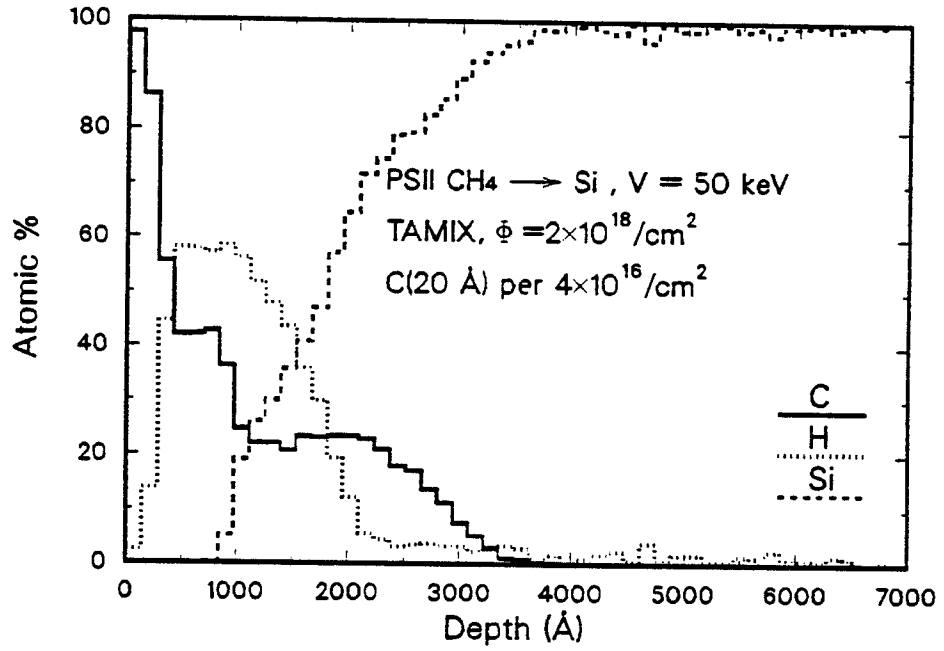

Figure 6.29: TAMIX simulation of PSII-CH_4 on Si

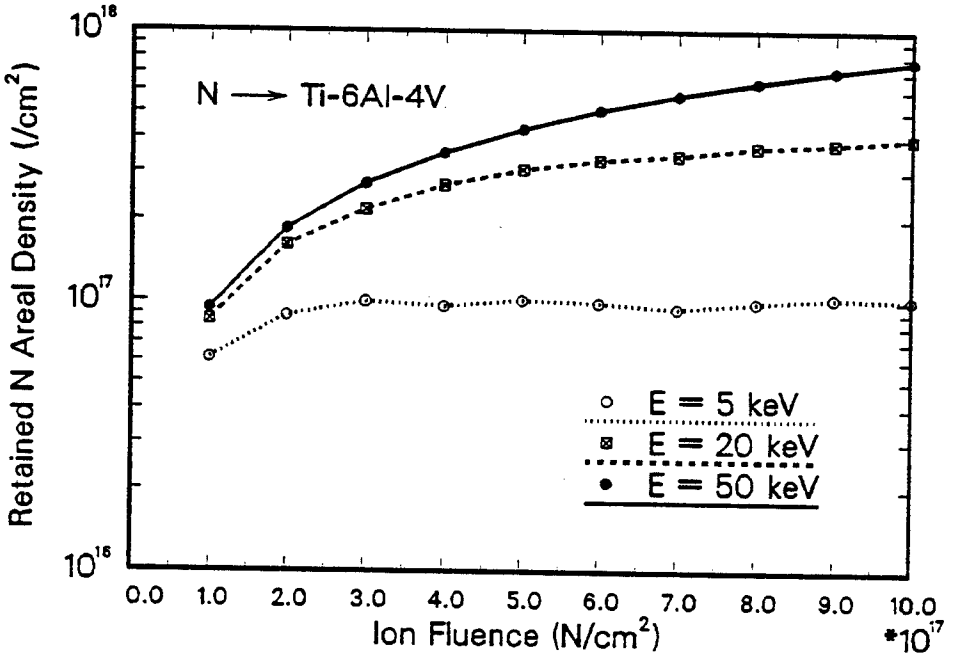

Figure 6.30: Areal density of retained N for PSII-N on Ti-6Al-4V

alloy. The first reason to choose this particular system is that its diffusion parameters are relatively well known compared to the other systems. Secondly, it forms a complete solid solution in entire composition range even though it shows a miscibility gap at lower temperature. Those parameters used in the calculation are summarized below.

$L = 5000$ Å

$C^o_{Cu} = 25$ %

$K_o = 10^{-3}$ /sec

$\rho_d = 10^8$ /cm^2

$R_o = 6$ Å

$Z = 12$

$\lambda = 3.55$ Å

$\nu_v = 5 \times 10^{12}$ /sec	$\nu_i = 5 \times 10^{13}$ /sec
$E^f_v = 4.0$ eV	$E^f_i = 1.6$ eV
$S^f_v = 3$ k	$S^f_i = 0$ k
$E^m_{v,Cu} = 0.95$ eV [48]	$E^m_{i,Cu} = 0.10$ eV
$E^m_{v,Ni} = 1.10$ eV [49]	$E^m_{i,Ni} = 0.15$ eV

The notations used in this section are the same and will not be repeated here except to note that L is the foil thickness, C^o_{Cu} is the initial Cu concentration, and the K_o value of 10^{-3} /sec is typical for ion irradiation. The calculations were performed at three different temperatures, at 200 °C, 500 °C, and 800 °C. From Fig. 6.31 to Fig. 6.33, the time-developments of the Cu concentra-

tion profiles are shown along with the vacancy and interstitial concentration profiles.

The first thing to note is a strong segregation behavior of the constituent elements at an intermediate temperature of 500 °C. The surface region is gradually depleted with Cu up to a few hundreds Å thickness, reaching a steady state at $t = 10^4$ sec. The reason for the strong segregation can be understood from the coupling between defect and atomic fluxes, as modeled in the diffusion equation. At this temperature, the point defects are mobile and they develop a concentration gradient because the foil surface is assumed to be an infinite sink to the point defects. Furthermore, these defect fluxes are coupled to the constituent atomic species, which will cause atomic transport. If the tendency of an atomic species to be coupled with a specific defect flux is different from that of the other species, then there will be a net increase or decrease of a particular element in that region. This atomic transport will continue until it builds up an enough atomic concentration gradient to back-diffuse, where the steady state will be achieved. In the present system, all of the parameters are set to be equal for both elements except the energies of motion of the defects associated with each element. Because the atomic species moves in the opposite direction to the vacancy in contrast to the interstitial, the segregation behavior can easily be predicted with the difference between the energies of motion of vacancy and interstitial for each element. Indeed, Wiedersich et al. [50] have shown that the element A becomes enriched at sinks if

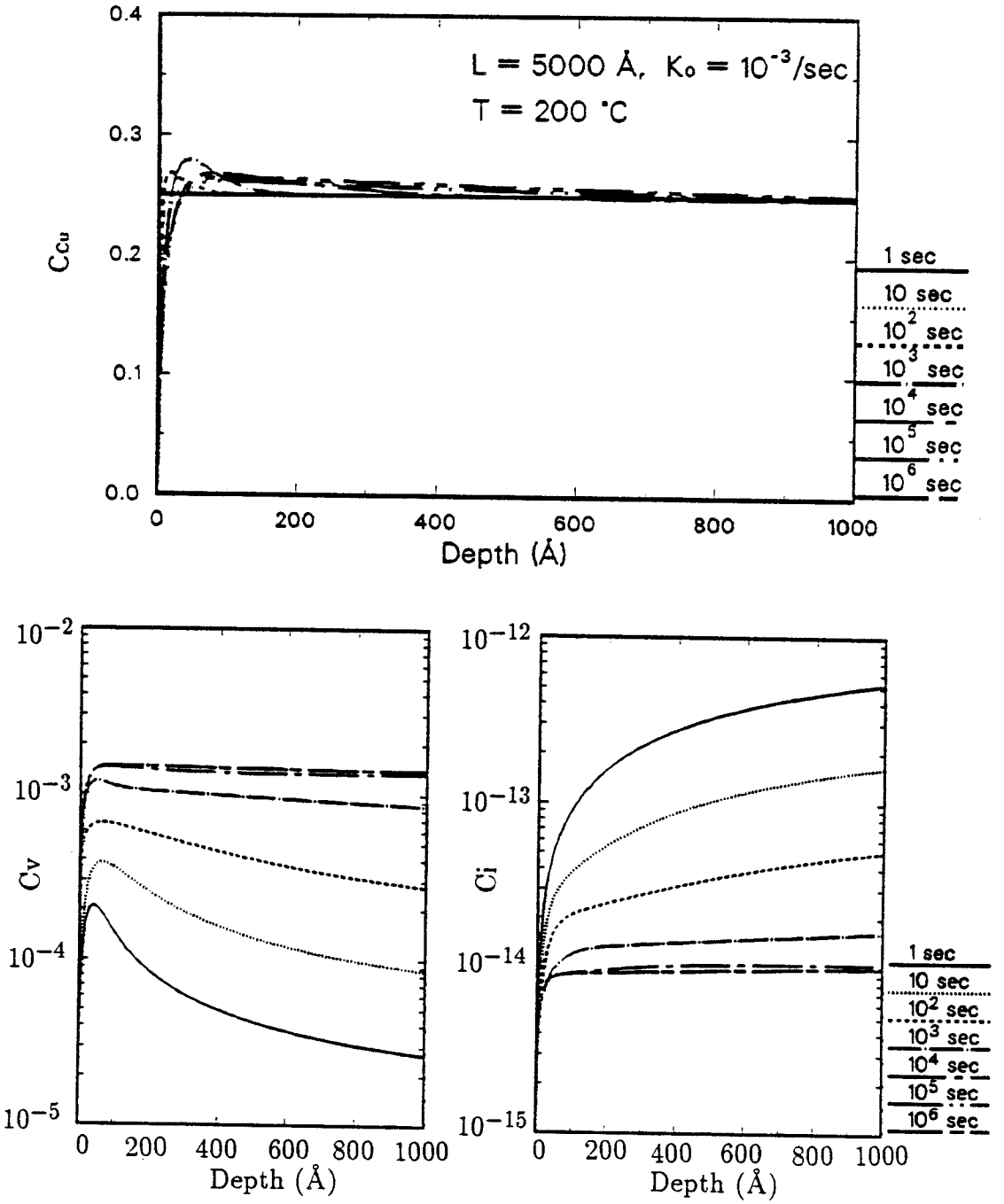

Figure 6.31: Profile evolution for a uniform irradiation on a foil, T= 200 °C

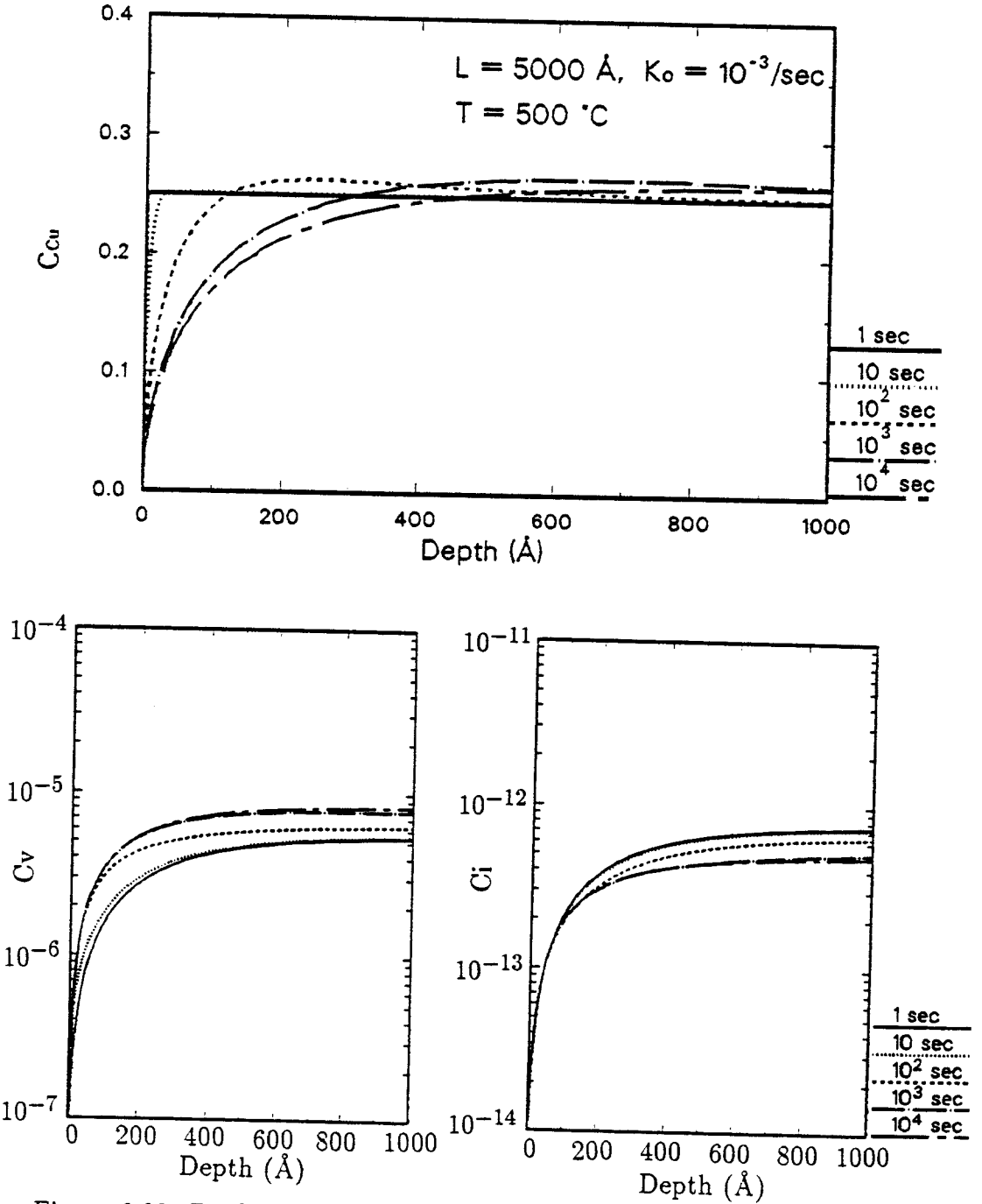

Figure 6.32: Profile evolution for a uniform irradiation on a foil, T= 500 °C

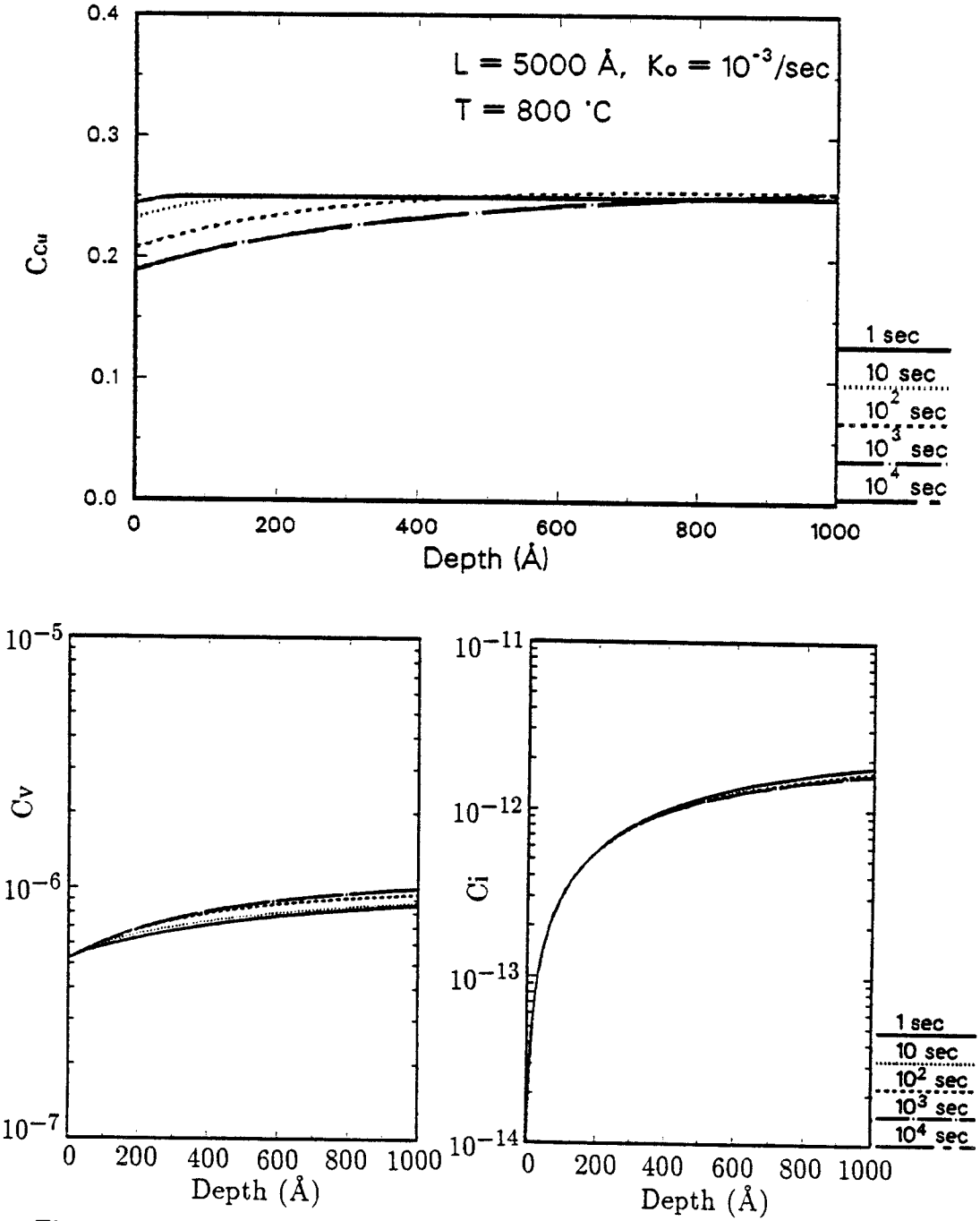

Figure 6.33: Profile evolution for a uniform irradiation on a foil, T= 800 °C

$$\frac{d_{iA}}{d_{ib}} > \frac{d_{vA}}{d_{vB}} \tag{6.1}$$

, where d_{iA}, d_{iB}, d_{vA}, and d_{vB} are the partial diffusivities of each element associated with each defect. If all of the parameters which determine the partial diffusivities remain the same for both elements, then eq.(6.1) will be

$$E^m_{vA} - E^m_{iA} > E^m_{vB} - E^m_{iB} \tag{6.2}$$

In the Cu-Ni system

$$E^m_{v,Cu} - E^m_{i,Cu} = 0.95 - 0.1 = 0.85 \text{ eV}$$

$$E^m_{v,Ni} - E^m_{i,Ni} = 1.1 - 0.15 = 0.95 \text{ eV}$$

, hence it can be predicted that Ni will be enriched at the surface with the depletion of Cu, which is confirmed in the present calculation.

At higher temperature of 800 °C, the defects are extremely mobile, which gives higher effective diffusion coefficients of the atomic species. Consequently, the steady state can be achieved with a lower atomic concentration gradient, which results in the reduced segregation and the solid becomes uniform again as in Fig. 6.33. At lower temperature of 200 °C, the vacancies are essentially immobile and the vacancy concentration becomes large. At steady state, most of the interstitials recombine with vacancies rather than diffuse to the surface, therefore segregation is reduced again. However, before reaching the steady state, the transient segregation is observed in Fig. 6.31, during which a shallow depth of the surface region becomes depleted with Cu. This transient behavior was seen to be disappeared eventually in the figure. Also, it can be noted that at lower temperature the atomic transport is quite slow, which gives a longer time to reach a steady state.

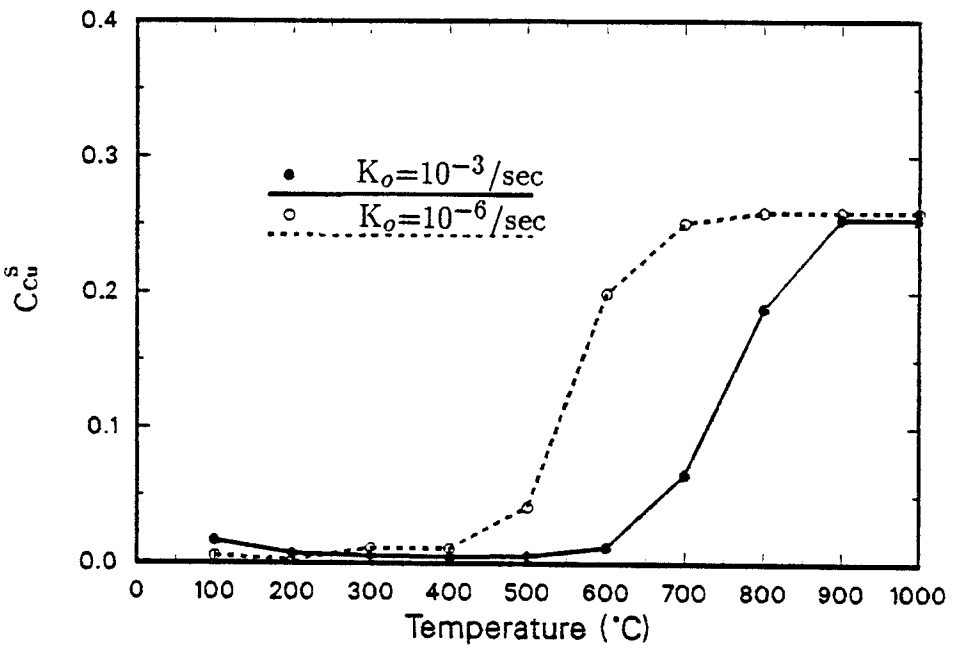

Figure 6.34: Temperature dependence of radiation induced segregation

In Fig. 6.34, the surface concentration of Cu at steady state is shown as a function of temperature for two K_o values. It can be seen that for lower defect production rate the segregation curve has been shifted to lower temperatures, which can be explained by the reduced defect concentration associated with lower value of K_o. One thing should be mentioned about the 100 °C data point, that is, because such a long time was taken to reach a steady state, the calculation was terminated at $t = 10^6$ sec. Actually, in the steady state they will have higher values than those in the figure. To see the effect of some of the input variables, two examples are shown, one for a different dislocation density and the other for a higher $E^m_{v,Cu}$. All the other parameters remain the same. In Fig. 6.35 it can easily be seen that the concentration profile development is quite different, that is the transient segregation at low temperature is more

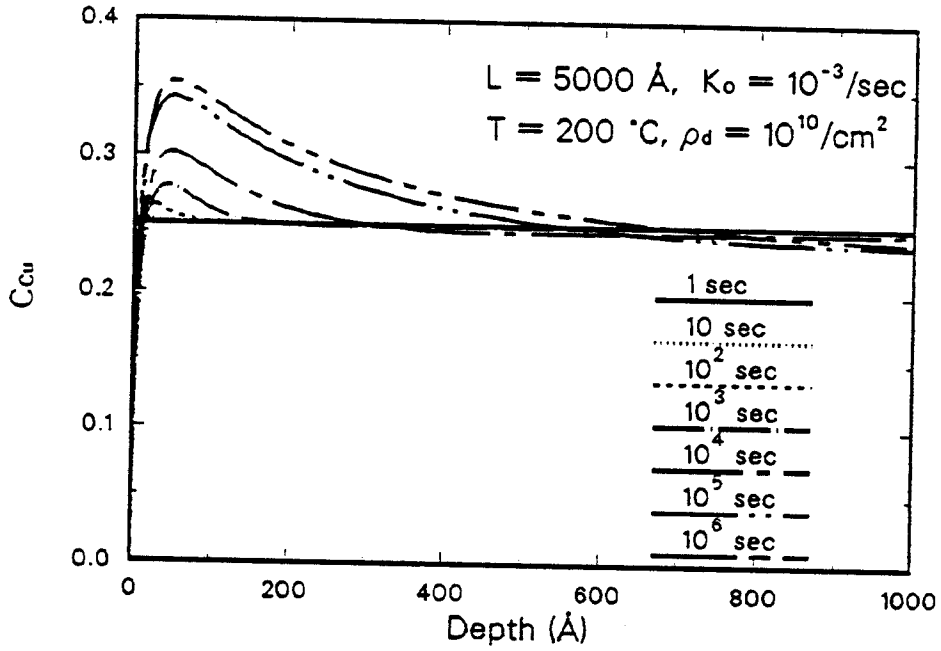

Figure 6.35: Profile evolution for a uniform irradiation with $\rho_d = 10^{10}$ /cm^2, at 200 °C

significant and lasts even at longer times. The reason for this is that the higher vacancy concentration gradient caused by the increased internal sink density gives the increased vacancy flux from the subsurface region to the bulk, which in turn results in the associated Cu flux from bulk to the subsurface region. In Fig. 6.36, the reduced segregation for increased $E^m_{v,Cu}$ can be understood from eq.(6.2) that the difference is more important than the absolute magnitudes to determine the segregation behavior. It has been seen in these examples that the diffusional process is quite sensitive to the choice of the values for involved parameters, most of which are not well known unfortunately.

In the next few figures, some of the TAMIX simulation results are shown, in which the diffusional processes were taken into account. In Fig. 6.37,

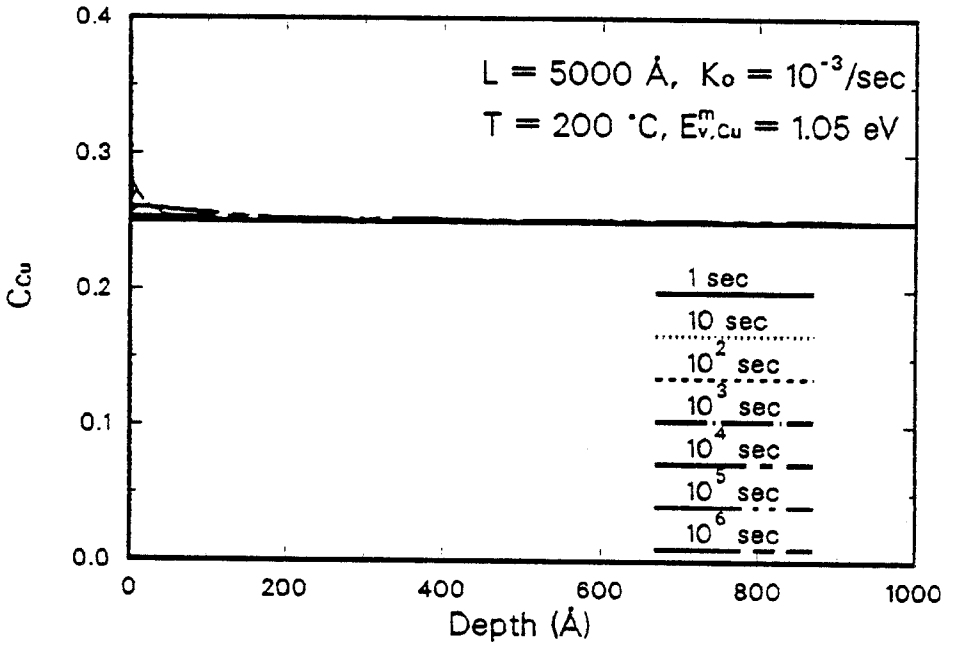

Figure 6.36: Profile evolution for a uniform irradiation with $E^m_{v,Cu} = 1.05$ eV, at 200 °C

the previously discussed 14 MeV Cu irradiation on Ni target at 500 °C was calculated again to see the diffusion effect. Indeed, it can be seen that the diffusion broadened the Cu profile as expected. The Cu atoms can reach far beyond the ion range determined from collisional process up to 4 μm below the surface. Also, the peak concentration of Cu is found to be lowered accordingly. In Fig. 6.38, the TAMIX simulation result for a bilayer target is shown, which has already been discussed in a previous section for the collisional dynamic mode. The target is a Cu-Ni bilayer with 250 Åthickness of Cu, which is then irradiated with 50 keV Ar ions up to a fluence of 2×10^{16} /cm^2 at 200 °C and 500 °C. It can be observed that the intermixing between two layers are greatly enhanced by diffusion at higher temperature. In 500 °C profile, it can also be seen that at the target surface segregation occurs, which is not observed at

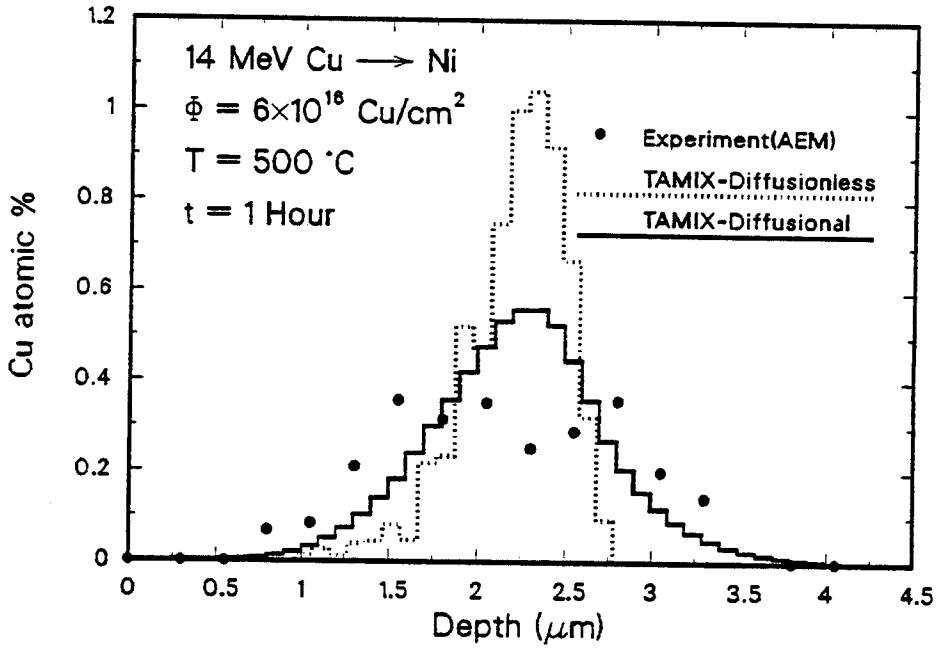

Figure 6.37: Ion distribution for 14 MeV Cu in Ni with diffusion 200 °C profile.

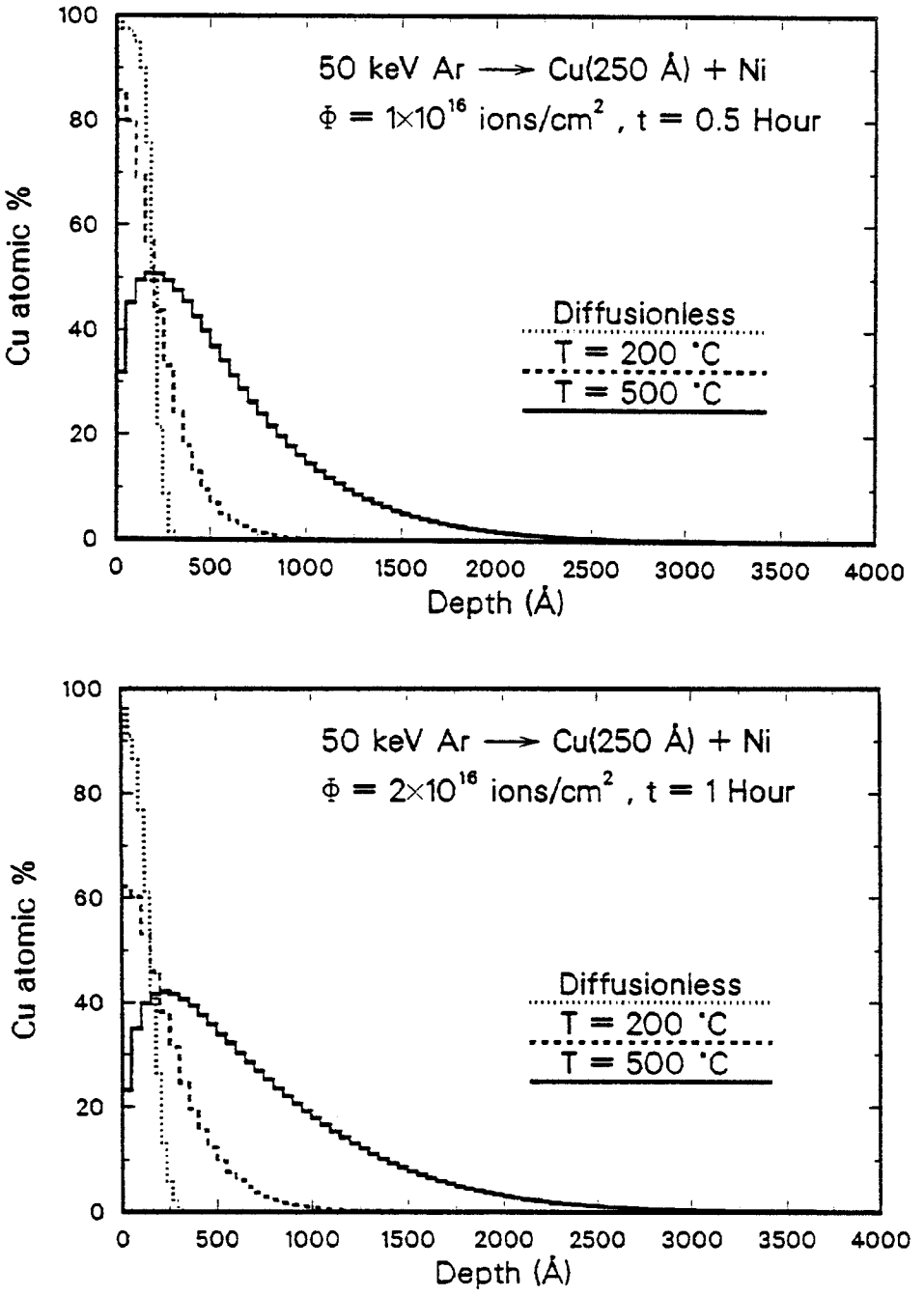

Figure 6.38: Ion beam mixing of Cu + Ni by 50 keV Ar irradiation with diffusion

References

[1] L. M. Wang, Ph. D. Thesis, Univ. of Wisconsin-Madison (1988).

[2] G. L. Kulcinski, J. L. Brimhall, and H. E. Kissinger, Production of Voids in Pure Metals by High-Energy Heavy-Ion Bombardment, in "Radiation-Induced Voids in Metals"(eds. J. W. Corbett and L. C. Ianniello), AEC Symposium Series, No 26(CONF-710601), p. 449 (1972).

[3] D. J. O'Connor, Nucl. Instr. and Meth. **196**, 493 (1982).

[4] M. Behar et al., Nucl. Instr. and Meth. **B6**, 454 (1985).

[5] M. Behar et al., Rad. Effect **90**, 103 (1985).

[6] J. L. Combasson et al., Rad. Effect **36**, 149 (1978).

[7] H. Nakata, Can. J. Phys. **46**, 2765 (1968).

[8] J. R. Conrad and C. Forest, in "IEEE International Conference of Plasma Science", Saskatoon, Canada, May 19-21, 1986 (IEEE, New York, 1986), p. 28.

[9] J. R. Conrad and T. Castagna, Bull. Am. Phys. Soc. **31**, 1479 (1986).

[10] J. R. Conrad et al., in "IEEE International Conference of Plasma Science", Arlington, Virginia, June 1-3, 1987 (IEEE, New York, 1987), p. 124.

[11] J. R. Conrad et al., J. Appl. Phys., **62**(11), 4591 (1987).

[12] W. Eckstein and H. Verbeek, "Data on light ion reflection", Max-Planck Inst. Plasma Phys. Rep. IPP 9/32 (1979).

[13] E. W. Thomas, J. Appl. Phys. **51**, 1176 (1980).

[14] H. H. Andersen et al., J. Appl. Phys. **47**, 13 (1976).

[15] D. Hildebrandt and R. Manns, Phys. Status Solidi A **38**, k155 (1976).

[16] J. Schou, H. Sørensen, and U. Littmark, J. Nucl. Mater. **76/77**, 359 (1978).

[17] D. Rosenberg and G. K. Wehner, J. Appl. Phys. **33**, 1482 (1962).

[18] H. Fetz and H. Oechsner, Ioniz. Phenom. Gases, Paris, Vol. **2**, p. 39 (1963).

[19] J. Roth, J. Bohdansky, and W. Ottenberger, "Data on Low Energy Light Ion Sputtering", IPP Report 9/26 (1979).

[20] O. Almen and G. Bruce, Nucl. Instr. and Meth. **11**, 257 (1961).

[21] C. H. Weijsenfeld, A. Hoogendoorn, and M. Koedam, Physica **27**, 763 (1961).

[22] H. L. Bay, J. Bohdansky, and E. Hechtl, Rad. Effect **41**, 77 (1979).

[23] O. C. Yonts, C. E. Normand, and D. E. Harrison, J. Appl. Phys. **31**, 447 (1960).

[24] N. Laegreid and G. K. Wehner, J. Appl. Phys. **32**, 365 (1961).

[25] H. Schirrwitz, Beitr. Plasmaphys. **2**, 188 (1962).

[26] B. M. Gurmin,T. P. Martynenko, and Ya. A. Ryzkov, Sov. Phys.-Solid State **10**, 324 (1968).

[27] V. K. Koshkin, "Sergev Ordzhonikidze" Aeronauti Institut, Report (1975).

[28] O. C. Yonts, in "Proc. Nuclear Fusion Reactor Conference(British Nuclear Energy Society, Culham 1969) p. 424.

[29] C. R. Finfgeld, ORO-3557-15 (1970).

[30] H. Oechsner, Appl. Phys. **8**, 185 (1975).

[31] G. Sletten and P. Knudsen, Nucl. Instr. and Meth. **102**, 459 (1972).

[32] Z. E. Switkowski et al., Rad. Effect **29**, 65 (1976).

[33] H. L. Bay, J. Roth, and J. Bohdansky, J. Appl. Phys. **48**, 4722 (1977).

[34] B. Emmoth, T. Fried, and M. Braun, J. Nucl. Mater. **76/77**, 129 (1978).

[35] M. Kaminsky et al., in "Int. Symp. Fusion Technology(Euroatom, Padua 1978) p. 112.

[36] T. Nenadovic and Z. Jurela, Ioniz. Phenom. Gases, Bucharest, p. 90 (1969).

[37] A. K. Furr and C. R. Finfgeld, J. Appl. Phys. **41**, 1739 (1970).

[38] H. H. Andersen and H. L. Bay, J. Appl. Phys. **45**, 953 (1974).

[39] E. P. EerNisse, Appl. Phys. Lett. **29**, 14 (1976).

[40] M. Szymonski et al., J. Phys. D. **11**, 751 (1978).

[41] P. Sigmund, Phys. Rev. **184**, 383 (1969).

[42] G. K. Wehner and D. Rosenberg, J. Appl. Phys. **31**, 177 (1960).

[43] W. O. Hofer, "Sputtering by Particle Bombardment III"(R. Behrisch, ed.) (1983).

[44] B. Perović.6 and B. Cobić, "Proc. 5th Int. Conf. on Ion Phenomena in Gases"(M. Maecker ed.) p. 1165 (1961).

[45] A. Gras-Marti and P. Sigmund, Nucl. Instr. and Meth. **180**, 211 (1981).

[46] B. M. Paine and M. A. Nicolet, Nucl. Instr. and Meth. **209/210**, 173 (1983).

[47] J. R. Conrad, private communication.

[48] W. Schüle and R. Scholz, Properties of Point Defects in FCC Metals in "Point Defects and Defect Interactions in Metals"(eds. J. Takamura, M. Doyama, and M. Kiritani), p. 257 (1982).

[49] R. W. Siegel, Atomic Defects and Diffusion in Metals in "Point Defects and Defect Interactions in Metals"(eds. J. Takamura, M. Doyama, and M. Kiritani), p. 533 (1982).

[50] H. Wiedersich, P. R. Okamoto, and N. Q. Lam, J. Nucl. Mater. **83**, 98 (1979).

Chapter 7.

Summary and conclusion

An extensive Monte Carlo computer program-TAMIX has been developed to simulate the complicated nature of ion beam mixing processes. In TAMIX, various levels of sophistication have been adopted to achieve the necessary accuracy for a desired computation speed, which include the tabulation of the scattering angle, energy-dependent mean free path for nuclear collision, 'random surface' model for sputtering, and concentration-dependent surface binding energies. Also, TAMIX is a highly optimized program, in which the variance reduction scheme and vectorization are utilized. The variance reduction was achieved by the use of importance sampling(splitting and Russian roulette). For vectorization, TAMIX uses a completely different algorithm from the conventional 'history-based' Monte Carlo method, i.e. 'event-based' algorithm is adopted in TAMIX to follow a bundle of particles at a time. Furthermore, some of the diffusional processes have been incorporated in TAMIX to take into account the temperature-dependent behavior of the target during irradiation.

The TAMIX code can be run in three modes of simulation, i.e. static mode, collisional-dynamic mode, and collisional-diffusional-dynamic mode, each of which is appropriate to a specific kind of interest. In static mode, the target is assumed to remain in its initial state, with which the static ion range and damage distribution at the low fluence limit can be calculated. Besides, the

sputtering characteristics of the target can also be investigated with this mode. In collisional-dynamic mode, the dynamic response of the target due to the collisional processes induced by ion irradiation can be effectively simulated. The preferential sputtering, altered layer formation, and collisional mixing can be examined with this mode of simulation. In collisional-diffusional-dynamic mode, the temperature-dependent diffusional processes are taken into account in addition to the collisional features. The radiation-enhanced diffusion and radiation-induced segregation were considered in the form of numerical solution of the governing diffusion equation.

The TAMIX program has been applied in several specific situations and the simulation results were compared to the available data and shown to be in good agreement. Also, very complicated situations have been effectively simulated with TAMIX, some of which include the multiple ion species, multiple(variable) ion energies, and co-deposition during irradiation, which is really difficult to be treated analytically.

From this work following conclusions can be drawn.

1. A highly optimized dynamic Monte Carlo program, TAMIX has been developed to effectively simulate the ion beam mixing process, in which some of the diffusional processes were also taken into account in addition to the collisional features.

2. With regard to the speed of the code, TAMIX code was found to be more than 20 times faster than a similar Monte Carlo code TRIM.SP for a sputtering calculation(D on Au). The large speed gain was achieved

through a variance reduction scheme and vectorization.

3. TAMIX can be run in three modes, i.e. **Static mode, C-Dynamic mode**, and **CD-Dynamic mode**, each of which is appropriate to a specific kind of problem.

4. The **Static mode** simulation results showed that

   - The ion distribution for 14 MeV Cu in Ni calculated with TAMIX was much narrower than measured in an experiment, which was performed at 500 °C. The projected range of Cu agreed well with the experimental result. (See chapter 6. for further clarification.)
   - The calculated heavy ion ranges and stragglings in Si using the Universal interatomic potential showed a good agreement with experimental data. However, Au showed a sizable deviation either from the calculated result or the average behavior of the other elements.
   - The predicted range of MeV range N^{14} in Ni showed a reasonable agreement with a slight underestimation of about 6 %.
   - The light ion back-scattering coefficients have been calculated for the cases of D on Fe and He on Ag, which showed good agreement with experimental data.
   - The total sputtering yields of both heavy and light ions on Be, Ni, Mo, Au, and stainless steel have been compared with experimental data. For Be, a noticeable underestimation of the sputtering yield

has been observed especially for low energy Kr. For Ni and Mo, the agreements were quite good. For Au, the expected underestimation was found for both heavy and light ions. For a multicomponent target, stainless steel, a slight overestimation was observed.

- The angular dependence of the sputtering yield has been investigated for Xe on Ni and He on Ni. For Xe, the predicted behavior from analytical sputtering theory was found. For He, the negligible enhancement of sputtering yield for glancing incidence observed in the experiments, was confirmed by TAMIX simulation.
- The angular distribution of the sputtered atoms was also investigated for Xe on Ni and He on Ni. The calculation results showed the same behavior as in experiments, that is, for Xe the transition from undercosine to overcosine with increasing energy was clearly seen. Such an effect was not found in He ion sputtering.
- For glancing angle incidence, the experimentally observed enhancement in specular direction was also seen from TAMIX simulation.
- The energy distribution of sputtered atoms showed a maximum at the half of the surface binding energy and the $\frac{1}{E^2}$ behavior at the high energy tail.
- TAMIX simulation showed the greater contribution from low-indexed recoils to the sputtering yield for the light ion compared to that for the heavy ion sputtering. Also, it was shown that the major portion of sputtered atoms originates from one or two monolayers at

the surface.

5. The **C-Dynamic mode** simulation results showed that

   - For multicomponent targets, the preferential sputtering of the lighter and less tightly bound element caused the formation of the altered layer with a thickness comparable to the maximum ion range. Recoil implantation of the lighter element was also observed.
   - In steady state, it was found that the partial sputtering yield of each component had the same value as predicted from mass conservation. The minimum ion fluence to reach the steady state was found to be lowest for an intermediate ion energy of 5 keV among investigated energies.
   - The calculated broadening of a thin Pt marker in Si from 300 keV Xe ion irradiation was found to be lower than measured in the experiment, but higher than the analytic prediction. Also, the broadening showed a square root dependence on the ion fluence, which was experimentally observed.
   - The scanning AES(Auger Electron Spectroscopy) was simulated with TAMIX to observe the smoothening of the concentration profile by the working ions.
   - The simultaneous C deposition during PSII-CH_4 irradiation was simulated with TAMIX and compared with the SIMS experimental data, which showed a good agreement at a C deposition rate of 100 Å per 2×10^{17} /cm^2 of ion fluence. The higher and lower

C deposition rate failed to reproduce the observed concentration profiles.

6. A uniform irradiation on a Ni-25Cu foil was investigated to see the segregation behavior, which gave the following conclusions.

   - Cu depletion from the surface was found most significant at the intermediate temperature range from 200 °C to 600 °C for a defect production rate of 10^{-3} /sec.
   - At higher temperature over 600 °C, the segregation was found to be small due to the increased mobilities of the point defects.
   - At lower temperature below 200 °C, the segregation at the steady state was also reduced, even though the transient behavior was observed. The reason for this is attributed to the vacancy flux from the subsurface region to the bulk caused by the high recombination rate of the vacancy in the bulk. Because the vacancy concentration is high at low temperature, the atomic flux driven by the vacancy motion is also significant. However, the negative vacancy concentration gradient in the subsurface region disappeared eventually, which gave the final reduced segregation.
   - The lower defect production rate shifted the segregation curve to lower temperatures because of the reduced defect concentration.
   - The diffusion behavior(of Cu-Ni system) was found to be very sensitive to the input parameters, most of which are not well-known.

7. The **CD-Dynamic mode** simulation results showed

   - The experimentally observed broad 14 MeV Cu profile in Ni at 500 °C was accurately predicted from diffusion-incorporated TAMIX code.

   - The intermixing of the Cu-Ni bilayer target was found to be enhanced by diffusion at high temperature. Moreover, the deeply penetrating Cu tail was also observed. Radiation-induced segregation was found to occur near the surface region.

8. Due to the uncertainties of the diffusion mechanism and involved parameters, a rather simple diffusion model has been used in TAMIX with the assumption that the target remains in a single phase during irradiation. The refinement of the program, especially the diffusion part, can be achieved by taking into account other contributing effects such as defect-solute binding in radiation-induced segregation model, surface segregation, and radiation-induced phase transformation along with the evaluation of the related thermodynamic parameters, which comprise the future direction of continued researches.